

UNIVERSITÀ DEGLI STUDI DI NAPOLI  
“FEDERICO II”

FACOLTÀ DI INGEGNERIA  
DIPARTIMENTO DI INGEGNERIA CHIMICA



Dottorato di Ricerca in Ingegneria Chimica,  
dei Materiali e della Produzione  
– XIX ciclo –

**Tesi di Dottorato**

**ADVANCED MECHANICAL SPECTROSCOPY  
TO INVESTIGATE THE MICROSTRUCTURE  
OF COMPLEX FLUIDS**

**Comitato Scientifico**  
*Nino Grizzuti (relatore)*  
*Massimiliano Grosso*  
*Pier Luca Maffettone*

**Candidata**  
*Claudia Carotenuto*

ANNO ACCADEMICO 2005-2006

# CONTENTS

<b>INTRODUCTION</b>	<b>1</b>
<i>Chapter 1</i>	
<b>DYNAMIC MECHANICAL SPECTROSCOPY</b>	<b>3</b>
1.1 Linear dynamic mechanical spectroscopy	3
1.2 Nonlinear dynamic mechanical spectroscopy	5
REFERENCES	8
<i>Chapter 2</i>	
<b>THERMOREVERSIBLE GELATION OF AQUEOUS SOLUTIONS OF HYDROXYPROPYLCELLULOSE</b>	<b>10</b>
2.1 Introduction	10
2.2 Materials	13
2.3 Methods	14
2.4 Experimental results and discussion	14
2.4.1 Rheology of the isotropic solution	14
2.4.2 Rheology of the direct <i>sol-gel</i> transition	16
Heating rate effect	20
Effect of concentration	21
Effect of ionic strength of aqueous solutions	22
2.4.3 Rheology of the reverse <i>gel-sol</i> transition	23
Reversibility	23
Cooling rate effect	25
Effect of HPC concentration	27
2.4.4 The effect of HPC molecular weight	30
Isotropic phase	30
Thermoreversible gelation	32
<i>Sol-gel</i> transition	34
<i>Gel-sol</i> transition	36
REFERENCES	38
<i>Chapter 3</i>	
<b>FOURIER TRANSFORM RHEOLOGY OF DILUTE IMMISCIBLE POLYMER BLENDS</b>	<b>40</b>
3.1 Immiscible polymer blends	40
3.1.1 Single drop dynamic	41

3.1.2 Interfacial stress	43
3.1.3 Blend linear viscoelasticity – SAOS tests	43
3.1.4 Blend nonlinear viscoelasticity – LAOS tests	46
3.2 Materials	46
3.3 Experimental Realization	48
3.3.1 Set-up	48
3.3.2 Data acquisition system	50
3.3.3 Signals' calibration	51
3.4 Experimental results	53
3.4.1 SAOS measurements	53
3.4.2 LAOS measurements	56
3.5 Model/Experiments comparison	61
3.5.1 The model	61
3.5.2 The method	63
3.5.3 Blend morphology estimation	64
3.6 On the occurrence of even harmonics	70
REFERENCES	74
<b>CONCLUDING REMARKS</b>	<b>77</b>



## INTRODUCTION

“Complex fluids” include polymeric liquids and melts, suspensions, emulsions, gel, micellar solutions, foams and so on. Although so diversified, all these systems present constitutive elements organized into a precise microstructure, which determines the macroscopic properties of the material.

Dynamical Mechanical Spectroscopy (DMS) is one fundamental rheological technique used to characterize the viscoelastic properties of complex fluids and to investigate their microstructure. In particular, during DMS experiments, the material is subjected to a sinusoidal shear deformation and the corresponding stress response is measured.

There are two different types of DMS tests, depending on the amplitude of the applied deformation, namely SAOS (Small Amplitude Oscillatory Shear) and LAOS (Large Amplitude Oscillatory Shear). SAOS is a robust, largely adopted rheology technique in which the strain is small enough to produce a linear response of the material. The stress is proportional to the oscillatory deformation and is represented by a sinusoidal wave with the same frequency. LAOS is a much more recent technique in which the deformation is large enough to determine a nonlinear response. The stress is still periodic, but not sinusoidal and can be deconvoluted in terms of a fundamental harmonic and its odd multiples. Stress is often analyzed in the Fourier space leading to the so called Fourier Transform Rheology. Nonlinear measurements are, obviously, more complex than linear ones. However, they carry much richer information about the morphology of micro-structured systems. Both SAOS and LAOS tests are used in this work.

SAOS measurements are adopted to follow the morphology evolution of hydroxy-propylcellulose (HPC)/water systems. Some aqueous solutions of cellulose ethers, like HPC, have the peculiar characteristic to form gel upon heating at about human body temperature. This feature, along with the well-known HPC biocompatibility, makes the material attractive as an injectable drug delivery matrix. The morphological changes of the system during the gelation process are really complex and not yet completely

understood.

LAOS measurements are used to probe the morphology of a dilute immiscible polymer blend. The microstructure of a dilute emulsion usually consists of spherical droplets immersed in a continuous matrix. The size and the distribution of the globular domains strongly affect the final properties of the product. By means of linear rheological measurements only the average drop size of the dispersed phase can be generally obtained. In this work, a new experimental procedure, based on LAOS tests, is proposed in order to estimate the drop size distribution of a polydisperse polymer blend.

The aim of this work is not only to obtain a robust characterization of the two considered complex fluids, but also to explore the potentiality of both linear and nonlinear DMS. The present thesis is structured as follows.

Chapter 1 contains the fundamentals of dynamic mechanical spectroscopy in linear and nonlinear regime.

Chapter 2 deals with the thermoreversible gelation of hydroxypropyl-cellulose/water systems. The direct *sol-gel* and the reverse *gel-sol* transition are studied by performing different heating/cooling cycles with different thermal ramp rates. The effect of HPC concentration, its molecular weight and ionic strength of aqueous solutions on the entire process is also analyzed and discussed.

Chapter 3 deals with the Fourier Transform Rheology applied to the microstructure analysis of a polydisperse polymer blend. This chapter contains an ample experimental section, in which the instrumental apparatus and the data acquisition system are detailed described. A model to interpret the nonlinear experimental results is also proposed and adopted to estimate the blend drop size distribution.

Conclusions on both SAOS and LAOS sections are drawn in the final chapter.

# CHAPTER 1

## DYNAMIC MECHANICAL SPECTROSCOPY

Dynamical Mechanical Spectroscopy (DMS) is one fundamental rheological technique used to characterize the viscoelastic properties of complex fluids and to investigate their microstructure. During DMS experiments, the system is subjected to a sinusoidal shear deformation,  $\gamma(t)$ :

$$\gamma(t) = \gamma_0 \sin(\omega t) \quad (1.1)$$

where  $\gamma_0$  is the amplitude of the applied strain and  $\omega$  is the frequency of oscillation. The shear rate,  $\dot{\gamma}(t)$ , is:

$$\dot{\gamma}(t) = \gamma_0 \omega \cos(\omega t) \quad (1.2)$$

The material stress response is measured and, by means of some adequate theoretical models, it is correlated to the characteristics of the system under investigation.

There are two different families of DMS tests, depending on the amplitude,  $\gamma_0$ , of the applied deformation; they are named SAOS (Small Amplitude Oscillatory Shear) and LAOS (Large Amplitude Oscillatory Shear). In the former case,  $\gamma_0$  is small enough to produce a linear response of the material, in the latter case, the amplitude of  $\gamma_0$  becomes large and determines a nonlinear response of the systems. The fundamentals of both SAOS and LAOS technique will be discussed in the following paragraphs.

### 1.1 Linear dynamic mechanical spectroscopy

Linear properties of viscoelastic fluids have been studied extensively and the

mechanical behavior in this regime is well investigated and documented in textbooks (Macosko 1994, Larson 1988, Collyer and Clegg 1998). SAOS measurements have been adopted to characterize a very large number of complex fluids: from polymer melts (Laun 1978) to liquids crystalline (Acierno e Grizzuti 2003), from gels (Winter and Chambon 1986) to polymer blends (Tucker and Moldenaers 2002).

The typical shear stress response of a SAOS test is:

$$\sigma(t) = \sigma_0 \sin(\omega t + \varphi) \quad (1.3)$$

The stress oscillates with the same frequency  $\omega$  of the imposed deformation, but it is shifted by an angle  $\varphi \in [0, \pi/2]$ . The value of  $\varphi$  is equal to 0 for elastic solids, so the stress is in phase with the strain. The value of  $\varphi$  is equal to  $\pi/2$  for viscous liquids, in this case, the stress is in phase with the shear rate. In the linear regime, the phase angle  $\varphi$  depends upon strain frequency only, and not on  $\gamma_0$ . Equation 1.3 is usually written in the following way:

$$\sigma(t) = \gamma_0 (G' \sin(\omega t) + G'' \cos(\omega t)) \quad (1.4)$$

where:

$$G' = \frac{\sigma_0}{\gamma_0} \cos(\varphi) \quad (1.5)$$

$$G'' = \frac{\sigma_0}{\gamma_0} \sin(\varphi) \quad (1.6)$$

The term  $G'$  is in phase with the strain and is called elastic or storage modulus, while the term  $G''$  is in phase with the shear rate and is called viscous or loss modulus.

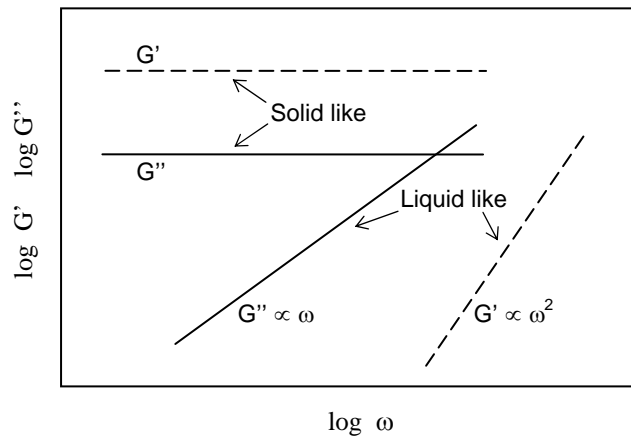


Figure 1.1. Illustrations of frequency-dependent storage and loss  $G'$  and  $G''$  modulus for typical “liquid-like” and “solid-like” materials.

As already said, in linear regime the amplitude of the stress is proportional to the amplitude of the imposed deformation, consequently  $G'$  and  $G''$  do not depend on  $\gamma_0$ , but on frequency only. The storage and loss modulus for typical “liquid-like” and “solid-like” fluids are shown in figure 1.1. For the “liquid-like” fluid, the elastic modulus is much lower than the viscous one and it scales with frequency as  $G' \propto \omega^2$ , the viscous modulus is linear in frequency,  $G'' \propto \omega$ . For “solid-like” fluid,  $G' \gg G''$ , and  $G'$  is nearly frequency-independent. Real complex fluids often show an intermediate *viscoelastic* behavior, as can be observed in figure 1.2. At low frequencies, the system is “liquid-like”, with  $G' \ll G''$ , while more nearly “solid-like” behavior, with  $G' > G''$ , is found at high frequencies.

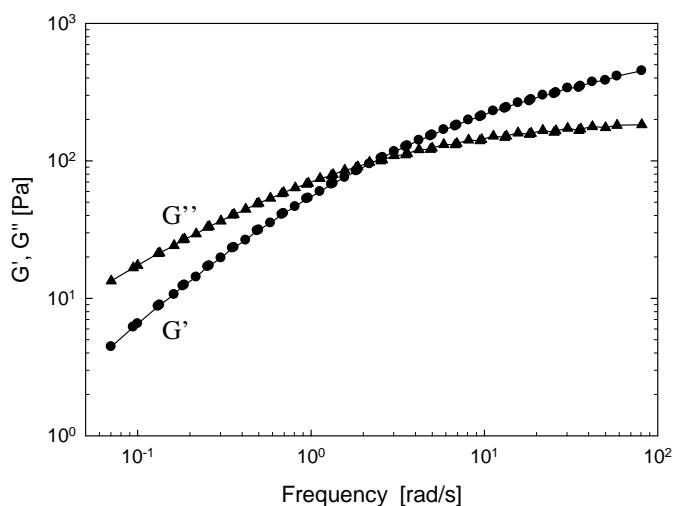


Figure 1.2. Storage (●) and loss (▲) modulus as a function of frequency for an aqueous solution of hydroxypropylcellulose, at 25°C.

### 1.2 Nonlinear dynamic mechanical spectroscopy

Nonlinear dynamic mechanical spectroscopy is intrinsically more complex than linear one, from both the experimental and the theoretical point of view. The interest for this kind of measures is twofold. First of all, many polymeric systems are processed in the nonlinear regime, thus LAOS experiments can give useful information on the material properties just in that range. Furthermore, nonlinear tests are able to provide a very detailed characterization of complex fluids microstructure, as it will be explained

below. In the seventies, the first experimental works on nonlinear measurements start to appear (Krieger and Niu 1973, Tee and Dealy 1975), but only in the last two decades, they are significantly increased (Giacomin and Dealy 1996, Wilhelm et al. 1998 - 1999 - 2002, Debbaut and Burhin 2002, Neidhöfer et al. 2003), thanks to the great improvement of the instrumental and software devices.

The shear stress response of a LAOS test is still periodic, with the same frequency  $\omega$  of the imposed oscillation, but not sinusoidal. It can be described by a Fourier series of odd harmonics:

$$\sigma(t) = \sum_{\substack{k=1 \\ k, \text{odd}}}^{\infty} a_k \cos(k \omega t) + \sum_{\substack{k=1 \\ k, \text{odd}}}^{\infty} b_k \sin(k \omega t) \quad (1.7)$$

where  $a_k$  and  $b_k$  represent the amplitude of the cosine and sine terms of the  $k$ -th harmonic and depend on both frequency and strain amplitude. They can be calculated as follow:

$$a_k = \frac{2}{T} \int_0^T \sigma(t) \cos(k \omega t) dt \quad (1.8.a)$$

$$b_k = \frac{2}{T} \int_0^T \sigma(t) \sin(k \omega t) dt \quad (1.8.b)$$

where  $T$  is the period of the imposed strain oscillation. By using the Euler notation,  $e^{\pm jx} = \cos x \pm j \sin x$ , the equation 1.7 becomes:

$$\sigma(t) = \sum_{\substack{k=-\infty \\ k, \text{odd}}}^{\infty} I_{k\omega} e^{jk\omega t} \quad (1.9)$$

$$I_{k\omega} = \frac{2}{T} \int_0^T \sigma(t) e^{-jk\omega t} dt \quad (1.10)$$

In equation 1.9,  $I_{k\omega}$  is the complex coefficient of the  $k$ -th harmonic in the Fourier domain,  $I_{k\omega} = a_k - jb_k$ . It should be remarked that shear stress is an odd function of the strain. As a consequence, only odd terms of the Fourier series are accounted for in equations 1.7 and 1.9.

In figure 1.3 the typical shear stress response of a LAOS measurement is reported both in time and in Fourier domain (Wilhelm et al. 1999). The occurrence of odd multiples of fundamental harmonic is apparent. The number and the amplitude of the

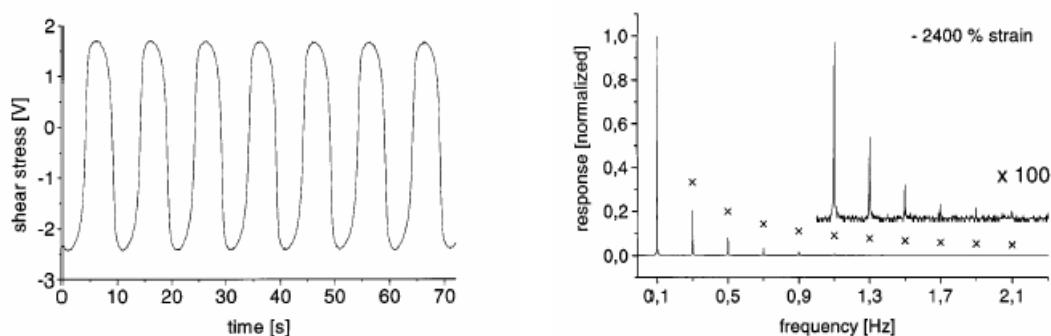


Figura 1.3. Shear stress response both in time and in frequency domain of a polyisobutylene sample subjected to a sinusoidal deformation at 0.1 Hz, with a strain amplitude equal to 2400% (Wilhelm et al. 1999)

detected overtones are proportional to the nonlinearity of the systems. It must be remarked that during a LAOS test, the system is deformed with a single frequency, while the stress presents more than one frequency, so the experimental response is spread on different time scales and, consequently, contains much richer and more detailed information on the investigated material.

LAOS technique requires 1) a sophisticated experimental apparatus, 2) an elaborated data manipulation, 3) a theoretical model able to interpret nonlinear results. The first two points are largely discussed in the literature (Giacomin and Dealy 1993, Wilhelm 2002), while only few references exist on the third point (Neidhöfer et al. 2003, Guido et al. 2004). Wilhelm indicates the fundamental modifications of traditional rotational rheometer to correctly implement the nonlinear dynamic mechanical spectroscopy. The author underlines the importance to improve as much as possible the signal to noise ratio of the acquired experimental signals. He also suggests some practical contrivances to obtain this highly sensitive detection. Since experimental data are analyzed in the Fourier domain, the technique is usually named *Fourier Transform Rheology* (FTR).

The data analysis in the Fourier rather than in the time domain allows a series of advantages. First of all, the occurrence of nonlinearity is better observed (Reimers and Dealy 1996). FTR can detect the nonlinear contribution at about 10-times lower strain amplitude compared to linear oscillatory measurements (Wilhelm et al. 2000). The stored files of the experimental points contain only the intensity of the odd peaks, so

they occupy a small amount of memory. Furthermore, the Fourier coefficients are robust to experimental noise. It must be noted that only the third and fifth overtones and, in particular, their absolute value are usually adopted. Only few works separate the real and imaginary part of the harmonics (Reimers and Dealy 1996, Neidhöfer et al. 2003).

LAOS tests are applied to the characterization of few systems like polystyrene melts (Neidhöfer et al. 2004), block copolymers (Langela et al. 2002) and colloidal dispersions (Kallus et al. 2001). All these studies are essentially qualitative and they do not contain theoretical models able to correlate experimental points to the morphology of the systems. Nowadays, this is the fundamental lack of the Fourier Transform Rheology. The present work tries to fill this gap.

## REFERENCES

- Acierno S, Grizzuti N (2003) "Measurements of the rheological behaviour of a crystallizing polymer by an "inverse quenching" technique." *J Rheol* **47**:563-576
- Collyer AA, Clegg DW (1998) "Rheological measurements". London, Chapman and Hall
- Debbaut B, Burhin H (2002) "Large amplitude oscillatory shear and Fourier transform rheology for a high-density polyethylene: experiments and numerical simulation." *J Rheol* **46**:1155-1176
- Giacomin AJ, Dealy JM (1993) "Large amplitude oscillatory shear" in "Techniques in rheological measurements". London, Chapman and Hall
- Guido S, Grosso M, Maffettone PL (2004) "Newtonian drop in a newtonian matrix subjected to large amplitude oscillatory shear flows." *Rheol Acta* **43**:575-583
- Kallus S, Willenbacher N, Kirsch S, Distler D, Neidhöfer T, Wilhelm M, Spiess HW (2001) "Characterization of polymer dispersions by Fourier transform rheology." *Rheol Acta* **40**:552-559
- Krieger IM, Niu TF (1973) "A rheometer for oscillatory studies of nonlinear fluids." *Rheol Acta* **12**:567-571
- Langela M, Wiesner U, Spiess HW, Wilhelm M (2002) "Microphase reorientation in block copolymer melts as detected via rheology and 2D SAXS." *Macromolecules* **35**:3198-3204
- Larson RG (1988) "Constitutive equations for polymer melts and solutions". Washington, Butterworth
- Laun HM (1978) "Description of the non-linear shear behaviour of a low density polyethylene melt by means of an experimentally determined strain dependent memory function." *Rheol Acta* **17**(1):1-15
- Macosko CW (1994) "Rheology: principles, measurements and applications". New York, VCH
- Neidhöfer T, Sioula S, Hadjichristidis N, Wilhelm M (2004) "Distinguishing linear from star-branched polystyrene solutions with Fourier-Transform rheology." *Macromol Rapid Commun* **25**:1921-1926
- Neidhöfer T, Wilhelm M, Debbaut B (2003) "Fourier-transform rheology experiments and finite-element simulations on linear polystyrene solutions." *J Rheol* **47**(6):1351-1371
- Reimers MJ, Dealy JM (1996) "Sliding plate rheometer studies of concentrated polystyrene solutions: Large amplitude oscillatory shear of a very high molecular weight polymer in diethylphthalate." *J Rheol* **40**(1):167-186
- Tee TT, Dealy JM (1975) "Nonlinear viscoelasticity of polymer melts." *Trans Soc Rheol* **19**:595-615

- Tucker CL, Moldenaers P (2002) "Microstructural evolution in polymer blends." *Annu Rev Fluid Mech* **34**:177-210
- Wilhelm M (2002) "Fourier-Transform Rheology." *Macromol Mater Eng* **287**(2):83-105
- Wilhelm M, Maring D, Spiess HW (1998) "Fourier-transform rheology." *Rheol Acta* **37**:399-405
- Wilhelm M, Reinheimer P, Ortseifer M (1999) "High sensitivity Fourier-transform rheology." *Rheol Acta* **38**:349-356
- Wilhelm M, Reinheimer P, Ortseifer M, Neidhöfer T, Spiess HW (2000) "The cross-over between the linear and nonlinear mechanical behaviour in polymer solutions as detected by Fourier-transform rheology." *Rheol Acta* **39**:241-246
- Winter HH, Chambon F (1986) "Analysis of linear viscoelasticity of a crosslinking polymer at the gel point." *J Rheol* **30**:367-382

# CHAPTER 2

## **THERMOREVERSIBLE GELATION OF AQUEOUS SOLUTIONS OF HYDROXYPROPYLCELLULOSE**

### **2.1 Introduction**

Water soluble cellulose derivatives are bio-compatible polymers widely applied in the food, pharmaceutical and cosmetic industries. In particular, when dissolved in water, they can be used as thickeners, binding agents, emulsifiers and stabilizers.

Aqueous solutions of cellulose ether polymers often present a complex phase behavior. Hydroxypropylcellulose (HPC), for example, undergoes various phase transitions upon changes of both temperature and concentration (Guido 1995, Lárez-V et al. 1995), as can be observed in figure 2.1. At room temperature, an increase of concentration determines an isotropic-liquid crystalline transition. The same transition occurs at high concentrations when the solution is cooled below a critical temperature (Guido and Grizzuti 1995).

A different microstructural evolution is observed when cellulose derivative solutions are heated from room temperature. Two main phase transitions, namely, polymer precipitation and gel formation may occur. This process is often called in the literature with the generic term “thermoreversible gelation” (e.g. Morawets 1975). The actual gelation is of particular interest in view of applications in the field of injectable drug delivery (Kabra and Bhagwati 1998). They are based on the possibility of inoculating the solution by exploiting its room temperature liquid-like behavior. Once

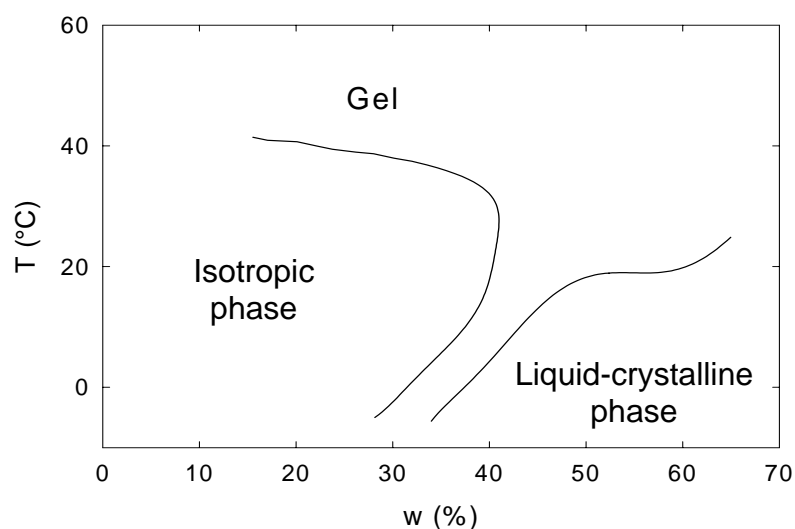


Figure 2.1. Phase diagram of an aqueous solution of HPC with a  $M_w = 80000$  Da. (Guido 1995)

inside the human body, the temperature increase determines the *sol-gel* transition. The positive effects are a better coating performance of the polymeric system as well as a drug delivery enhancement by the de-swelling effect due to polymer/water segregation.

*Sol-gel* transition usually happens by lowering the temperature. The peculiar behavior of aqueous solutions of HPC to form physical gel upon heating can be explained by observing the chemical structure of hydroxypropylcellulose (figure 2.2). It presents hydrophilic ends which allow the polymer dissolution in water and hydrophobic segments which are responsible of the gel formation (Ford 1999). At room temperature, water surrounds polymer chains screening physical bonds among propylic

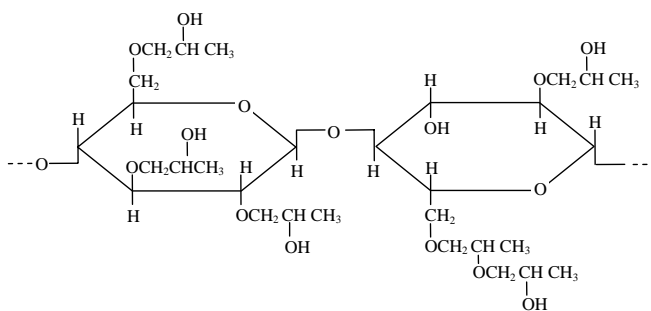


Figure 2.2. Possible hydroxypropylcellulose chemical structure (DS = 2.5, MS = 3)

segments of HPC. To underline this screening effect of the hydration water, Elias (1989) refer to an “ice-like structure”, Haque and Morris (1993) use the expression “water-cage” and Fujii et al. (2001) coin the term “water-shell”. At higher temperature, the quality of water/polymer relation decreases and propylic segments remain progressively “uncovered” and free interacting each other to form a three-dimensional network.

Rheological techniques have been often used to characterize the mechanical behavior of cellulosic ether solutions. An exhaustive review of the rheology of cellulosic solutions has been recently given by Clasen and Kulicke (2001). Thermoreversible gelation has been widely studied, especially with reference to Methylcellulose (MC) and Hydroxypropylmethylcellulose (HPMC) (Heymann 1935, Sarkar 1979, Haque and Morris 1993, Sarkar 1995, Hirrien et al. 1998, Desbrières et al. 2000, Hussain et al. 2002). There exists a certain degree of controversy regarding the mechanism of gelation. The major discussion concerns the nature of the zones involved in the gelation. Savage et al. (1963) suggest that the ability to gel is a consequence of the presence of zones containing the original cellulosic structure. This is not consistent with the observation of Heymann (1935) who studies highly substituted methylcellulose. Rees (1972) refers to micellar interactions and Sarkar (1979) postulates that gelation is due to hydrophobic or micellar interactions. Khomutov et al. (1993) propose that gelation is due to crystallization. The question can be considered still open. All these works deal with MC and HPMC aqueous solutions. In comparison, much less work has been devoted to the *sol-gel* transition of HPC/water systems (Haque et al. 1993, Fujii et al. 2001).

Gelation is often coupled with precipitation. In this case, the gel is opaque and not transparent (Hirrien et al. 1998, Hussain et al. 2002). The interrelationship between gelation and precipitation remains relatively poorly understood.

In this work, the thermoreversible gelation of commercial HPC aqueous solutions has been studied by means of linear dynamic mechanical spectroscopy. Some optical measurements (turbidimetry) are also conducted. Both the “direct” *sol-gel* and the “reverse” *gel-sol* transition are studied by performing different heating/cooling cycles

with different thermal ramp rates. Particular attention is dedicated to the role of precipitation on the entire process. The effect of HPC concentration, HPC molecular weight and ionic strength of aqueous solutions is also analyzed and discussed.

## 2.2 Materials

Hydroxypropylcellulose is a non ionic, water soluble polymer prepared by reacting alkali cellulose with propylene oxide at elevated temperature and pressure. The propylene oxide can be substituted on the cellulose macromolecule, through an ether linkage at the three reactive hydroxyl groups present on each anhydroglucose monomer unit, so the Degree of Substitution,  $DS$ , may vary from 0 to 3. The terminal hydroxyl group of the substituents is available for further reactions leading to side chains with more than one propylene oxide, so the Molar Substitution,  $MS$ , may be greater than 3. Both  $DS$  and  $MS$  influence the behavior of the macromolecule (Desbrières et al. 1998). A possible chemical structure of HPC is reported in figure 2.2.

Hydroxypropylcellulose used in this work is provided by Aqualon under its trade name Klucel EF. According to the manufacturer, the molecular weight,  $M_w$ , is 80000 Da,  $DS$  is  $\sim 2.5$  and  $MS \sim 3.7$ . Intrinsic viscosity measurements on the sample used in this work, as measured by Guido (1995), indicate a somewhat larger  $M_w \cong 132,000$  Da. The values of the Mark-Houwink constants used by Guido ( $K=2.6 \times 10^5$ ,  $\alpha=0.9$ ) are those determined by Wirick and Waldman (1970) for aqueous solutions of HPC at 25°C.

The samples are prepared by adding the desired amount of dry HPC powder to double-distilled water. Due to the long dissolution times, solutions are kept at rest for one month. They are periodically, gently hand-mixed by means of a glass rod to guarantee sample homogeneity. The adopted weight concentration,  $w$ , ranges from 10% to 40%.

At room temperature, the intrinsic viscosity of the adopted HPC is  $[\eta]=1.02$  dl/g (Guido 1995). This means that the overlapping concentration is of the order  $c^* \cong 10$  g/L, that is about 1% by weight. Therefore, at the concentrations investigated here, solutions are expected to be in the concentrated regime.

### 2.3 Methods

Rheological measurements are carried out on a controlled stress rheometer (Rheometrics DSR 200). A cone and plate geometry of 25 mm diameter and 0.1 rad angle is used. Temperature is controlled by a Peltier unit, which guarantees a thermal stability within  $\pm 0.1^\circ\text{C}$ . All measurements are performed under oscillatory shear mode in the linear viscoelastic regime. Linearity is verified under all experimental conditions. Depending on temperature, the maximum amplitude of the applied stress never exceeds the value of 15 Pa.

In view of the strong effect of HPC concentration on solution viscosity (see paragraph 2.4.1) it is essential to avoid solvent evaporation. For this reason, a low viscosity silicone oil (Dow Corning, 20 cSt), immiscible with water and HPC, is used to seal the sample.

Solution turbidity changes during phase transition are determined by transmitted light measurements. To this end, HPC samples are placed between the transparent parallel plates of a Linkam hotstage (CSS450, Linkam Scientific Instruments). Optical observations are made by a microscope (Axioskop 2 Plus, Carl Zeiss Inc) equipped with a 10 $\times$  magnification objective. Light is generated by the standard microscope lamp. Images are recorded by means of a CCD camera (TMC-76s, Pulnix Inc) connected to a PC-hosted image acquisition board (PCI-1409, National Instruments). The average gray level signal over the whole CCD field of view is taken as proportional to the intensity of the transmitted light.

### 2.4 Experimental results and discussion

#### 2.4.1 Rheology of the isotropic solution

As mentioned in paragraph 2.1, HPC solutions are isotropic at room temperature below a concentration of about 41%wt (Guido 1995). This is confirmed by the optical transparency of the samples both under polarized and non polarized light. Figure 2.3 shows the complex viscosity,  $\eta^*$ , as a function of frequency for the 30%wt solution at 25 $^\circ\text{C}$ . The typical response of a homogeneous polymer system can be observed.

Over the whole concentration range investigated, the Newtonian viscosity,  $\eta$ ,

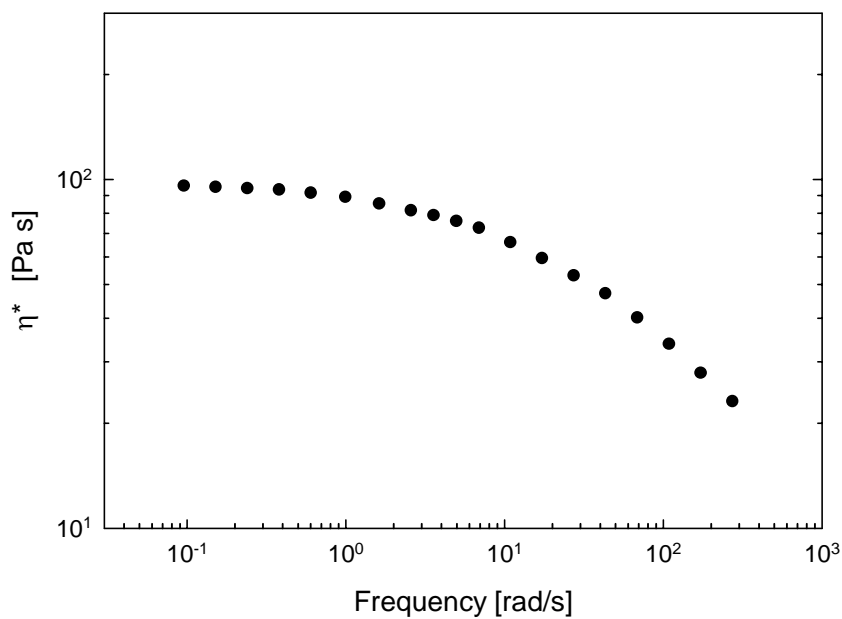


Figure 2.3. Complex viscosity as a function of frequency for a 30%wt HPC solution at 25°C.

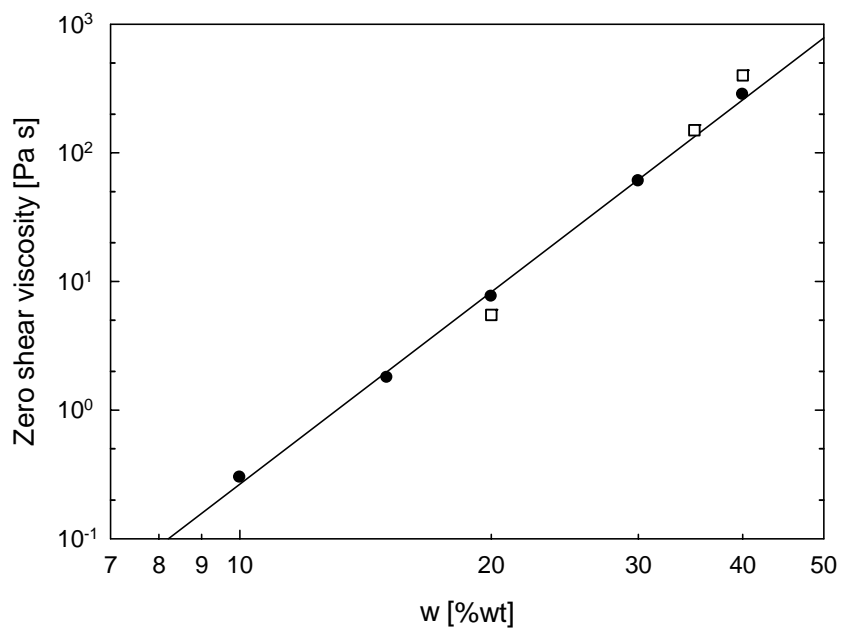


Figure 2.4. Zero-shear-rate viscosity as a function of HPC concentration at 25°C. Filled symbols: this work; empty symbols: data from Walker and Wagner.

shows a strong concentration dependence, as reported in figure 2.4. Data taken by Walker and Wagner (1994) on a similar HPC sample are also shown for comparison. Linear correlation of the experimental data on the log-log plot indicates a power-law functionality,  $\eta \propto w^n$ . The high exponent obtained ( $n=5$ ) is consistent with other literature data for HPC solutions. Phillis and Quinlan (1995) measure the Newtonian viscosity of HPC/water solutions over a wide range of concentrations and for molecular weights between 3 and 1.15 MDa. In particular they find that, for concentrations above 2-4 %wt, solutions are in the concentrated regime. In this region, the power law exponent ranges between 4.27 and 4.64, and increases with decreasing  $M_w$ . Extrapolation of these exponent data to the  $M_w$  used in the present work is in good agreement with the above determined value of  $n=5$ . An exponent of 4.24 is also reported by Clasen and Kulicke (2001) for HPC aqueous solutions. The data of figure 2.4 also confirm that the concentration dependence of these polymer solutions is higher than that predicted by theory for both flexible and rigid polymers (Doi and Edwards 1986, Pearson 1987).

#### **2.4.2 Rheology of the direct *sol-gel* transition**

When HPC solutions are heated from room temperature, a complex rheological response is observed. In this paragraph, details of such a behavior will be presented and related mechanisms of phase transition will be proposed.

In a typical experiment, the sample is heated from room temperature to 60°C by a thermal ramp with constant rates,  $dT/dt$ , ranging from 0.1 to 10°C/min. When heating, a small amplitude oscillatory flow is applied at a given frequency. When the stress amplitude remained within the linear viscoelastic limit, no influence of this parameter on the results reported below has been found.

Figure 2.5 shows the evolution of the viscoelastic moduli as a function of temperature for a 30%wt solution. The heating rate is 5°C/min. Initially, both moduli gradually decrease with increasing temperature, as expected for a homogeneous polymer solution. Notice that, in this region, the elastic modulus,  $G'$ , is lower than the viscous modulus,  $G''$ , at the assigned frequency. At an intermediate temperature (about

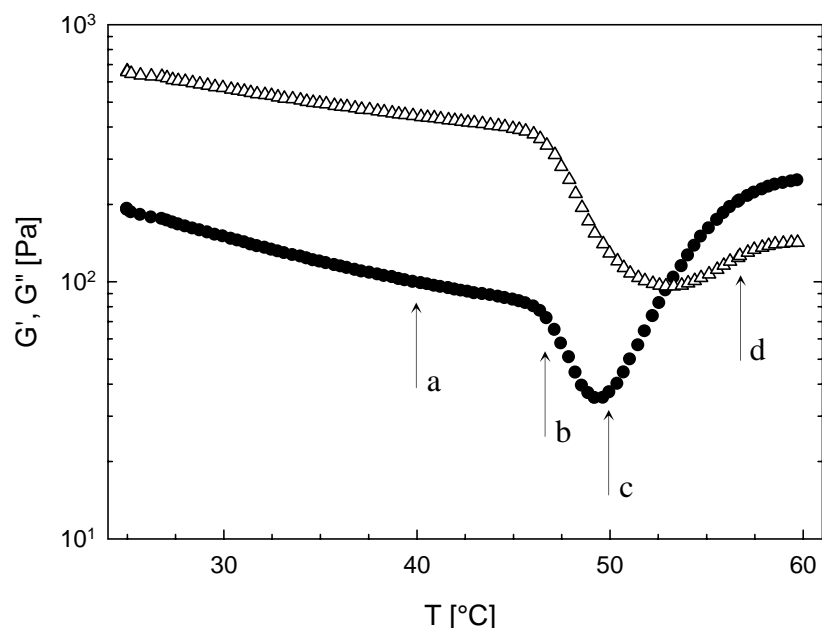


Figure 2.5. The elastic (●) and loss (△) moduli of a 30%wt HPC solution as a function of temperature during a heating ramp at 5°C/min. The oscillation frequency is 10 rad/s. Arrows refer to temperature where frequency sweep tests were performed (see figure 2.7).

46°C for the sample shown in figure 2.5), however, a sudden change in the slope of  $G'$  and  $G''$  is observed. The moduli fall much faster with temperature, eventually reaching an absolute minimum. At higher temperatures, both moduli start increasing and a crossover between them takes place. At the final temperature, both  $G'$  and  $G''$  essentially reach a plateau value.

The response shown in figure 2.5 is qualitatively similar for all samples investigated. A possible explanation of the just observed behavior is the following: a double step phase transition occurs in the system. In particular, the sudden drop of viscoelastic properties is determined by polymer precipitation. Conversely, the subsequent moduli raise, and the concurrent crossover leading to  $G' > G''$ , is determined by a *sol-gel* phase transition. The proposed picture, based solely on the rheological response, can be justified in view of the following experimental evidence.

One first evidence of polymer precipitation from the solution is given by direct eye observation. For example, when heated at the temperature of 48°C, that is, well inside the region of sharp moduli decrease, the solution shows a macroscopic phase separation, the fluid appearing stratified into an upper, more transparent phase, and a

lower milky suspension.

Polymer precipitation is further confirmed by turbidimetry measurements. Figure 2.6 is a plot of the relative adsorbed light intensity as a function of temperature. This parameter is defined as  $(I-I_0)/I_0$ , where  $I$  is the average luminosity of the microscope sample image, and  $I_0$  is the corresponding value at room temperature. The results of figure 2.6 are obtained under the same experimental conditions of the measurement reported in figure 2.5. The sudden change in light intensity takes place at the same temperature corresponding to the change in slope of the viscoelastic moduli, thus confirming that the precipitation process starts at 46°C. It can be also noticed that changes in turbidity essentially stop at the temperature corresponding to the minimum of the elastic modulus. It should be noticed that, after the sudden increase, a modest decrease in adsorbed light intensity is also observed for intermediate temperatures, followed by a local minimum at a temperature that roughly corresponds to the critical gel point (see below). At present, there is no definitive explanation for this behavior.

A first evidence for the second phase transition step at higher temperatures, i.e., a *sol-gel* transition, is already given by figure 2.5, where the cross-over between moduli

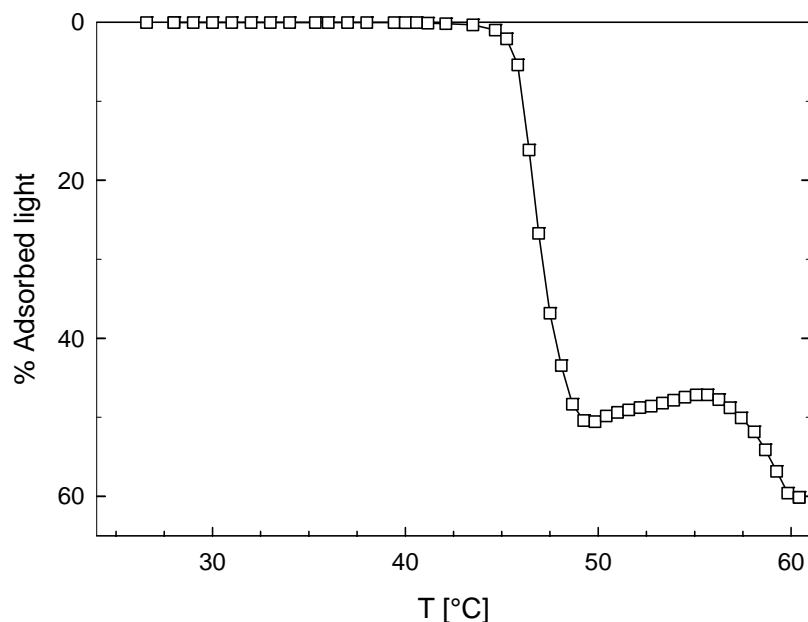


Figure 2.6. The relative adsorbed light intensity of a 30%wt HPC solution as a function of temperature during a heating ramp at 5°C/min.

suggests that a solid-like structure is developing. The results of figure 2.5, however, are obtained at a single frequency. Therefore, they cannot be a definitive proof of the gelation process. In order to clarify this point, frequency sweep tests were conducted at different temperatures during the heating stages. Figure 2.7 shows the viscoelastic moduli of the 30%wt HPC solutions at 40, 47, 50 and 57°C, respectively. Such temperatures are indicated by arrows in figure 2.5.

At 40°C (figure 2.7.a) the solution is isotropic and the moduli show the typical behavior of an entangled polymer liquid. In the explored frequency window  $G' < G''$  and the limiting slopes of 2 ( $G'$ ) and 1 ( $G''$ ) are reached at the lowest frequencies.

At 47°C (figure 2.7.b) precipitation has occurred to a large extent. Both moduli curves are shifted to lower values with respect to data at 40°C. The large drop, however,

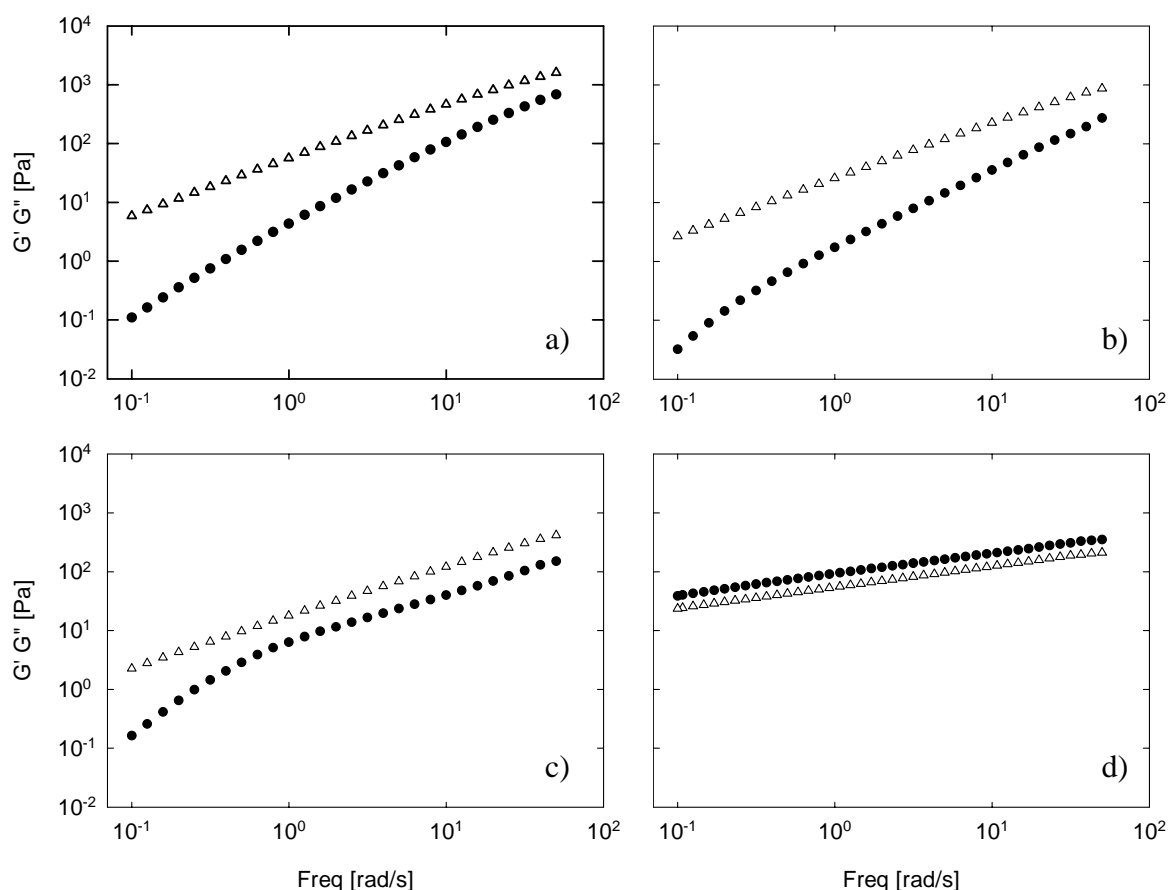


Figure 2.7. The elastic ( $\bullet$ ) and loss ( $\triangle$ ) moduli of a 30%wt HPC solution as a function of frequency at different temperatures. a) 40°C; b) 47°C; c) 50°C; d) 57°C.

cannot be justified only by the increase in temperature. In fact, precipitation decreases the concentration of the polymer in solution, thus making the latter more “dilute”. As a consequence, viscoelasticity is also strongly reduced.

At 50°C (figure 2.7.c) the elastic modulus starts increasing with increasing temperature. The formation of an interconnected molecular structure is confirmed, at this point, both by the increase of moduli and by the appearance of a new relaxation time in the  $G'$  curve.

Finally, at 57°C (figure 2.7.d) the gel is well formed, as confirmed by the fact that, over the whole frequency range,  $G' > G''$  and both moduli show a power-law behavior with the same exponent,  $G'$  and  $G'' \propto \omega^n$  (Winter and Mours 1997). In this case, figure 2.7.d gives  $n=0.35$ . To our knowledge, the critical gel exponent has never been directly determined for this family of cellulose ether solutions. Elaboration of the experimental results by Desbrières et al. (2000) on aqueous solutions of methylcellulose suggests a value of  $n=0.78$ .

### *Heating rate effect*

The experimental results reported above give strength to the hypothesis that precipitation and gelation take place sequentially. In particular, rheological measurements indicate that precipitation strongly affects the quality of the upcoming gel, as further demonstrated in figure 2.8 where the gel elastic modulus at 60°C,  $G'_{60^\circ}$ , is plotted as a function of the heating rate.  $G'_{60^\circ}$  strongly decreases as the heating rate decreases. Eventually, at a rate of 0.1°C/min there is no indication of gel formation. Based on these results we propose that the gel is formed only by “active” polymer chains, that is, those that are still present in solution after precipitation. For such chains the increasing hydrophobicity induces the formation of intermolecular temporary connections. Conversely, the fraction of HPC that precipitates does not take part to the gelation process. Low heating rates allow for a larger extent of polymer precipitation, thus subtracting HPC chains to the solution up to the point of inhibiting gel formation.

It should be mentioned that similar phase transition behaviors have been already reported for other cellulosic derivatives, like MC and HPMC (Desbrières et al. 1998,

Hussain et al. 2002). In particular, gelation is found to be the dominant mechanism for MC, whereas precipitation is more effective for HPMC, and increases with the amount of hydroxypropyl substituents (Haque et al. 1993). The results presented here for HPC solutions seem to confirm this trend, i.e. an increasing tendency to precipitation when moving from methyl- to fully hydroxypropyl-substituted polymers.

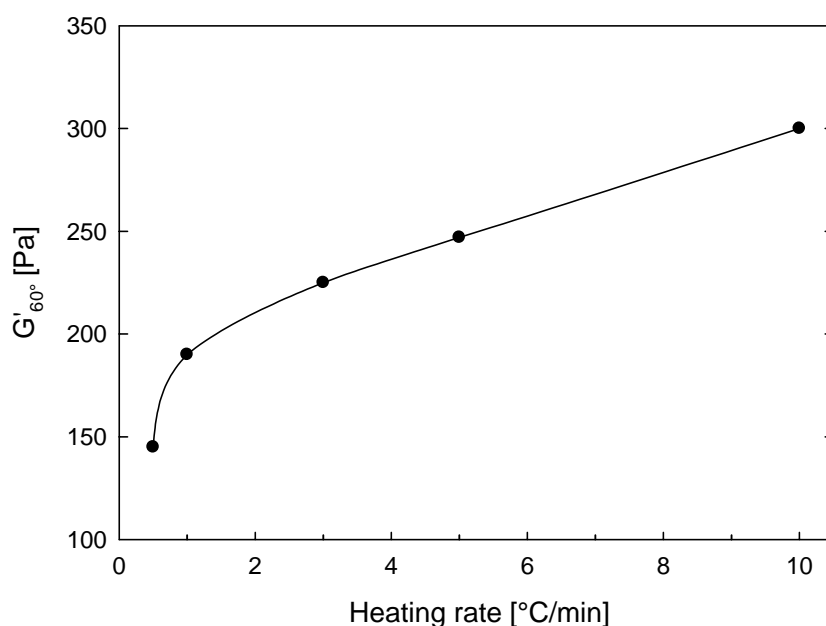


Figure 2.8. The elastic modulus of a 30%wt HPC solution, at 60^\circ C, as a function of the heating-rate. The oscillation frequency is 10 rad/s.

### *Effect of concentration*

The effect of concentration on the double phase transition is summarized in figure 2.9 where two characteristic temperatures of the process are plotted as a function of concentration.  $T_p$  is the temperature corresponding to the first change of slope of the viscoelastic moduli, thus representing the onset of precipitation.  $T_{co}$  is the temperature of cross-over between  $G'$  and  $G''$  and is therefore related to gel formation. Within experimental error, both temperatures do not depend on polymer concentration, indicating that phase transition is only driven by the thermally-induced changes in hydrophobic interactions. It should be noticed that no cross-over, and therefore no gel formation, is observed for concentrations below 20%wt.

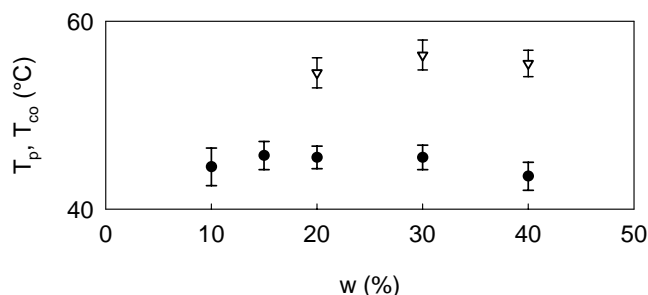


Figure 2.9. The precipitation (●) and cross-over (▽) temperatures as a function of the HPC weight fraction.

### *Effect of ionic strength of aqueous solutions*

Up to now, experimental evidence suggests that the morphology evolution of aqueous solutions of hydroxypropylcellulose can be ascribed to a change into water/polymer interactions with temperature. Consequently, a modification of ionic strength of aqueous solutions should cause a change of the two characteristic temperatures of the process:  $T_p$  and  $T_{co}$ .

The salinity is modified by adding potassium chloride,  $KCl$ , to the system. The adopted salt concentration ranges from 0.7 to 7% wt.

Figure 2.10 shows the behavior of  $T_p$  and  $T_{co}$  as a function of the amount of  $KCl$

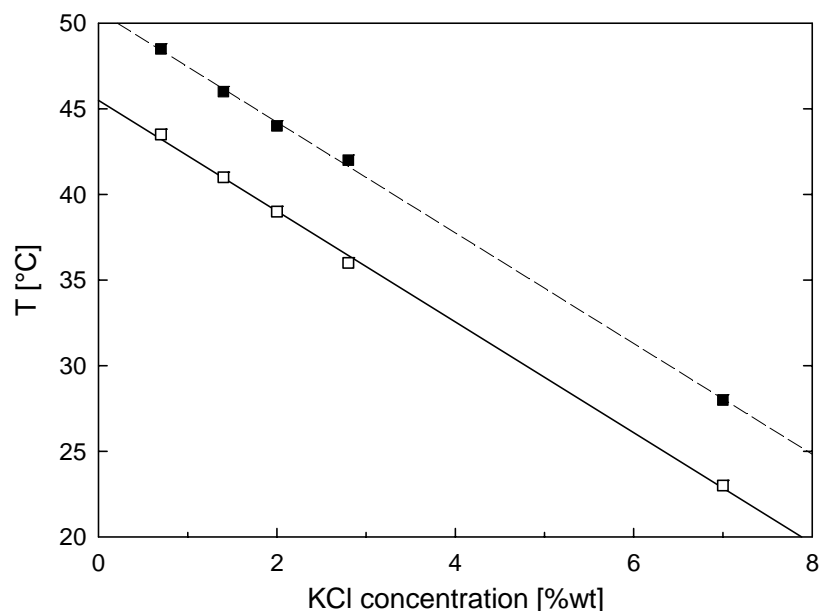


Figure 2.10. Precipitation temperature (□) and cross-over temperature (■) as a function of  $KCl$  weight concentration. The HPC concentration is 20% wt.

dissolved in solution. Both temperatures linearly decrease with salt concentration. The presence of potassium chloride worsens the solvent/HPC interactions, leading to an anticipated “water-cage” breakup. The zero shear viscosity of the isotropic solution is not influenced by the addition of *KCl*. The salt effect on the final properties of the gel is not investigated in this work. Sarkar (1979) added sodium chloride to methylcellulose aqueous solutions observing an increase of gel strength.

The dissolution of a salt into the system, apart from giving important information on the process mechanism, represents an easy and handy way to adjust the gelation temperature. Indeed, for the use of HPC solutions as injectable drug delivery systems,  $T_{co}$  must be equal to 37°C.

### 2.4.3 Rheology of the reverse *gel-sol* transition

The study of the *gel-sol* transition needs, first of all, the choice of a precise three-dimensional network to start from. Indeed, as said in the previous paragraph, the gel properties are strongly influenced by the adopted heating rate. This is why all the HPC/water solutions used to study the reverse *gel-sol* transition have been heated from 25 to 60°C at 5°C/min. This value combines a good thermal control with strong and stable three-dimensional networks. Furthermore, gel preparation is quite fast.

#### ***Reversibility***

The evolution of the viscoelastic moduli between 25 and 60°C, both upon heating and upon cooling, with thermal ramp rate  $dT/dt = \pm 5^\circ\text{C}/\text{min}$ , is shown in figure 2.11. After the completion of the whole heating/cooling cycle,  $G'$  and  $G''$  recover their initial room temperature value demonstrating that the phase transition is completely reversible. The complete reversibility is also confirmed by turbidity measurements.

From now on, to distinguish the symbols of viscoelastic moduli upon heating or cooling the subscript “+” or “-” will be used, where necessary.

During the cooling, the viscoelastic moduli follow a completely different evolution with respect to the heating cycle. In particular,  $G'_-$  is overlapped to  $G'_+$  up to 56°C. At this temperature the slope of the elastic modulus decreases and  $G'_-$  remains

almost constant until 50°C. This sort of “step” causes a difference between the  $G'_-$  and  $G'_+$  behaviour and leads to the formation of the *high temperature hysteresis loop*. In the just explored temperature interval,  $G''_-$  is superimposed to  $G''_+$  and no hysteresis is present in the viscous response of the system. At 50°C,  $G'_-$  starts to decrease again, crosses  $G'_+$  at 47°C and reaches a minimum at 46°C. By further reducing the temperature, the cooling elastic modulus increases and eventually, at 34°C, joins again the  $G'_+$  behavior. From 47 to 34°C a second, *low temperature hysteresis loop* can be observed not only for the storage modulus, but also for the loss one.

This rheological behaviour suggests a complex morphology evolution of the system upon cooling and puts in evidence great differences in the dynamics of formation and destruction of microstructure.

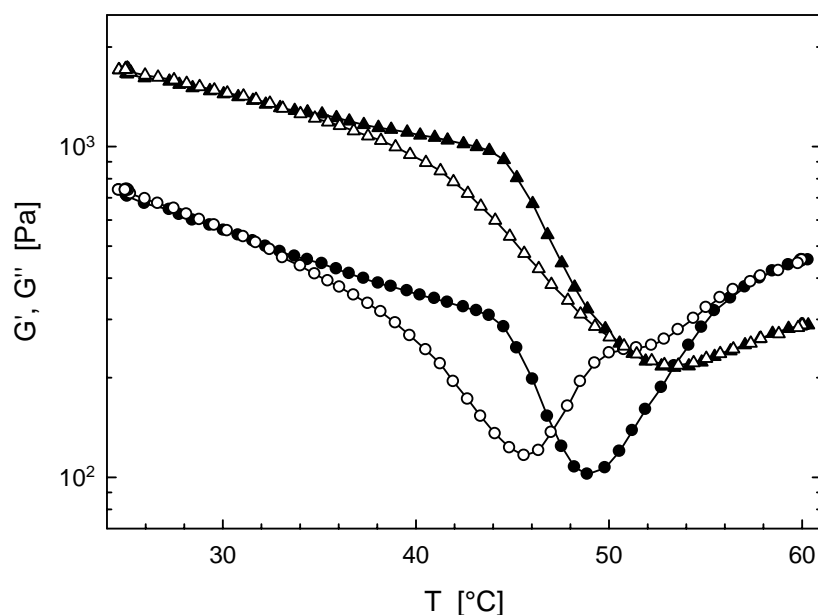


Figure 2.11. The elastic (*circular symbols*) and viscous (*triangular symbols*) modulus of a 37wt% HPC solution as a function of temperature during a heating/cooling cycle at  $\pm 5^\circ\text{C}/\text{min}$ . The frequency of oscillation is 10 rad/s. *Filled symbols* refer to heating, *empty symbols* to cooling.

### Cooling rate effect

As already observed, the heating rate has a crucial role in the “direct” process of gelation. For this reason, the effect of cooling rate on the “reverse” transformation has been immediately explored. In particular, all samples are heated at 5°C/min and cooled at rates ranging from -5 to -0.1°C/min.

The behavior of  $G'_-$  as a function of temperature at four different cooling rates is shown in figure 2.12.a. The  $G'_+$  is also reported for comparison. The cooling rate has no effect on the reversibility of the process. On the contrary, it presents a great influence on the two hysteresis loops. The high temperature hysteresis loop broadens by reducing the thermal rate. Conversely, the low temperature hysteresis loop size decreases by reducing thermal rate. The minimum of  $G'_-$  moves towards lower temperatures and its value increases as the cooling rate decreases.

The behavior of  $G''_-$  is shown in figure 2.12.b.  $G''_+$  is also reported for comparison. As regard the loss modulus, the high temperature hysteresis loop is absent for cooling rates of -5 and -2°C/min. It appears at -0.5°C/min and becomes broader at -0.1°C/min. No effect of cooling rate can be observed on the low temperature hysteresis loop of the loss modulus.

The enlargement of the high temperature hysteresis loop by reducing the cooling

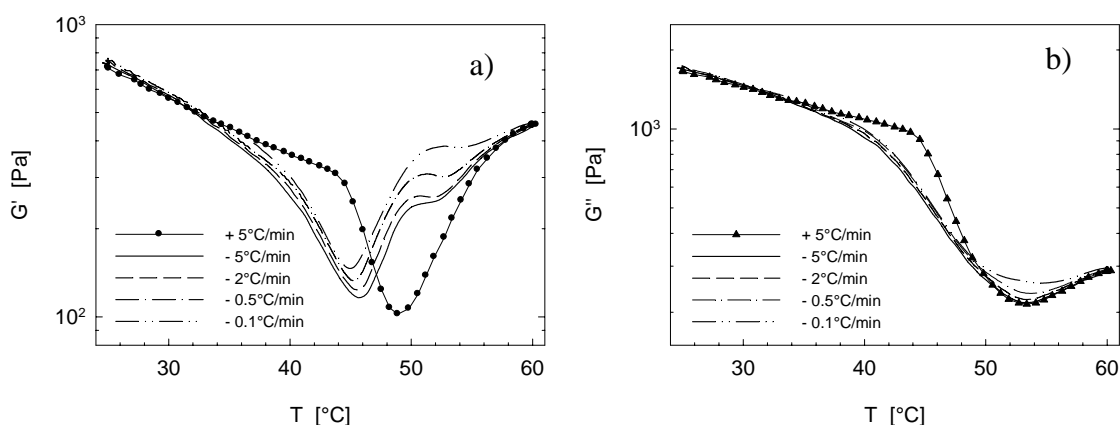


Figure 2.12. The a) elastic and b) viscous moduli of a 37%wt HPC solution as a function of temperature. The system is heated at 5°C/min and cooled at different thermal rates. The oscillation frequency is 10 rad/s.

rate, especially for the elastic modulus, is completely unexpected, being contrary to a “kinetic” intuition. Indeed, it is more natural to think that a fast cooling rate does not let time to gel destruction and, consequently, the elastic response of the system remains elevated. On the contrary, a slow cooling rate allows for a significant gel breakup, causing an evident reduction of  $G'_-$ . This incoherence could be justified throughout the follow hypothesis: the destruction of gel does not happen alone, but it is accompanied by the re-dissolution of precipitates. While the network breakup causes a reduction of storage modulus, the re-dissolution of HPC chains determines its increment. In this way, a slow cooling rate allows a re-dissolution of precipitates larger than a fast one, leading to a higher value of  $G'_-$ . This behavior gets along with the observed effect of cooling rate and saves the “kinetic” intuition.

The minimum value of  $G'_-$  (figure 2.12.a) confirms the just proposed hypothesis. Indeed, the elastic modulus minimum represents, both upon heating and upon cooling, a measure of precipitate amount present in solution before the beginning of gel formation or after the end of gel destruction, respectively. The minimum of  $G'_-$  is greater than the minimum of  $G'_+$  for all the performed cooling rates, suggesting that the amount of precipitates, at the minimum point, is less upon cooling than upon heating. So, in the *gel-sol* transition, the re-dissolution of chains is probably overlapped to gel breakup. Moreover, the amount of precipitates still present in solution, at the  $G'_-$  minimum, decreases by decreasing the cooling rate, suggesting again that the slower the thermal ramp, the larger the amount of re-dissolved chains.

All the performed thermal ramps are carried out at the fixed frequency of 10 rad/s. To obtain a more complete rheological picture of the microstructure evolution of the system, frequency sweep tests from 0.1 to 50 rad/s are conducted at different temperatures during the cooling stages. This procedure had already been used upon heating to study the *sol-gel* transition.

In general, the progressive break-up of a three-dimensional network leads to a decrease of the viscoelastic response of the system (Larson 1990). In particular, elastic modulus shifts downward and the  $G'$  low-frequency slope gradually increases

approaching the limiting liquid value of 2 (Venkataraman and Winter 1990). Figures 2.13.a and 2.13.b show, respectively, the frequency spectra of elastic and viscous modulus, measured at different temperatures, during the *gel-sol* transition of a 40% wt HPC aqueous solution, with a  $dT/dt = -0.1^\circ\text{C}/\text{min}$ . At low frequencies, the expected behavior of viscoelastic moduli is obtained, indeed  $G'$  and  $G''$  curves shift downward and their slopes increase. On the contrary, at high frequencies, both the elastic and loss moduli increase by decreasing the temperature. This behavior seems to suggest that the gel destruction, which leads to a reduction of viscoelastic moduli, is accompanied by another process that determines their increment. This second process could really be the re-dissolution of precipitates, thus confirming the supposed parallelism between gel breakup and re-solvation of HPC chains.

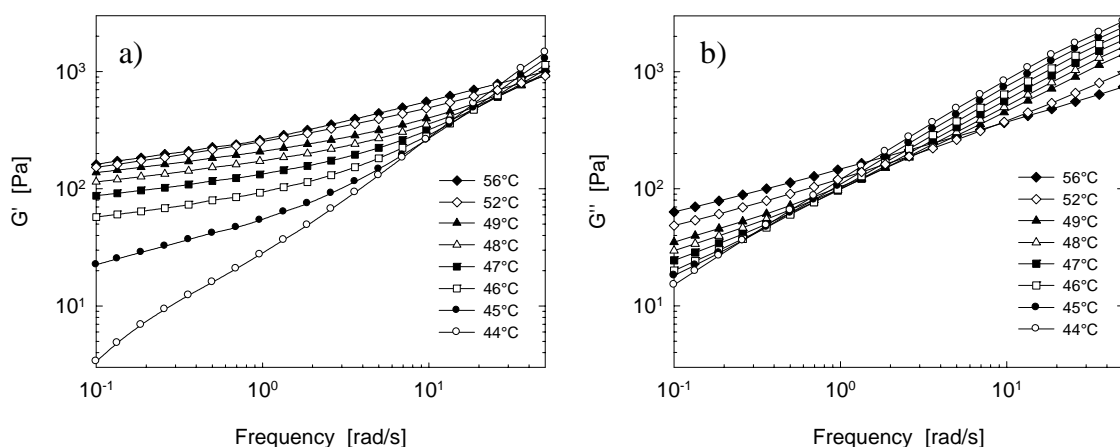


Figure 2.13. Frequency spectra of a 40% wt HPC solution, at different temperatures, during a cooling cycle at  $-0.1^\circ\text{C}/\text{min}$ .

### ***Effect of HPC concentration***

Figure 2.14 shows the evolution of the storage modulus during a heating/cooling cycle for three different HPC concentrations. The temperature is raised, as always, at  $5^\circ\text{C}/\text{min}$  and lowered at  $-0.1^\circ\text{C}/\text{min}$ . The upper cycle refers to a concentration of 40% wt, the middle to 30% wt and the lower to 20% wt. By reducing the amount of HPC, both the high and the low hysteresis loop decrease and eventually disappear at the lower concentration. To better understand this behavior the value of the elastic modulus

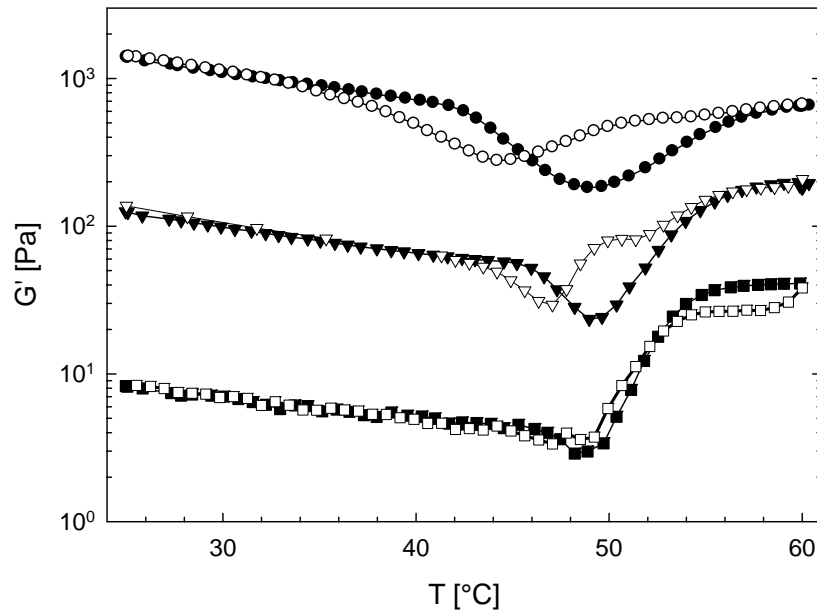


Figure 2.14. Elastic modulus as a function of temperature during a heating/cooling cycle for three different HPC concentrations: 40wt% (*circles*), 30wt% (*triangles*), 20wt% (*squares*). Heating rate is  $+5^{\circ}\text{C}/\text{min}$  (*filled symbols*), cooling rate is  $-0.1^{\circ}\text{C}/\text{min}$  (*empty symbols*).

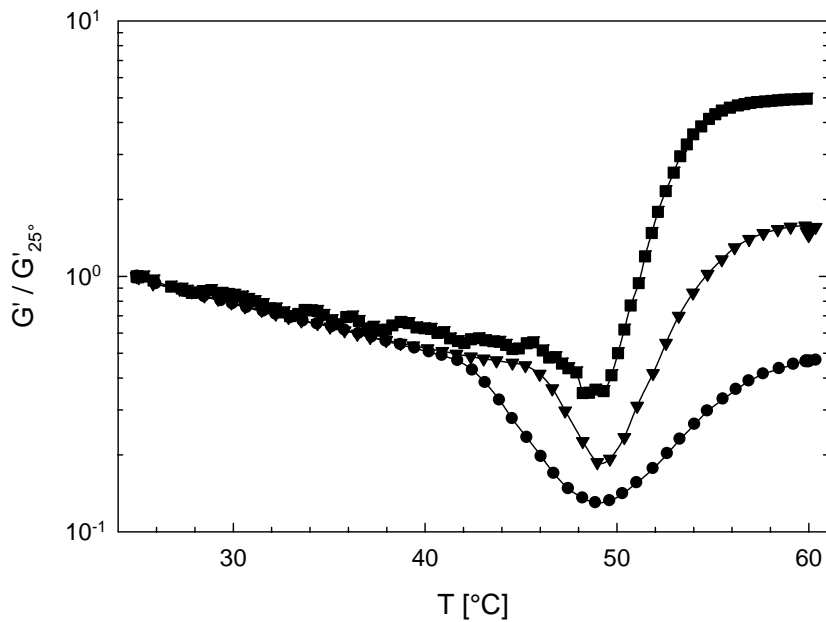


Figure 2.15. Normalized elastic modulus as a function of temperature for three different HPC concentrations: 40wt % (*circles*), 30wt % (*triangles*), 20wt % (*squares*)

divided by its own value at room temperature,  $G'/G'_{25^\circ}$ , during the heating stage, is reported in figure 2.15 for each studied concentration. This normalization allows an easier comparison among the systems. It is immediately evident that, by reducing the concentration, the minimum of  $G'/G'_{25^\circ}$  is higher. The precipitation process decreases and, consequently, subtracts less “active” chains from the solution, leading to the formation of proportionally stronger gels. For this reason, at 60°C, the characteristics of the three systems are different, being different the repartition of HPC chains between precipitation and gelation. So, where the precipitation is pronounced (40%wt) the hysteresis loops are large, where the precipitation is almost absent (20%wt) the hysteresis loops disappear.

The storage modulus of a 20%wt HPC solution versus frequency at different temperatures during a cooling stage is reported in figure 2.16. The experiment is the same reported in figure 2.13.a for a 40%wt HPC solution. The two graphs show a different behavior. The elastic modulus of the less concentrated system shows the typical behavior of gel destruction: it shifts downwards and its slope at low frequencies gradually increases. In this case, as mentioned before, the amount of precipitates is very

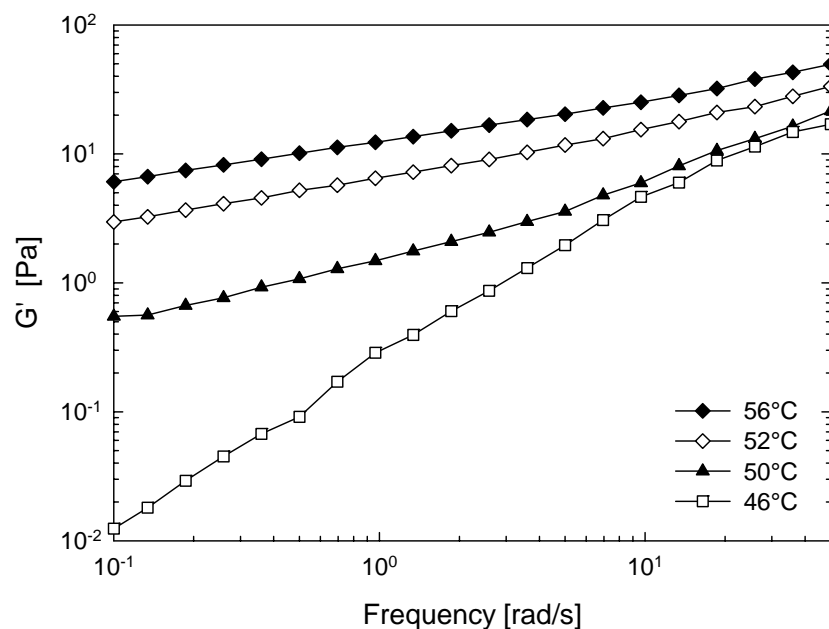


Figure 2.16. Elastic modulus of a 20wt % HPC solution as a function of frequency, at different temperatures. The corresponding cooling rate is -0.1 °C/min

small, and the anomalous increment of  $G'$  at high frequency, observed in figure 2.13.a, is absent.

The results exposed above underline the crucial role of precipitates in the process. Indeed, they are responsible of the formation of hysteresis loops and, consequently, of the unexpected trend of storage and loss moduli observed in figure 2.13.a and 2.13.b at high frequencies.

#### 2.4.4 The effect of HPC molecular weight

The effect of molecular weight is investigated by means of four different HPC samples, whose fundamental chemical characteristics are listed in table 2.1. It immediately emerges that the molar substitution of the EF-type (adopted until now) is larger than the MS of the remaining three samples. This difference is relatively small and it is considered acceptable. Anyway, this is the first characteristic that starts to distinguish the EF-sample from the other ones.

Table 2.1. Average Molecular weight ( $M_w$ ), Degree of Substitution ( $DS \in [0;3]$ ) and Molecular Substitution ( $MS \in [0;+\infty[$ ) of the four adopted HPC samples

<i>Klucel® mark</i>	$M_w [Da]$	$DS$	$MS$
EF	80000	2.5	3.7
GF	370000	2.5	3
MF	850000	2.5	3
HF	1150000	2.5	3

#### *Isotropic phase*

As already observed for the EF-type, the zero-shear viscosity,  $\eta$ , at room temperature, is strongly influenced by HPC concentration (figure 2.4). In particular, it is a power law function of concentration,  $\eta \propto w^n$ , with  $n = 5$ . Figure 2.17 reports the effect of concentration on zero-shear viscosity for the other molecular weights. The EF-

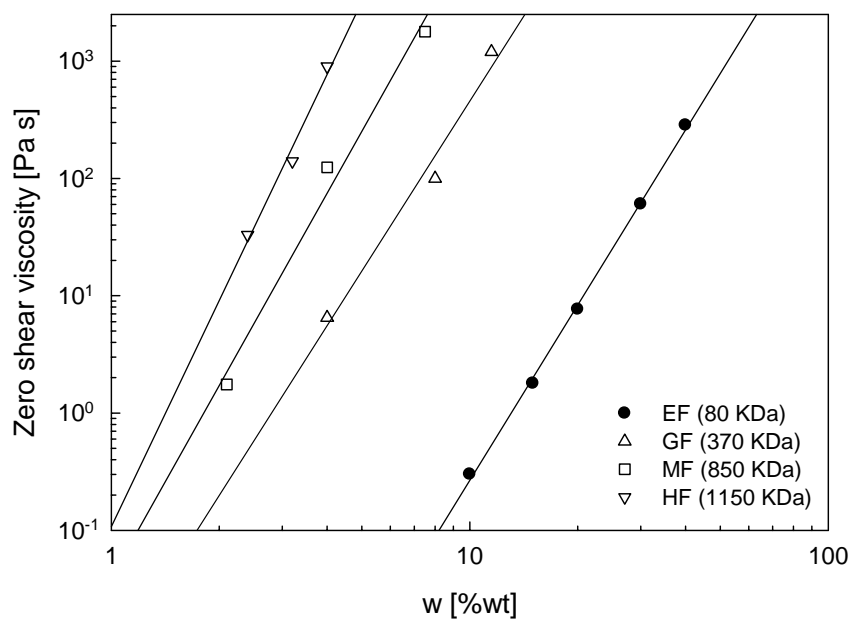


Figure 2.17. Zero-shear viscosity of HPC aqueous solutions as a function of polymer concentration for different molecular weights.  $T = 25^{\circ}\text{C}$ . The lines represent the linear regression for each data set.

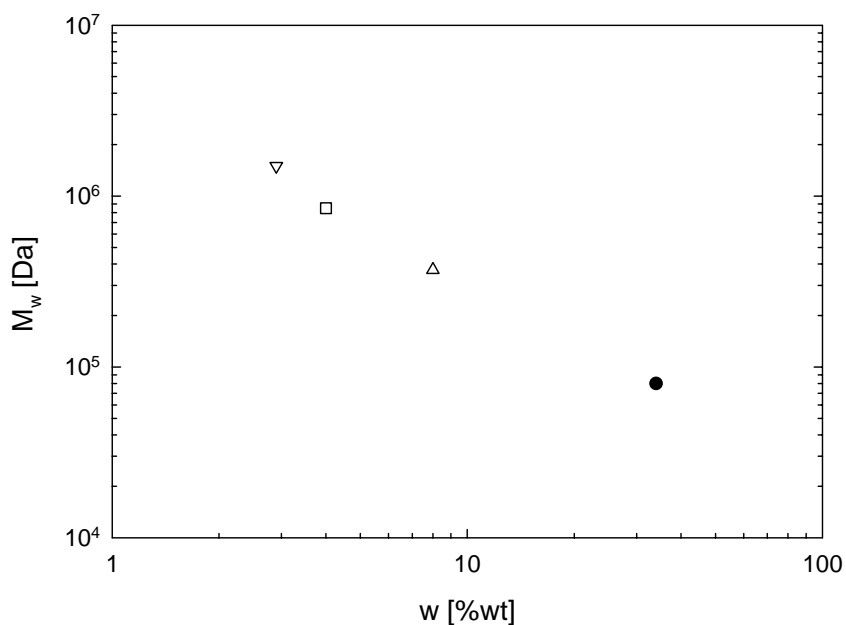


Figure 2.18. Molecular weight versus concentration for iso-viscous HPC aqueous solutions.  $\eta = 200 \text{ Pa}\cdot\text{s}$ ,  $T = 25^{\circ}\text{C}$

data are also shown for comparison. In figure 2.17, the interpolating lines of each molecular weight data set are also reported. Their slope is essentially the same and it is equal to 5.

The couple  $(w, M_w)$  at a fixed value of viscosity is plotted in figure 2.18 on a log-log plot. The obtained points are aligned, thus suggesting the following scaling law:  $\eta \propto w^n M_w^m$ . The slope of the data interpolating line is  $n/m$  and results equal to 1.16, thus leading to  $m = 4.3$ .

### *Thermoreversible gelation*

To study the effect of molecular weight on the thermoreversible gelation the most natural choice is to compare samples with the same HPC concentration. This is as easy as impractical. Indeed, at fixed concentration, the viscosities of the four HPC types are extremely different, as observable by drawing a vertical line into figure 2.17, and it is impossible to measure all of them by means of the adopted rheometer. For this reason, another criterion is used and it consists in choosing iso-viscous systems. In particular, the fixed viscosity value is 200 Pa·s ( $T=25^\circ\text{C}$ ). By drawing a horizontal line at 200 Pa·s in figure 2.17 the value of concentration, for each molecular weight, is individuated and listed in table 2.2. From now on, each sample will be identified with its own Klucel<sup>®</sup> mark followed by a number indicating the corresponding adopted concentration. For example, MF4 is the label for an aqueous solution with a HPC molecular weight equal to 850 MDa and a concentration of 4% wt.

Table 2.2 HPC concentration values for iso-viscous aqueous solutions  
( $\eta = 200$  Pa·s,  $T = 25^\circ\text{C}$ )

<i>Klucel<sup>®</sup> mark</i>	<i>Concentration [%wt]</i>
EF	34
GF	8
MF	4
HF	3.2

The four selected systems are characterized, at room temperature, by means of dynamic frequency sweep tests. The obtained results are shown in figure 2.19, where viscoelastic moduli and complex viscosity ( $\eta^*$ ) are plotted. The low frequency Newtonian plateau of  $\eta^*$  can be observed for each system, although it is not well defined for the highest molecular weight (figure 2.19.d). The value of the measured Newtonian plateau is, as established, around 200 Pa·s (aqueous solutions of HPC respect the Cox-Merz rule, 1958). As expected, the frequency of the cross-over between  $G'$  and  $G''$  decreases by increasing the  $M_w$ .

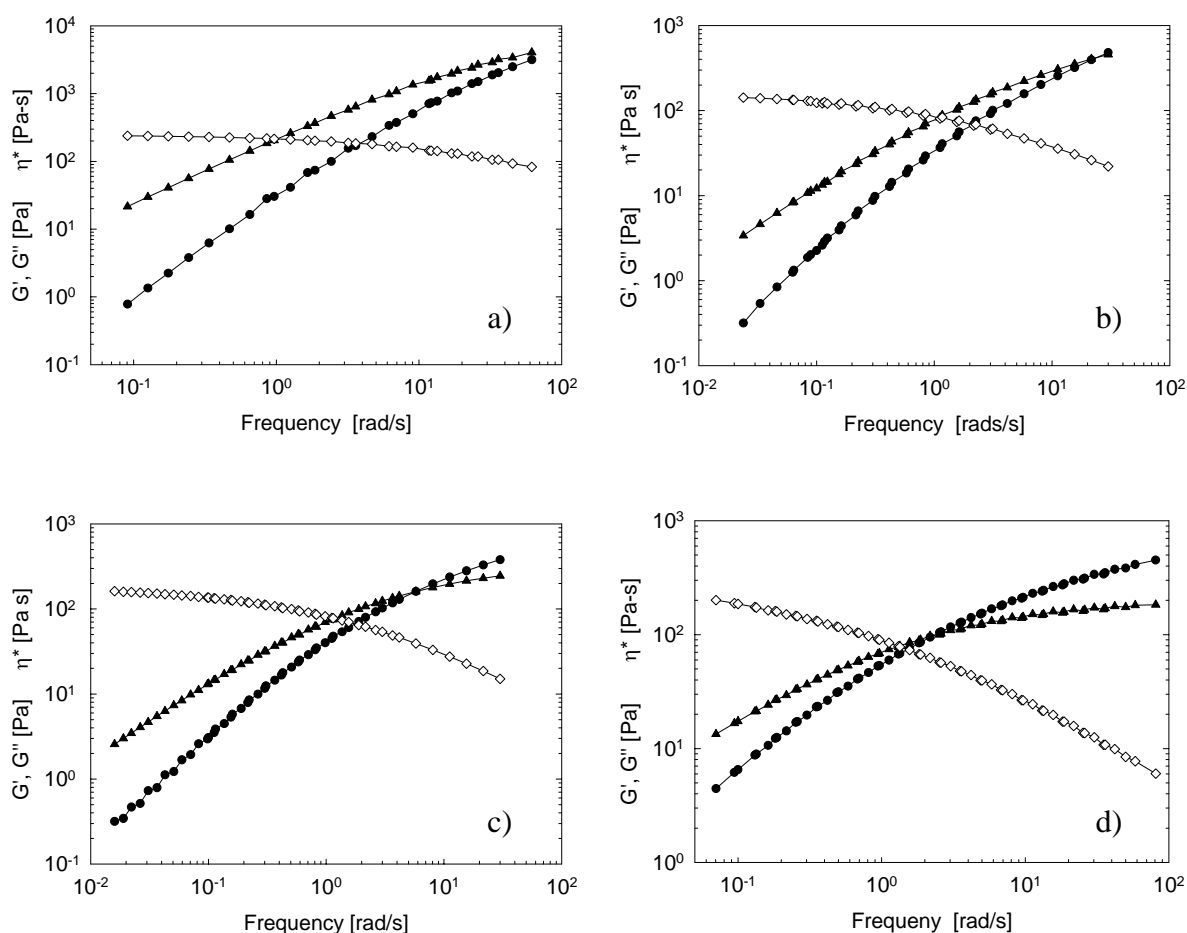


Figure 2.19. Elastic modulus ( $\bullet$ ), viscous modulus ( $\blacktriangle$ ) and complex viscosity ( $\diamond$ ) of four HPC solutions with different molecular weights and concentrations: a)  $M_w = 80000$  Da,  $w = 34\text{wt}\%$  b)  $M_w = 370000$  Da,  $w = 8\text{wt}\%$  c)  $M_w = 850000$  Da,  $w = 4\text{wt}\%$  d)  $M_w = 1150000$  Da,  $w = 3.2\text{wt}\%$ . The temperature is  $25^\circ\text{C}$ .

### *Sol-gel transition*

The experiment adopted to study the *sol-gel* transition of the EF34, GF8, MF4 and HF3.2 systems is the same described in the paragraph 2.4.2. Samples are heated from room temperature to 60°C by a thermal ramp with rates ranging from 0.1 to 10 °C/min. When heating, a small amplitude oscillatory flow is applied at a given frequency.

Figure 2.20 shows the evolution of the viscoelastic moduli as a function of temperature for the sample a) EF34, b) GF8, c) MF4 and d) HF3.2. The heating rate is 5°C/min and the oscillation frequency is 10 rad/s. All four graphs present qualitatively similar behaviors. The sol-gel transition always happens into two steps: precipitation followed by gelation. The precipitation temperature of GF, MF, HF samples is ~43°C, it is slightly lower than the  $T_p$  of the EF-type. This is probably ascribable to the dissimilar

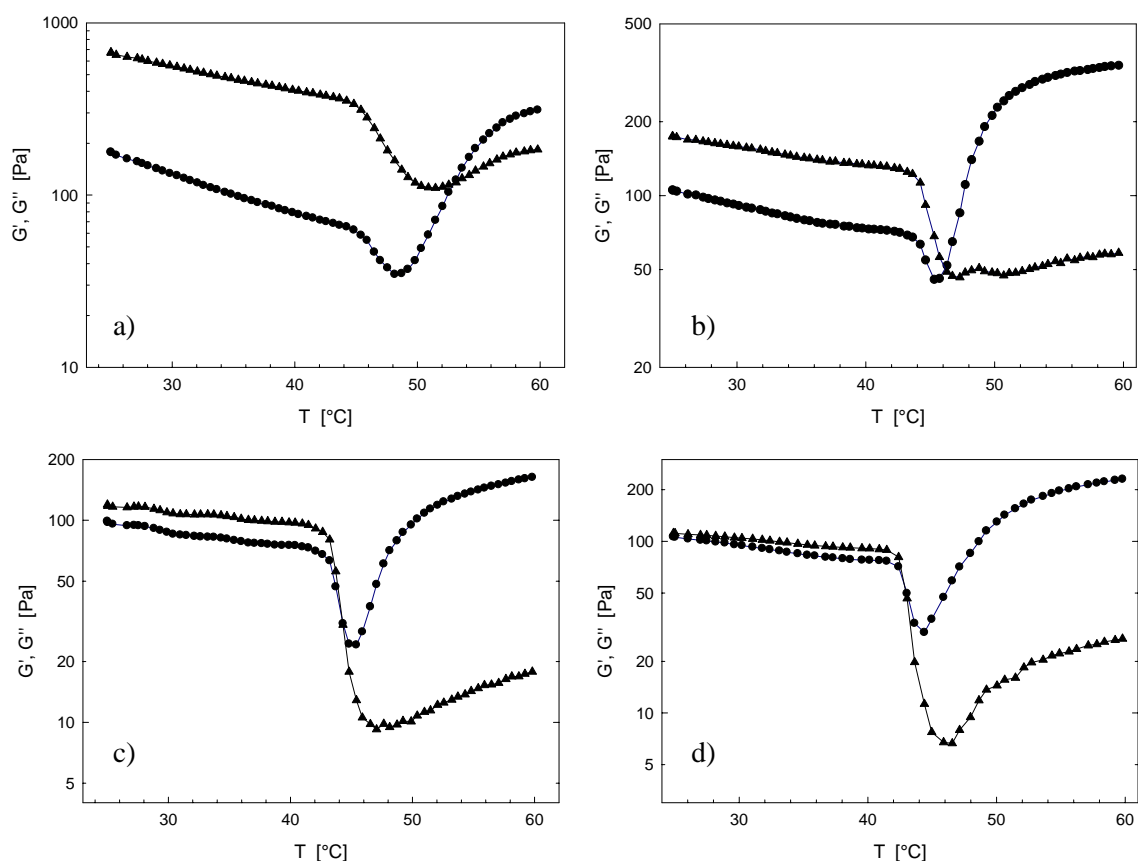


Figure 2.20. The elastic (*circles*) and viscous (*triangles*) moduli as a function of temperature during a heating ramp at 5°C/min for the sample: a) EF 34wt%, b) GF 8wt%, c) MF 4wt%, d) HF 3.2wt%. The oscillation frequency is 10 rad/s.

value of the Molar Substitution (see table 2.1) and, consequently, to the different chemical structure of the higher molecular weight HPC samples. On the one hand, this different chemical structure is a disadvantage to study the effect of  $M_w$  on the thermoreversible gelation; on the other hand, it represents a further proof that the phase transitions of the HPC aqueous solutions are driven by polymer/water interaction changes.

The cross-over temperature decreases by increasing the molecular weight. Consequently, the interval between  $T_p$  and  $T_{co}$  becomes progressively smaller, as evident in figure 2.20. Gelation, being an inter-molecular process, is more favored for longer chains. The decrease of the gelation temperature with  $M_w$  is already observed for aqueous solutions of methylcellulose (Takahashi et al. 2001).

Precipitation and gelation compete for the same HPC molecules dissolved in water. So, a precipitated chain doesn't contribute to the subsequent gel formation. This effect can be clearly observed in figure 2.21, which shows the normalized elastic modulus,  $G'/G'_{25^\circ}$ , of the samples GF8, MF4 and HF3.2 as a function of temperature, during a heating cycle at 5°C/min. The normalization is realized by dividing each elastic

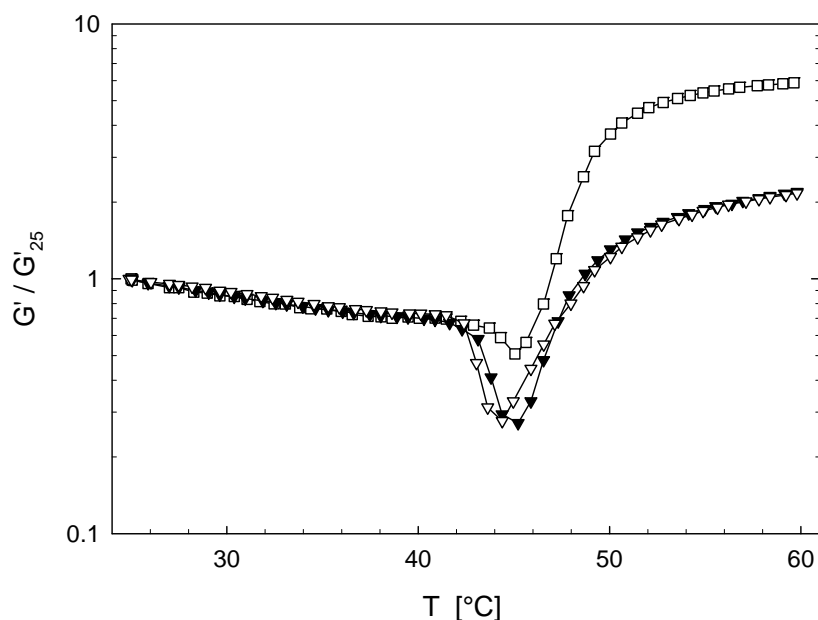


Figure 2.21. Normalized elastic modulus as a function of temperature during a heating ramp at 5°C/min for the systems: GF 8wt% (*squares*), b) MF 4wt% (*filled triangles*) and HF 3.2wt% (*empty triangles*).

modulus by its own value at room temperature. This allows for a clearer comparison among the systems. In figure 2.21 two paths can be discerned: one for GF8, and one for MF4 and HF3.2. The former presents a little precipitation followed by a strong increase of the normalized elastic modulus. The latter present a larger precipitation followed by only a moderate raise of the  $G'/G'_{25^\circ}$ . In the first case, the precipitation process subtracts fewer chains from the system, and a greater fraction of them remains dissolved in solution to form a strong gel. In the second case, precipitation is enhanced and the gel is proportionally weaker.

### ***Gel-sol transition***

The direct *sol-gel* transition is qualitatively similar for all the considered  $M_w$ , in particular the GF, MF, HF behavior is coherent with the EF one, largely studied in the previous paragraphs 2.4.2 and 2.4.3. On the contrary, the reverse *gel-sol* process is completely dissimilar, as showed in figure 2.22. The principal difference regards the *high temperature hysteresis loop*, which is inverted in comparison with the EF one (see figure 2.11), in particular  $G'_- < G'_+$  and  $G''_- < G''_+$ . Furthermore, the minimum of the storage and loss modulus is lower during the cooling than during the heating cycle. The *low temperature hysteresis loop* practically disappears. In this case, the experimental results indicated that gel breakup is not counterbalanced by re-dissolution of precipitates. The value of the viscoelastic minimum suggests that the amount of precipitated chains is greater at the end of the gel breakup than at the beginning of the gel formation. This suggests that gel destruction is coupled with precipitation of other chains, which is the exact opposite of the EF behavior. Nowadays, there are different hypotheses to justify this difference, but no definitive proof exists. No literature references are found on this matter. A first explanation relates this behaviour to the different value of the molar substitution between EF-type and higher molecular weight HPC samples (table 2.1). Another possible reason may be found in the lower value of the concentration adopted for the GF, MF and HF sample in comparison with the EF one. Indeed, between HF and EF concentration there is a gap of one order of magnitude (table 2.2), which may reasonably lead to different behaviors. Probably, to obtain a

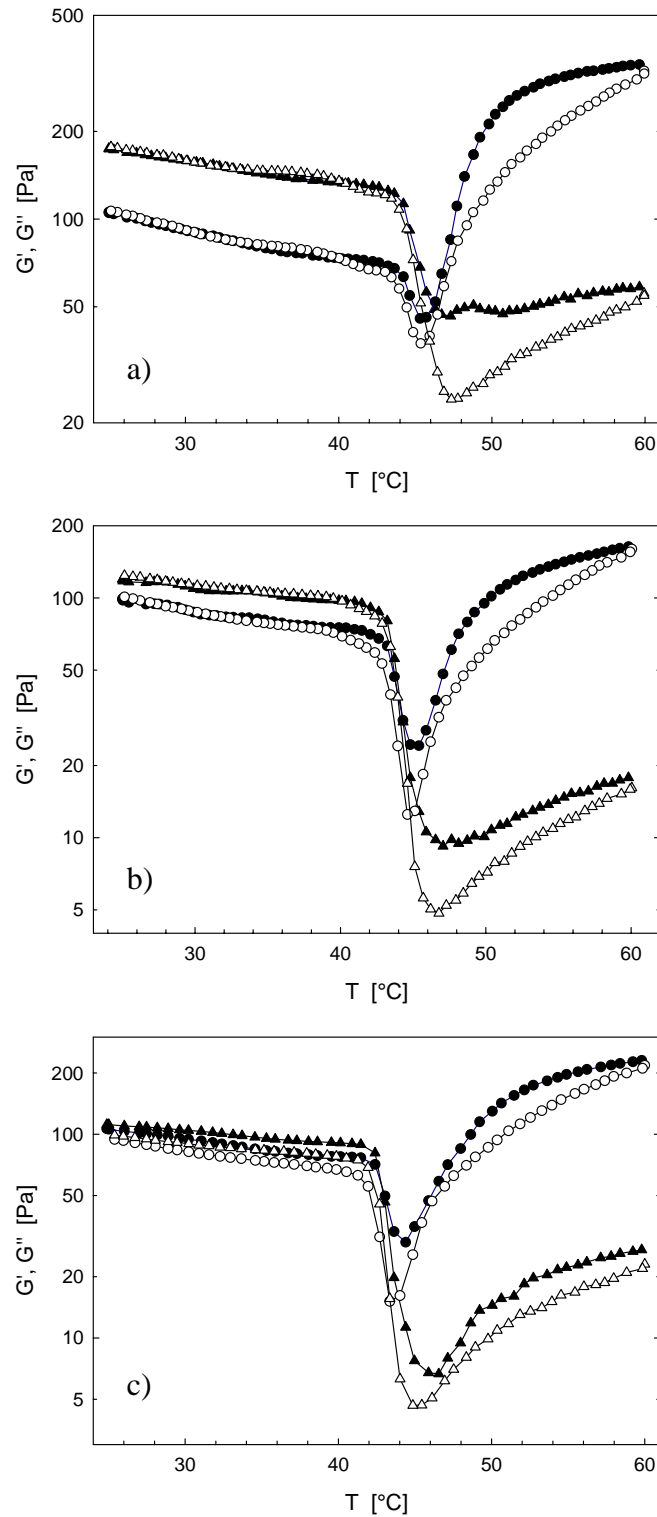


Figure 2.22. The elastic (*circles*) and viscous (*triangles*) moduli as a function of temperature during a heating/cooling cycle for the samples: a) GF 8wt%, b) MF 4wt%, c) HF 3.2wt%. The heating rate (*filled symbols*) is 5°C/min and the cooling (*empty symbols*) rate is -5°C/min. The oscillation frequency is 10 rad/s.

definite explanation on this matter, rheological measurements have to be coupled with other experimental methodologies, like calorimetric and optical tests.

## REFERENCES

- Clasen C, Kulicke WM (2001) "Determination of viscoelastic and rheo-optical material functions of water-soluble cellulose derivatives." *Prog Polym Sci* **26**:1839-1919
- Cox WP, Merz EH (1958) "Correlation of dynamic and steady-flow viscosities." *J Polym Sci* **28**:619-622
- Desbrières J, Hirrien M, Rinaudo M (1998) "A calorimetric study of methylcellulose gelation." *Carbohydr Polym* **37**:145-152
- Desbrières J, Hirrien M, Ross-Murphy SB (2000) "Thermogelation of methylcellulose: rheological considerations." *Polymer* **41**:2451-2461
- Doi M, Edwards S (1986) "The theory of polymer dynamics". Oxford, Oxford University Press
- Elias HG (1989) *Macromolecules* **1**:232
- Ford JL (1999) "Thermal analysis of hydroxypropylmethylcellulose and methylcellulose: powders, gels and matrix tablets" *Int J Pharm* **179**:209-228
- Fujii S, Sasaki N, Nakata M (2001) "Rheological studies on the phase separation of hydroxypropylcellulose solution systems." *J Polym Sci PartB: Polym Phys* **39**:1976-1986
- Guido S (1995) "Phase behaviour of aqueous solutions of Hydroxypropylcellulose." *Macromolecules* **28**:4530-4539
- Guido S, Grizzuti N (1995) "Phase separation effects in the rheology of aqueous solutions of hydroxypropylcellulose." *Rheol Acta* **34**:137-146
- Haque A, Morris ER (1993) "Thermogelation of methylcellulose. Part I: molecular structures and processes." *Carbohydr Polym* **22**:161-173
- Haque A, Richardson RK, Morris ER, Gidley MJ, Caswell DC (1993) "Thermogelation of methylcellulose. Part II: effect of hydroxypropyl substituents." *Carbohydr Polym* **22**:175-186
- Heymann E (1935) "Studies of sol-gel transformations. 1. The inverse sol-gel transformation of methylcellulose in water." *Trans Faraday Soc* **31**:846-864
- Hirrien M, Chevillard C, Desbrières J, Axelos MAV, Rinaudo M (1998) "Thermogelation of methylcelluloses: new evidence for understanding the gelation mechanism." *Polymer* **39**(25):6251-6259
- Hussain S, Keary C, Craig DQM (2002) "A thermorheological investigation into the gelation and phase separation of hydroxypropyl methylcellulose aqueous systems." *Polymer* **43**:5623-5628
- Kabra, Bhagwati P (1998) "Thermally gelling emulsions comprising cellulose ethers." U.S. Patent Application: US 96-758787 19961203
- Khomutov LI, Ryskina II, Panina NI, Dubina LG, Timofeeva GN (1993) "Structural changes during gelation of aqueous solution of methylcellulose." *Polym Sci*:320-323
- Larez-V C, Crescenzi V, Ciferri A (1995) "Phase separation of rigid polymers in poor solvents. 1. (Hydroxypropyl)cellulose in water." *Macromolecules* **28**:5280-5284
- Larson RG (1999) "The Structure and Rheology of Complex Fluids". New York, Oxford University Press
- Morawets H (1975) In *Macromolecules in solution*, 2nd ed. New York, John Wiley
- Pearson DS (1987) "Recent advances in the molecular aspects of polymer viscoelasticity." *Rubber Chem Tech* **60**:439-496
- Phillies GDJ, Quinlan CA (1995) "Analytic structure of the solutionlike-meltlike transition in polymer dynamics." *Macromolecules* **28**:160-164
- Rees DA (1972) "Polysaccharide gels, a molecular view." *Chem Ind* **19**:630-636
- Sarkar N (1979) "Thermal gelation properties of methyl and hydroxypropyl methylcellulose." *J Appl Polym Sci* **24**:1073-1087

## 2. THERMOREVERSIBLE GELATION OF AQUEOUS SOLUTIONS OF HPC

---

- Sarkar N (1995) "Kinetics of thermal gelation of methylcellulose and hydroxypropylmethylcellulose in aqueous solutions." *Carbohydr Polym* **26**:195-203
- Savage AB, Young AE, Maasberg AT (1963) In Ott E, Spurlin HM, Grafflin MW "Cellulose and Cellulose derivatives, Part II" New York, Interscience
- Takahashi M, Shimazaki M, Yamamoto J (2001) "Thermoreversible gelation and phase separation in aqueous methylcellulose solutions." *J Polym Sci PartB: Polym Phys* **39**:91-100
- Venkataraman SK, Coyne L, Chambon F, Gottlieb M, Winter HH (1989) "Critical extent of reaction of a polydimethylsiloxane polymer network." *Polymer* **30**:2222-2226
- Walker L, Wagner N (1994) "Rheology of region I flow in a lyotropic liquid-crystal polymer: The effects of defect texture." *J Rheol* **38**:1525-1547
- Winter HH, Mours M (1997) "Rheology of Polymers Near Liquid-Solid Transitions." *Adv Polym Sci* **134**:165-234
- Wirick M, Waldman M (1970) "Some solution properties of fractionated water-soluble Hydroxypropylcellulose." *J Appl Polym Sci* **14**:579-597

# CHAPTER 3

## FOURIER TRANSFORM RHEOLOGY OF DILUTE IMMISCIBLE POLYMER BLENDS

As already observed in chapter 1, LAOS measurements, coupled with SAOS ones, are potentially able to provide a really detailed characterization of morphology of micro-structured systems. The development of this experimental method has been conditioned by two main factors; firstly, it requires a sophisticated technology, both regarding experimental instruments and informatics apparatus. Secondly, nonlinear theoretical models are, inevitably, more complex than linear ones. In this work nonlinear dynamic mechanical spectroscopy is used to investigate the morphology of **dilute immiscible polymer blends**. This system is largely studied in the linear regime. Moreover, a nonlinear theoretical model, able to interpret experimental points originated by LAOS measurements, is also available.

While the great part of the works present in the literature furnishes only the average drop radius of the blend inclusions, aim of this work is to individuate a new methodology to estimate the drop size distribution of the system.

### 3.1 Immiscible polymer blends

Blending of polymers is an efficient way to create materials with specific properties, without investing in new chemistry. Indeed, blends represent a large and rapidly growing fraction of all plastics produced. The properties of the final product

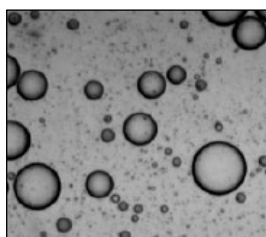


Figure 3.1. Micrograph of a dilute immiscible blend

depend not only on the properties of the constituents but also on the morphology of the system. Most polymers are thermodynamically incompatible (Krause 1978) and the blending process gives rise to a heterogeneous microstructure which can be characterized by the size, the shape and the distribution of the constitutive domains. Typically, the blend morphology is formed by inclusions of one polymer (the dispersed phase) embedded in a matrix of the other polymer (the continuous phase). In static condition, the dispersed domains generally assume a spherical shape, due to the action of the interfacial tension. A picture of a dilute immiscible polymer blend is showed in figure 3.1.

When a polymer blend is processed, it is subjected to complex flow fields which determine the final microstructure of the system. In particular, two main flow-induced phenomena may occur: one drop can deform and eventually breakup into smaller entities; conversely, two drops can collide and eventually coalesce to form one larger domain. Therefore, the interrelationship between phase morphology and rheological properties is crucial for the control of the microstructure.

#### **3.1.1 Single drop dynamic**

Significant efforts have been done in the last decades to understand the rheology/morphology correlation. This problem was first studied by Taylor (1934), who made the most basic experimental and theoretical discoveries and thus laid the groundwork for all that followed. Taylor considers the simplest case of a Newtonian drop suspended in a Newtonian fluid, subjected to a flow field. The drop deformation results from two competing phenomena. The viscous drag promotes the deformation which is resisted by the interfacial tension. The different properties of the fluid inside

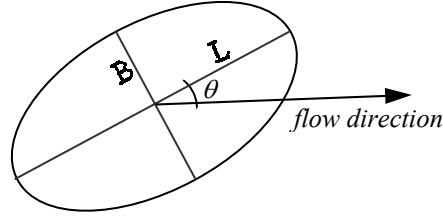


Figure 3.2. Picture of a small-deformed drop in the flow-velocity-gradient plane

and outside of the inclusion also lay a significant role. Qualitatively, the drop tends to assume a prolate shape with the major axis oriented at an angle  $\theta$  with respect to flow direction. If some critical condition is overcome, the drop does not achieve a stable stationary shape and, by the growth of hydrodynamic instabilities, it eventually breaks up.

Two quantities are typically introduced to describe the distorted drop in a planar flow: the deformation parameter,  $D$ , and the orientation angle,  $\theta$ .  $D$  is the ratio  $(L-B)/(L+B)$ , where  $L$  and  $B$  are the drop length and breadth in the plane of flow (figure 3.2).  $\theta$  has been already defined.

If gravitational settling can be neglected and if the droplet Reynolds number is small, then the drop deformation and its possible break up are controlled by two dimensionless groups: the viscosity ratio,  $\lambda$ , and the capillary number,  $Ca$ :

$$\lambda = \frac{\eta_d}{\eta_m} \quad (3.1)$$

$$Ca = \frac{\eta_m R \dot{\gamma}}{\Gamma} \quad (3.2)$$

where  $\eta_d$  is the viscosity of the dispersed phase,  $\eta_m$  is the viscosity of the external matrix,  $R$  is the radius of the undistorted spherical drop,  $\dot{\gamma}$  is the imposed shear-rate and  $\Gamma$  is the interfacial tension. The capillary number expresses the ratio between viscous and interfacial forces. Within small deformation limit, Taylor finds that the deformation parameter is proportional to the capillary number:

$$D = \frac{19\lambda + 16}{16\lambda + 16} \cdot Ca \quad (3.3)$$

There is a critical value of the capillary number,  $Ca_c$ , above which drop break up occurs. The value of the  $Ca_c$  is strongly influenced by the viscosity ratio (Grace 1982, Bentley and Leal 1986). In particular for  $\lambda \geq 4$ , no break up can be observed.

Taylor's theoretical work is for a small deformed drop at steady state. It has been extended to larger deformation, both in steady and transient flow. From one side, the analytical approach has been modified to include higher order expansions, as reviewed by Rallison (1984) and Stone (1994). On the other hand, numerical simulations of Navier-Stokes equations with boundary integral methods (Kennedy et al. 1994) gave detailed prediction of drop shape up to break up (Cristini et al. 1998). A handy though effective phenomenological model has been proposed by Maffettone and Minale (1998), christened MM-model, and it applies to generic flow fields. The authors assume that the drop retains an ellipsoidal shape at all times. The model is formulated in terms of at most six first-order, ordinary, differential equations and it is capable of describing drop deformation also in the nonlinear regime. It must be remarked that several ellipsoidal models have been proposed in the recent literature (Almusallam et al. 2000, Yu et al. 2002, Jackson and Tucker 2003, Yu and Bousmina 2003).

### 3.1.2 Interfacial stress

Once the drop evolution under a flow field is determined, it must be related to a measurable rheology quantity, in order to create the morphology/rheology link. First Batchelor (1970) and then Doi and Ohta (1991) calculated the interfacial contribution,  $\sigma_{\text{int}}$ , to the stress tensor,  $\sigma$ , coming from the deformed interface of the inclusions. The principal experimental difficulty is the extrapolation of  $\sigma_{\text{int}}$  from the measured  $\sigma$  (Jansseune et al. 2000 - 2001, Tucker and Moldenaers 2002).

### 3.1.3 Blend linear viscoelasticity – SAOS tests

A very powerful tool to characterize the microstructure of a polymer blend is represented by linear dynamic spectroscopy. When a polymer blend is subjected to a small amplitude oscillatory shear (SAOS) the droplet remains nearly spherical and the stress response is linear in strain. Experiments show that break up and coalescence

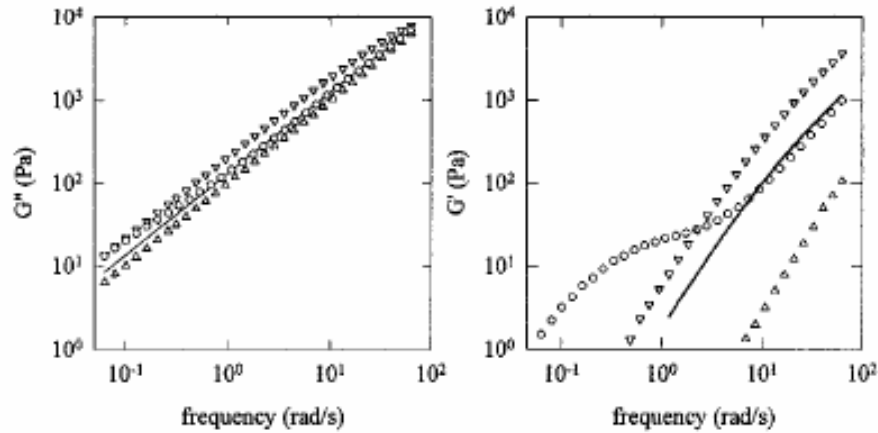


Figure 3.3. Dynamic moduli of a polymer blend ( $\circ$ ) composed by 30% of poly-dimethylsiloxane in poly-isobutene, at 23.3°C. The moduli of the pure components have been added for comparison ( $\triangle$  PIB,  $\nabla$  PDMS). The solid line represents the contribution of the components, weighted by their fraction, to the moduli of the blend (Vinckier et al. 1996).

phenomena are negligible during this kind of test. Thus, oscillatory shear offers a way to probe the properties of a blend without altering its microstructure.

In the frequency spectrum of a polymer blend an enhanced elastic response at low frequency appears, as shown in figure 3.3. This elasticity arises because deformed droplets relax back to a spherical shape under the influence of the interfacial tension, with a relaxation time,  $\tau_D$ , that scales with  $R\eta_m/\Gamma$ .  $\tau_D$  can be deduced from the  $G'$  curve in the frequency spectrum; indeed, as clearly evident in figure 3.3, the elastic modulus behavior presents a characteristic “shoulder” at a frequency  $\omega = 1/\tau_D$ . This shoulder will shift to higher frequency as the droplets size decreases. The presence of the globular inclusions has only a very slight effect on the loss modulus  $G''$  (figure 3.3).

The first theory of viscoelastic behavior imparted by interfacial tension was developed by Oldroyd (1953) for Newtonian phases of nearly spherical droplets. By using an effective-medium approach, he was able to relax the requirement of diluteness. Oldroyd’s theory was extended to linear viscoelastic phases by Palierne (1990) and Graebling and Muller (1990). Palierne provides a detailed derivation, which includes the polydispersity of droplet sizes as well as the variations in interfacial tension caused by a surfactant.

Although Palierne's theory can be written for a distribution of droplet sizes, for most cases, as observed by Graebling et al. (1993a), it is sufficient to use the volume-average droplet radius  $R_v$ :

$$R_v = \frac{\sum_i R_i \phi_i}{\sum_i \phi_i} \quad (3.4)$$

In the equation 3.4,  $R_i$  is the radius of the droplets and  $\phi_i$  the corresponding volume fraction. The complex modulus of the emulsion,  $G^* = G' + jG''$ , predicted by Palierne's model is given by:

$$G^*(\omega) = G_m^*(\omega) \frac{1 + 3\phi H(\omega)}{1 - 2\phi H(\omega)} \quad (3.5)$$

where

$$H(\omega) = \frac{4(\Gamma/R_v)(5G_d^* + 2G_m^*) + (G_d^* - G_m^*)(19G_d^* + 16G_m^*)}{40(\Gamma/R_v)(G_d^* + G_m^*) + (2G_d^* + 3G_m^*)(19G_d^* + 16G_m^*)} \quad (3.6)$$

$\phi$  is the volumetric fraction of all the drops ( $\phi = \sum_i \phi_i$ ),  $G_m^*$  and  $G_d^*$  are, respectively, the complex modulus of the matrix and of the dispersed fluid. Using the average drop radius has a negligible effect on the prediction as long as the polydispersity  $R_v/R_n$  is less than about two ( $R_n$  being the number-average drop radius of the inclusions).

Palierne model shows an excellent agreement with experiments on a variety of systems (Graebling et al. 1993a-1993b-1994, Bousmina and Muller 1993, Bousmina et al. 1995, Friedrich et al. 1995, Calvão et al. 2005, Yu et al. 2006).

Small-deformation droplet theory predicts viscoelastic behavior for Newtonian blends, and Choi and Scholwaller (1975) theory extends this to finite volume fraction. An alternative theory for viscoelastic blend has been proposed by Bousmina (1999). He, based on the Kerner's model (1956), developed a constitutive equation taking into account the effect of the interfacial tension and analyzing the circulation of the fluid inside the dispersed drops. The Lee and Park (1994) theory can be adapted to predict viscoelastic behavior (Lacroix et al. 1997), though the extension to viscoelastic phases is heuristic rather than rigorous.

#### **3.1.4 Blend nonlinear viscoelasticity – LAOS tests**

All the above exposed rheological methodologies are able to estimate the average drop size of the dispersed phase, but generally do not provide details on the drop size distribution. To define it, great improvements into optical techniques have been done (Ramic et al. 2000, Caserta et al. 2004). Anyway, these optical methods are limited to transparent emulsions.

In this work a new rheological methodology for the estimation of drop size distribution of dilute immiscible polymer blend is proposed. The procedure exploits the capabilities of Large Amplitude Oscillatory Shear (LAOS) flows to discriminate the behavior of drops of different size. The method is already tested on synthetic data obtained by mimicking rheological response of polydisperse emulsions (Grosso and Maffettone 2004). It is here applied to real experimental data set.

The procedure utilizes the MM-model to describe the drop dynamics under LAOS. The diluteness of the blend justifies the use of single drop theory. The interfacial tension arising from the deformed interfaces of the droplets is calculated by means of Batchelor theory (1970). Details about both the models and the entire procedure will be discussed in paragraph 3.5.1.

#### **3.2 Materials**

The studied blend is formed by poly-isobutylene (PIB, Parapol 1300 from Exxon) and poly-dimethylsiloxane (PDMS, Rhodorsil 47V200000 from Rhône-Poulenc). PIB and PDMS are immiscible; they are very stable, transparent at room temperature and exhibit a well defined Newtonian plateau in the shear-rate range adopted in this work (figure 3.4). At the same time, they possess a relative high viscosity and some degree of elasticity, which make them similar to industrial thermoplastic blends. For all these reasons, PIB/PDMS emulsion is considered a model system, it is largely studied in the literature, by means of both rheological and optical techniques (Vinckier et al. 1998, Minale et al. 1999, Guido et al. 2000, Jansseune et al. 2000, Wannaborworn et al. 2002).

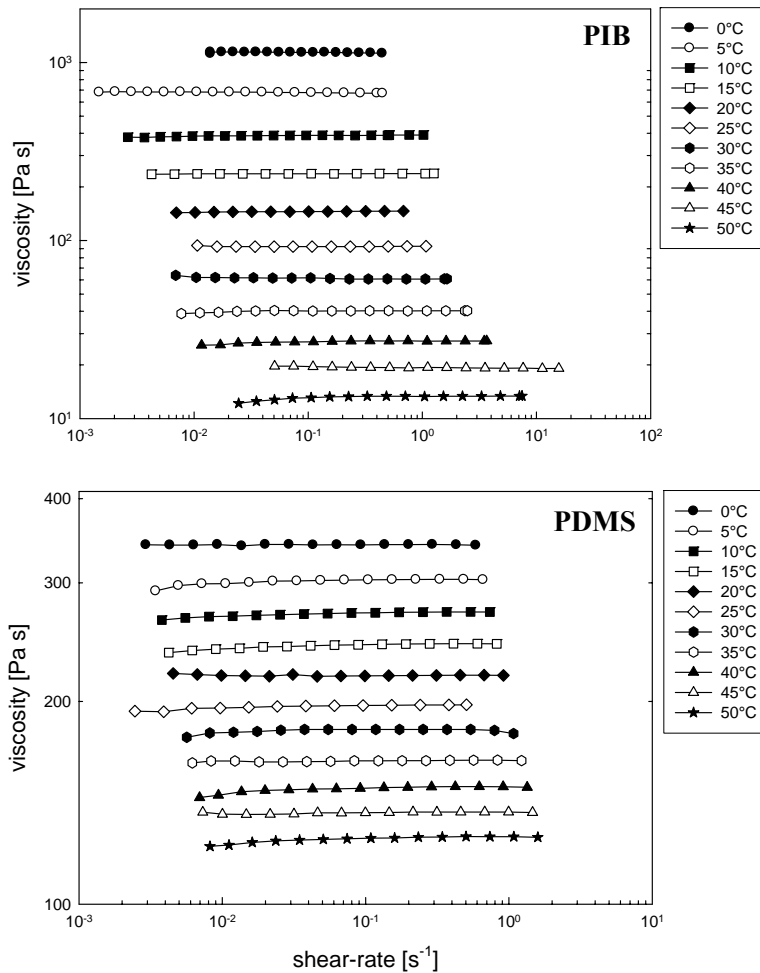


Figure 3.4. Viscosity versus shear-rate for poly-isobutylene (PIB, Parapol 1300 from Exxon) and poly-dimethylsiloxane (PDMS, Rhodorsil 47V200000 from Rhône-Poulenc) at different temperatures.

The main physical properties of poly-isobutylene and poly-dimethylsiloxane are reported in table 3.1, at the temperature  $T = 30^\circ\text{C}$ . The molecular weights and densities are provided by the manufacturers, the polymer viscosities are obtained with traditional rheological measurements, whereas the interfacial tension,  $\Gamma$ , comes from literature (Sigillo et al. 1997). It should be remarked that, for these physical conditions, the viscosity ratio,  $\lambda$ , is equal to 3 and it is larger enough to avoid break-up phenomena. Buoyancy effects can be excluded in view of the close values of the polymer densities and their high viscosities.

The volumetric fraction of the blend,  $\phi = \text{PDMS/PIB}$ , is equal to 0.1. This value is

small enough to consider the system dilute. The samples were prepared by hand mixing the desired amounts of the two polymers in a beaker until a homogeneous white cream is obtained. The air incorporated has been removed by at least one day stay under vacuum. Usually, this manual preparation determines an average drop size of about  $1\div 10\ \mu\text{m}$  (Grizzuti and Bifulco 1997). The experiments were carried out with samples obtained with this procedure. Sometimes, the blend was also subjected to a precise flow history in order to modify the microstructure. In particular, to favor drop coalescence, a shear flow of  $3\ \text{s}^{-1}$ , applied for an hour, at  $40^\circ\text{C}$ , was imposed.

Table 3.1. Main physical properties of the PDMS/PIB system at  $30^\circ\text{C}$

<i>Polymer</i>	<i>Formula</i>	<i>Molecular Weight [Da]</i>	<i>Density [Kg/m<sup>3</sup>]</i>	<i>Viscosity [Pa·s]</i>	<i>Interfacial tension [mN/m]</i>
PDMS	$[-\text{Si}(\text{CH}_3)_2\text{O}-]_n$	1300	971	175	3
PIB	$[-\text{CH}_2\text{C}(\text{CH}_3)_2-]_n$	200000	894	57	

### 3.3 Experimental Realization

#### 3.3.1 Set-up

Experimental set-up adopted in this work for Fourier Transform Rheology is based on the modification and extension of a commercial strain controlled ARES rheometer from TA-Instrument. The ARES rheometer is equipped with an electromagnetically compensated torque transducer (2KFRTN1) that can read a torque within the range  $0.002\div 200\ \text{mN}\cdot\text{m}$  and normal forces within  $0.02\div 20\ \text{N}$ , as specified by the manufacturer. The motor is a standard STD motor with a frequency range from  $10^{-5}$  to  $500\ \text{rad/s}$  and an angular deformation ( $\Omega$ ) of  $0.05$  to  $500\ \text{mrad}$ . The rotation frequency can be varied between  $0.001$  and  $100\ \text{s}^{-1}$ . The electrical signals coming from both motor and torque transducer possess an amplitude ranging from  $0$  to  $5\ \text{V}$  and they can be easily withdrawn by using the appropriate BNC output located in the Signal Panel on the back of the instrument. The raw data are digitized with a 16-bit analog to digital

converter (ADC) from National Instruments, labeled PCI\_6251. The data handling and elaboration is performed by a home-written LabView routine. The experimental set-up is displayed in figure 3.5.

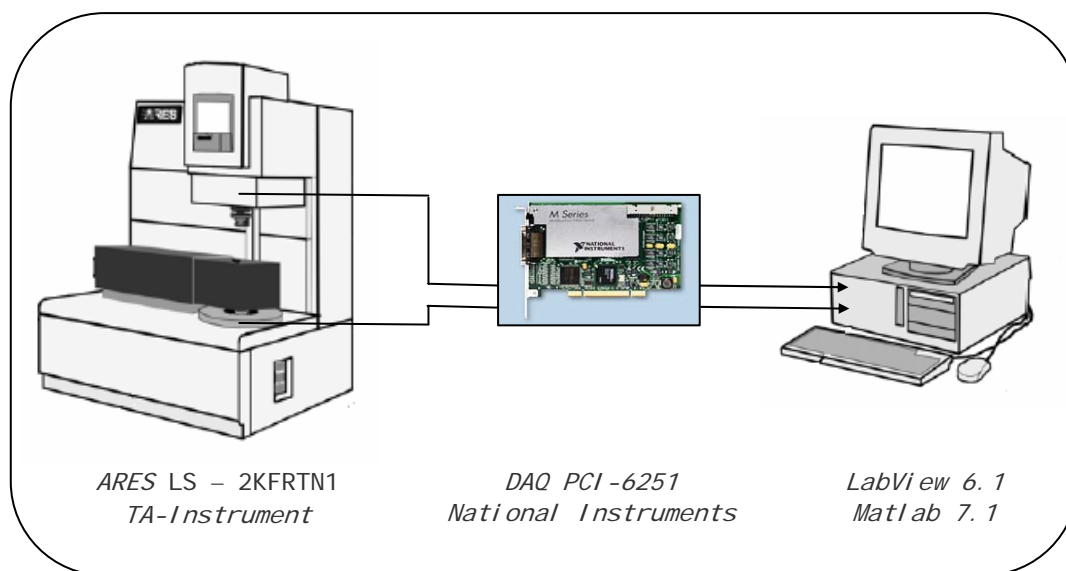


Figure 3.5. Experimental Set-up

As already stressed in the literature (Wilhelm et al. 1999), a crucial point for the Fourier Transform Rheology is represented by signal to noise ratio (S/N). The S/N can be defined as the ratio of the amplitude of the highest peak in the Fourier spectrum divided by the standard deviation of the noise. In general, there are essentially two ways to improve a ratio: decrease the denominator or/and increase the numerator. To decrease the denominator special care must be taken to avoid, or at least reduce, mechanical and electrical noises. The spectral range for both sources is typically between 0.01 Hz and 100 Hz. For the mechanical case, vibration of the building, resonances of the transducer, sonic disturbances, e.g. footsteps, fall into the just indicated frequency range (Skoog 1992). For this reason the rheometer is kept in an isolated, rigid and mechanical stable environment. To minimize the electric noise level, all the external connections are made of double-shielded BNC cables (RG 223/U by Pomona). However, it must be noted that electric disturbances originated by the circuit plans of the ARES rheometer itself cannot be avoided. In general, those electric noises are not random, but located at specific frequencies, i.e. 50 Hz in Europe and 60 Hz in North America. So, they cannot be

eliminated, but can be easily recognized.

The improvement of the numerator of the S/N ratio is favored, first of all, by the very sensitive torque transducer mounted on the rheometer. The use of a 16 bit, rather than 8 bit or 12 bit, ADC card allows a clear detection of very weak signals. Moreover, a considerable improvement of the S/N ratio can be obtained by choosing an appropriate geometry. In particular, in this work, a cone and plate geometry is adopted. The diameter is the larger available (50 mm) and is chosen to maximize the contact surface between sample and plate and, therefore, to improve the torque signal. The cone angle,  $\alpha$ , is 0.02 rad. The value of  $\alpha$  does not affect S/N ratio, but it holds an important role anyway. Indeed, reminding that the upper angular deformation limit is 500 mrad, the selected cone angle allows to reach a maximum strain amplitude,  $\gamma = \Omega/\alpha$ , of 25 (2500%). This large value is very important in LAOS experiments.

All the just described contrivances lead to a S/N ratio higher than  $10^4$ .

Finally, it must be observed that the linear viscoelastic properties of the studied polymer blend are measured by means of the ARES rheometer without any modification.

### 3.3.2 Data acquisition system

As already observed in the paragraph 3.3.1, the acquisition of the electric signals and their successive elaboration is realized through a program written in LabView.

Before starting the acquisition, two main parameters have to be set: scan rate,  $r$  [=] pts/s, and number of total points,  $N_p$ . They are the same for both the channels (ch1: motor signal, ch2: transducer signal). The ratio between  $N_p$  and  $r$  indicates the time required for the entire acquisition,  $t_{acq} = N_p/r$ . The oscillation cycles collected during  $t_{acq}$  depend on the imposed deformation frequency ( $\omega$ ). Typical values of  $r$  and  $N_p$  are 1000 pts/s and 80000 pts respectively, thus  $t_{acq} = 80$  s. If the motor imposes a deformation frequency of 0.1 Hz, 8 cycles will be acquired. It must be observed that the higher values of  $r$  and  $N_p$ , the higher the S/N ratio (Bracewell 1986; Ramirez 1995; Wilhelm 2002), but the longer the  $t_{acq}$  and the heavier the stored files. So, the typical values of  $r$

and  $N_p$  (see above) optimize between these two opposite factors.

The raw data coming from both motor and transducer, containing respectively the digitized signal of strain and torque, are collected into two columns in a .txt file. They are subsequently transformed into the corresponding Fourier spectra, by means of Finite Fourier Transform algorithm (Bracewell 1986) with Matlab 7.1.

The Fourier spectrum of motor signal allows controlling the quality of the applied deformation. Indeed, it should be a perfect sine wave and, consequently, it should contain only the fundamental harmonic at the imposed oscillation frequency.

The Fourier spectrum of the transducer signal, as already observed, contains only the fundamental harmonic in the linear regime (SAOS), and also odd multiples of the fundamental harmonic in the nonlinear regime (LAOS). For the investigated polymer blend, the 3<sup>rd</sup> and the 5<sup>th</sup> overtones can be clearly detected in the power spectrum for deformations  $\gamma_0 > 100\%$ .

### 3.3.3 Signals' calibration

The periodic electrical signals coming from both motor and transducer are expressed in Volt. They must be translated into the corresponding physical parameters.

The amplitude of the motor signal ( $\Delta V_m$ ) is proportional to the angular displacement ( $\Omega$ ):

$$\Omega = k_m \cdot \Delta V_m \quad (3.7)$$

The ideal value of proportionality coefficient  $k_m$  can be easily obtained. It is equal to the ratio between the upper angular deformation limit (= 0.5 rad) and maximum electrical signal amplitude (= 5 Volt), hence  $k_m = 0.1$  rad/Volt. To calculate the effective value of the proportionality coefficient, some dynamic experiments, at different deformation displacements, are carried out. The corresponding motor signal amplitude is also acquired. In figure 3.6.a the value of the angular deformation is reported as a function of motor electric potential difference. Experimental points fall a line with a slope of 0.1, which represents the real value of  $k_m$ . It is practically coincident with the ideal one.

The amplitude of the transducer signal ( $\Delta V_t$ ) is proportional to the measured torque ( $M$ ). The 2KFRTN1 transducer can run into two different modalities: "low range"

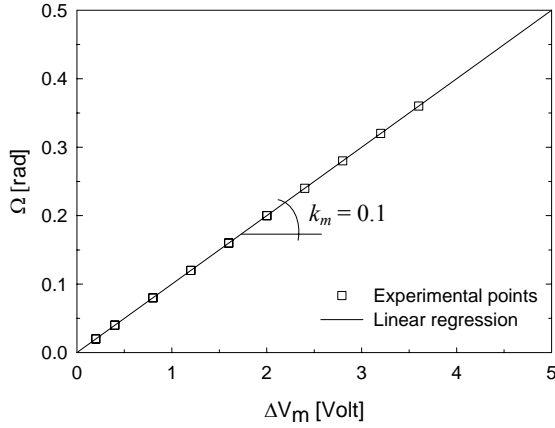


Figure 3.6.a. Angular displacement as a function of motor electric signal amplitude

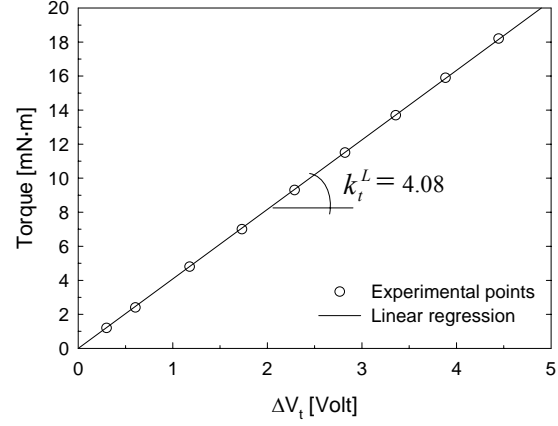


Figure 3.6.b. Measured torque as a function of transducer electric signal amplitude.

(0.002÷20 mN·m) for weak signals and “high range” (0.2÷200 mN·m) for strong signals. For this reason, two proportionality coefficients exist:

$$\text{Low range) } M = k_t^L \cdot \Delta V_t \quad (3.8.a)$$

$$\text{High range) } M = k_t^H \cdot \Delta V_t \quad (3.8.b)$$

The ideal value of  $k_t^L$  is equal to ratio between the upper “low range” torque limit (= 20mN·m) and the maximum electrical signal amplitude (= 5 Volt):  $k_t^L = 4 \text{ mN}\cdot\text{m/Volt}$ . The effective value of  $k_t^L$  is obtained by means of the same experiments used to calculate  $k_m$ . In figure 3.6.b the measured torque as a function of  $\Delta V_t$  is reported. From a linear regression of data in figure 3.6.b one obtains  $k_t^L = 4.08$ . Regarding the high range proportionality coefficient,  $k_t^H$ , its ideal value is 40 mN·m/Volt, while the regressed one is 40.62 mN·m/Volt.

The importance of signal’s calibration will become apparent in the section 3.5 which deals with model/experiments comparison. In particular, it will be useful to pass from  $\Delta V_t$  to the corresponding tangential stress  $\sigma$ , rather than the corresponding torque  $M$ . For this reason, equations 3.8.a and 3.8.b have to be slightly modified. The relationship between torque and tangential stress, for a cone and plate geometry, is:

$$\sigma = \frac{3M}{2\pi R_p^3} \quad (3.9)$$

where  $R_p$  is the plate radius. Inserting the equation 3.9 into the 3.8.a and 3.8.b, the following expressions are obtained:

$$\sigma = \frac{3k_t^L}{2\pi R_p^3} \Delta V_t = k_\sigma^L \Delta V_t \quad (3.10.a)$$

$$\sigma = \frac{3k_t^H}{2\pi R_p^3} \Delta V_t = k_\sigma^H \Delta V_t \quad (3.10.b)$$

where  $k_\sigma^L = 125$  Pa/Volt and  $k_\sigma^H = 1242$  Pa/Volt.

### 3.4 Experimental results

#### 3.4.1 SAOS measurements

The adopted experimental protocol plans linear viscoelastic measurements before nonlinear ones in order to obtain a preliminary, but fundamental, characterization of the system. SAOS tests are carried out in a frequency range from 0.1 to 10 Hz, at 30 °C. The amplitude of the imposed strain is 50% that is well within the linear region. In figure 3.7 the elastic modulus of the PIB (matrix), the PDMS (dispersed phase) and the blend is reported. The  $G'$  of the neat polymers shows the typical low frequency slope

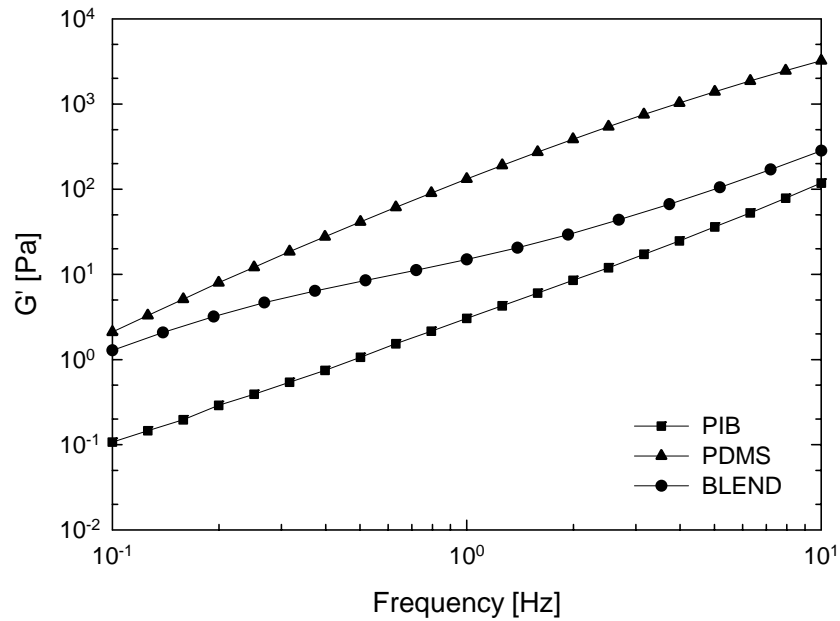


Figure 3.7. Dynamic elastic modulus of the pure component and the blend as a function of frequency, at 30°C. The imposed deformation is equal to 50%.

( $\cong 2$ ) of Newtonian fluids. The  $G'$  of the blend, at high frequencies, is a weighted average of the pure components, whereas, at low frequencies, it exhibits an enhanced elastic response arising from the drop interface relaxation. The  $G'$  “shoulder” position and the low frequency additional elastic contribution represent two fundamental information about blend morphology. The presence of droplets has a very small effect on the viscous modulus and for this reason  $G''$  is not reported in figure 3.7.

From SAOS measurements the average volumetric radius,  $R_v$ , of the disperse phase can be obtained by using the Palierne’s model (1990). This model, when the blend’s components are Newtonian, can be approximated with the following equation (Graebling et al. 1993a):

$$R_v \cong \frac{4\Gamma\tau_D}{\eta_m} \frac{10(\lambda+1) - 2\phi(5\lambda+2)}{(19\lambda+16)[2\lambda+3 - 2\phi(\lambda-1)]} \quad (3.11)$$

where  $\eta_m$  is the matrix viscosity and  $\tau_D$  is the characteristic relaxation time of the disperse phase. A first indication of  $\tau_D$  can be obtained from figure 3.7. It is the inverse of  $G'$  shoulder frequency. A more precise evaluation of  $\tau_D$  can be drawn from the relaxation time spectrum,  $H(\tau)$ , derived from the viscoelastic moduli of the blend (figure

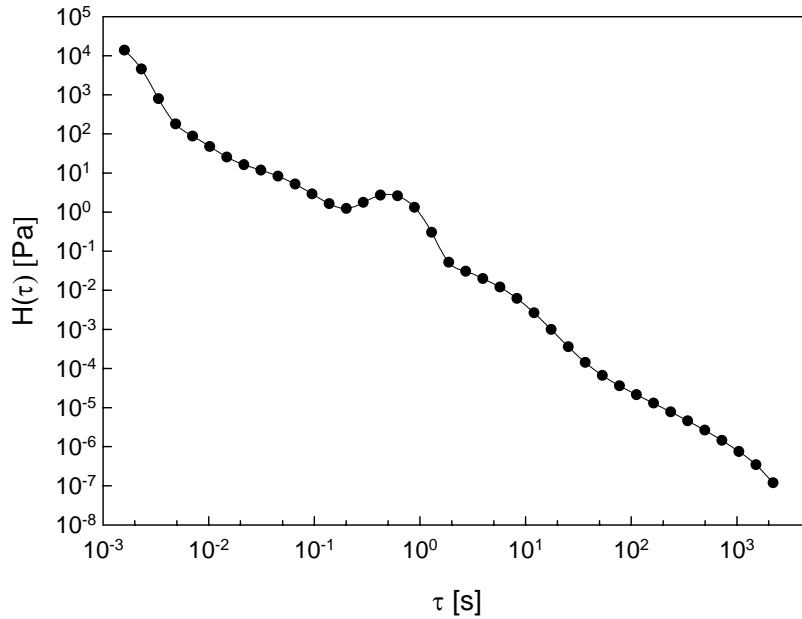


Figure 3.8. Relaxation time spectrum of the blend (10% PDMS, 90% PIB), at 30°C.

3.8). The local maximum visible in the figure 3.8 is representative of the interfacial relaxation time. For the case under investigation,  $\tau_D$  is equal to 0.61 seconds, which leads to  $R_v = 6.5 \mu\text{m}$ . It must be noted that  $H(\tau)$  contains contributions coming from the pure components,  $H(\tau)_{comp}$ , and from the interfacial tension,  $H(\tau)_{int}$ . A more accurate determination of  $\tau_D$  would have required the calculation of  $H(\tau)_{int} = H(\tau) - H(\tau)_{comp}$ . However, when the local maximum of  $H(\tau)$  is well defined like in figure 3.8, the more accurate procedure does not lead to a significant variation of  $\tau_D$  (Vinckier et al. 1996); for this reason it has not been applied in this work.

It must be noted that the Palierne model can also be used to extract the entire sphere-size distribution of an incompatible polymer blend. The procedure is very complex and it is seldom applied (Friedrich et al. 1995).

Figure 3.9 shows the elastic modulus of five different blends. Each blend is labeled with a capital letter. The assignation of letters is simply related to the chronological order of the performed tests. Blends A, C, D and E are not subjected to any pre-treatment. So, their morphology is only influenced by the hand mixing

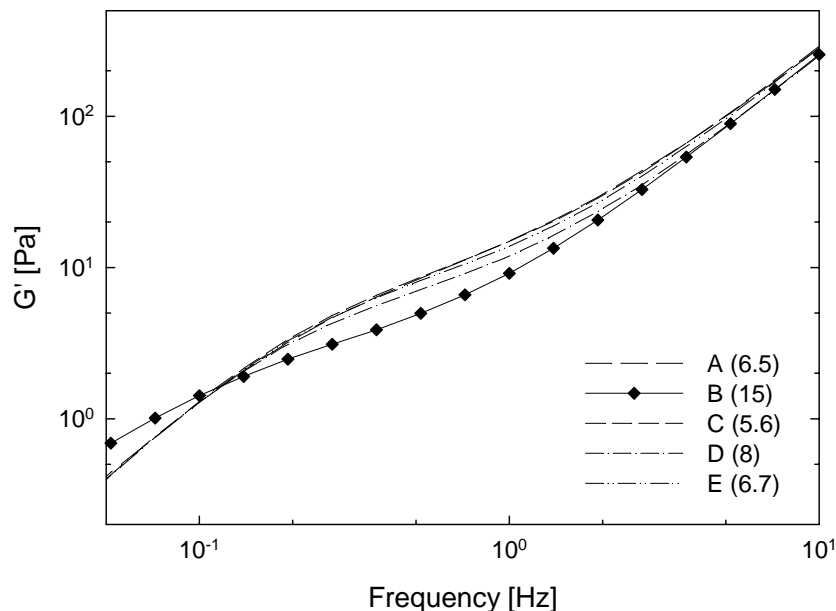


Figure 3.9. Dynamic elastic modulus versus frequency of five different blends, at 30°C. The amplitude of the imposed deformation is 50%. The values put in brackets into the legend indicate the average drop radius of the corresponding emulsion.

procedure. For this reason,  $G'$  of these four systems is similar. On the contrary, the blend B is subjected to a pre-shear of  $3 \text{ s}^{-1}$  for an hour, at  $40^\circ\text{C}$ . This temperature causes the viscosity ratio to rise up to 5.4, thus excluding the occurrence of break-up phenomenon. At  $40^\circ\text{C}$  drop coalescence is enhanced, so, the average drop radius of the blend B should be bigger than the other ones. This fact is confirmed by the figure 3.9. Indeed, the elastic modulus of the blend B, compared with the others reported in the same figure, presents a “shoulder” at a lower frequency, thus suggesting a longer relaxation time. Moreover, the elastic contribution at low frequencies shifts at larger values.

The average drop radius of these five blends is determined with the above-mentioned procedure, by means of time relaxation spectrum. The results are listed in table 3.2. The system B presents  $R_v = 15 \text{ }\mu\text{m}$ , which is about twice as big as the other blend average drop radius.

It must be noted that the choice of these specific five systems – four similar and one different - is not casual but it is related to the successive nonlinear measurements. Indeed, it will be very important not only to test LAOS ability describing blend micro-structure, but also verifying LAOS sensitivity to a small or large morphology change.

Table 3.2. Average drop radius of five different blends

<i>Sample</i>	<i>Relaxation time [s]</i>	<i>Average drop radius [<math>\mu\text{m}</math>]</i>
Blend A	0.6	6.5
Blend B	1.4	15
Blend C	0.53	5.6
Blend D	0.7	8
Blend E	0.62	6.7

### 3.4.2 LAOS measurements

During LAOS measurements, break-up and coalescence phenomena may occur and they are more and more enhanced as the deformation increases. The break-up is avoided or at least greatly thwarted by working at relatively high temperature ( $T =$

30°C) which correspond to a viscosity ratio of 3. The coalescence cannot be totally excluded, anyway, it is reduced by using a small volume fraction ( $\phi = 0.1$ ) of the dispersed phase. The sample stability check is done through frequency sweep test running at the beginning, at the middle and at the end of a LAOS experience. The overlapping of  $G'$  spectrum is considered a proof of a constant morphology.

When a polymer blend is subjected to a large amplitude oscillatory shear,  $\gamma = \gamma_0 \sin(\omega t)$ , with  $\gamma_0 > 100\%$ , a nonlinear response is observed. A typical experimental result is shown in figure 3.10, where the applied strain and the corresponding tangential stress are reported both in the time and in the frequency domain. The imposed deformation is equal to 800% and oscillates at  $\omega = 0.1$  Hz (figure 3.10.a), it is a perfect sine wave, as confirmed by the related Fourier spectrum (figure

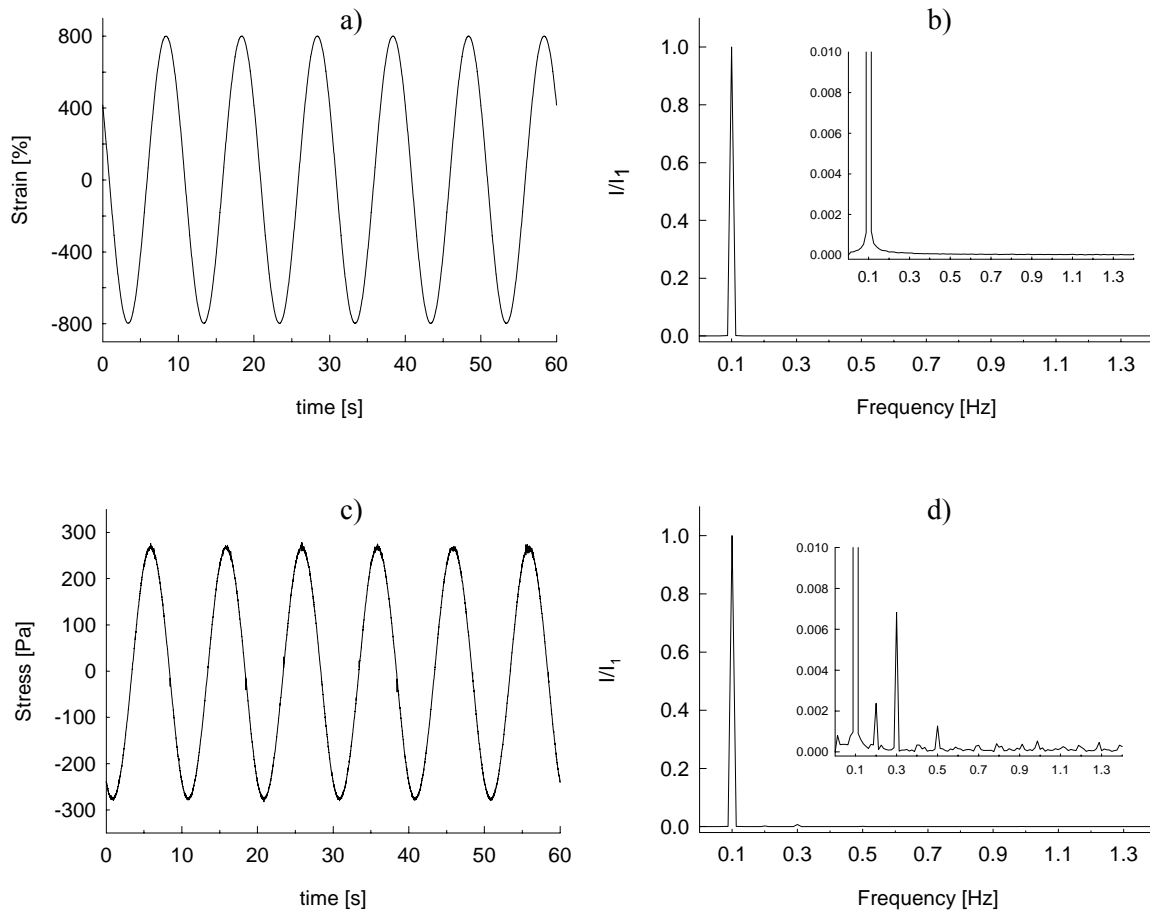


Figure 3.10. Motor and transducer signals in the time domain (a,c) and the corresponding Fourier spectra (b,d) for a polymer blend, at 30°C.

3.10.b) where only the fundamental harmonic appears. The nonlinear response of the system cannot be easily observed in the time domain, the stress signal (figure 3.10.c) looks like a sinusoidal waveform. On the contrary, in the corresponding power spectrum (figure 3.10.d) the occurrence of a third and a fifth peak is clearly evident. It must be noted that the Fourier spectra report the absolute value of the overtones, normalized with the first harmonic ( $I_k/I_1$  or equivalently  $I_{k1}$ ). This kind of representation is largely adopted in the literature.

LAOS experiences are performed also for the pure component in order to establish the origin of the nonlinearity. Is it a blend own property or does it derive from the pure polymer too? In figures 3.11.a and 3.11.b the Fourier spectra of PIB and PDMS are reported; the imposed oscillatory deformation is the same applied to the blend (figure 3.10.a). PIB power spectrum presents no odd multiple harmonics (figure 3.11.a), thus confirming its Newtonian behavior. On the contrary, PDMS power spectrum reveals the occurrence of a third peak,  $I_{31}$ , clearly distinct from the background noise (figure 3.11.b). This was predictable, as poly-dimethylsiloxane presents a nonlinear shear-thinning behavior starting from a shear rate  $\dot{\gamma} \sim 1 \text{ s}^{-1}$  (figure 3.4) and, the amplitude of the applied shear rate is  $\dot{\gamma} = \gamma_0 \cdot \omega = 0.8 \text{ s}^{-1}$ . Anyway, PDMS is the 10% of the blend and consequently its own contribution to the nonlinear response of the system is only one tenth of the  $I_{31}$  reported in figure 3.11.b and can be neglected. Therefore, the

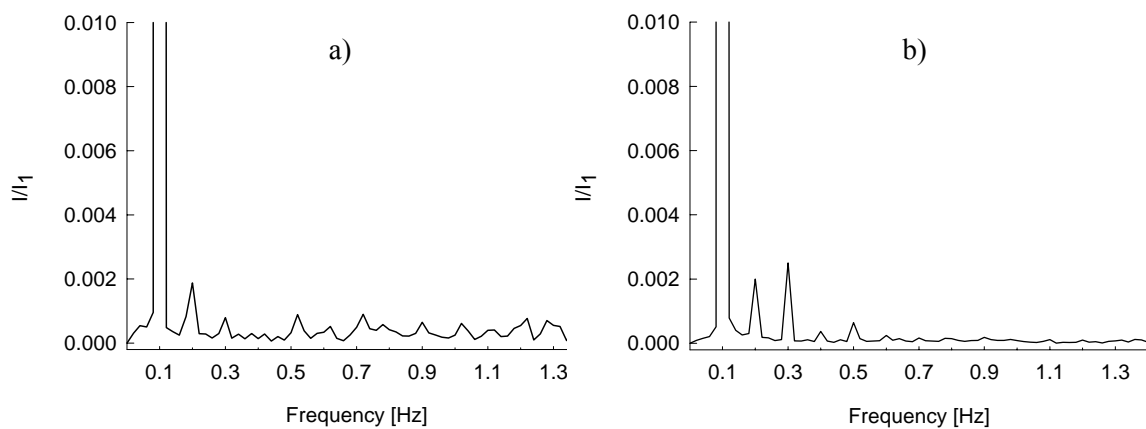


Figure 3.11. Normalized Fourier spectra of a) PIB and b) PDMS. The applied deformation is 800%, the oscillation frequency is 0.1 Hz

odd harmonics present in the emulsion power spectrum are mainly imputable to the interfacial stress coming from the deformed drops.

LAOS tests are carried out at different strain amplitudes,  $\gamma_0 \in [100\% \div 1600\%]$ . The lower limit represents the first deformation able to produce a third harmonic clearly distinct from the background noise; the upper limit is conditioned by the sample leakage from the plate's edge. The oscillation frequency is 0.1 Hz. In figure 3.12, the measured absolute value of the third harmonic normalized with the first one,  $I_{31}$ , is reported as function of the strain for the polymer blend. It presents a non monotonic trend and reaches a maximum at intermediate deformation. Even if the value of  $I_{31}$  is low, it is largely reproducible. Indeed, by performing different LAOS experiences on the same blend, the experimental error is less than 0.5%. In the same figure,  $I_{31}$  of PIB and PDMS is also shown for comparison. The contribution of both pure components is weighted by the respective amount used in the blend. Experimental data reported in figure 3.12 underline again that the nonlinearity comes almost exclusively from the interfacial stress.

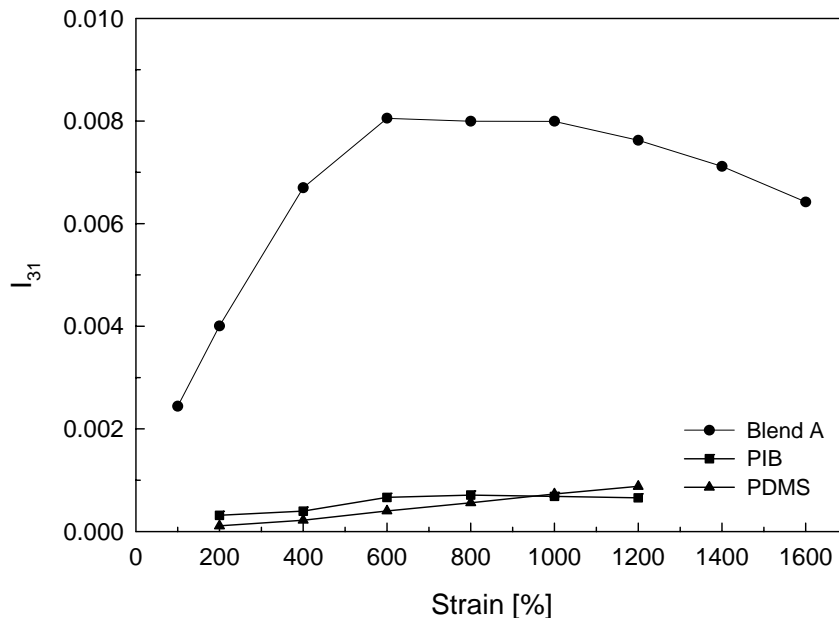


Figure 3.12. Absolute value of the third harmonic normalized with the first one as a function of the applied strain for the blend and the pure components. The oscillation frequency is 0.1 Hz

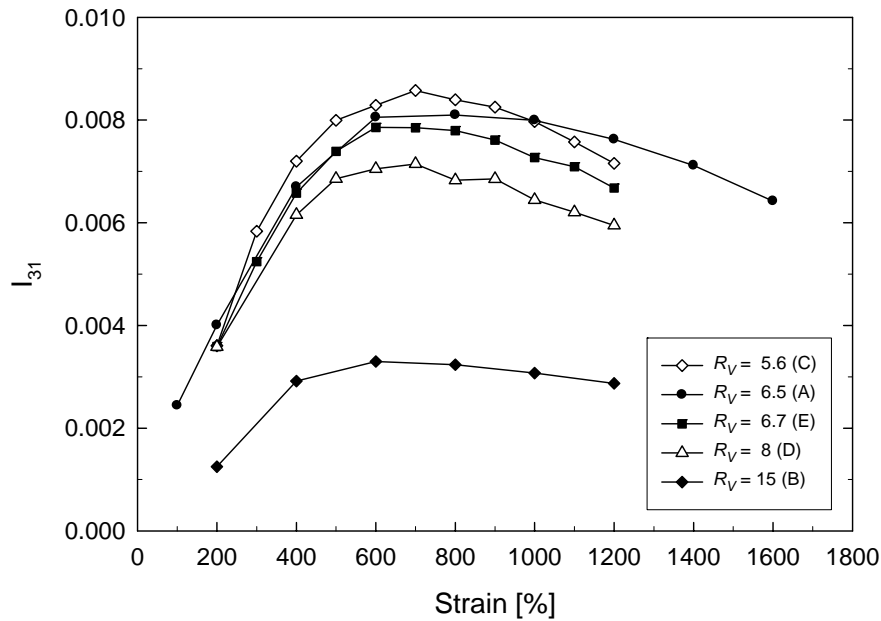


Figure 3.13. Absolute value of the third harmonic normalized with the first one as a function of the applied strain for five different blend morphologies. The oscillation frequency is 0.1 Hz ( $T = 30^\circ\text{C}$ )

The just described LAOS experimental procedure is applied to the five blends introduced in the section 3.4.1. By linear measurements, it is known that systems A, C, D and E possess a similar microstructure, while system B is quite dissimilar. LAOS experimental results are shown in figure 3.13, where  $I_{31}$  as a function of strain amplitude is reported for each blend. The graph presents five distinct curves. So, the first interesting outcome is the ability of LAOS technique to discriminate different morphologies. In addition, the distinction of the five  $I_{31}$  curves in this LAOS test seems to be larger than the distinction of the five elastic moduli in the SAOS test (figure 3.9). All the curves in figure 3.13 present a similar non-monotonic trend. The upper curve (*empty rhomb symbols*) is related to the smallest average drop radius,  $R_v = 5.6 \mu\text{m}$ . By moving progressively downwards, blends A ( $6.5 \mu\text{m}$ ), E ( $6.7 \mu\text{m}$ ), D ( $8 \mu\text{m}$ ), B ( $15 \mu\text{m}$ ) are met. Hence, the nonlinear response exhibited by a polymer blend increases by decreasing the mean size of the inclusions. A reasonable explanation of this behavior can be ascribed to the specific interfacial area of the system. At fixed volume fraction, it is greater for the blend with smaller droplets.

### 3.5 Model/Experiments comparison

#### 3.5.1 The model

To model the stress response of a dilute immiscible polymer blend under LAOS two groups of equations are adopted. The first one describes the shape evolution of the drop during the imposed oscillatory shear; the second one calculates the interfacial contribution to the stress tensor coming from the deformed interface of the inclusion. The diluteness of the blend allows considering the total stress of the system as a linear superposition of the matrix contribution plus the contributions pertaining to each drop.

In principle, any modeling approach to predict inclusion dynamics can be implemented. The direct solution of the motion equations for the single drop problem under periodic shear flow would certainly give a very accurate prediction. For the sake of simplicity, however, the drop dynamic is here described with an ellipsoidal model. Indeed, several ellipsoidal models have been proposed in the recent literature (Maffettone and Minale, 1998, Almusallam et al. 2000, Yu et al. 2002, Jackson and Tucker 2003, Yu and Bousmina 2003). The Jackson and Tucker's model is by far the most complete among them. It adequately describes drop dynamics at large deformation in a very broad parameter range. Nonetheless, in this work, the Maffettone and Minale model is adopted for its simplicity. The model is formulated in terms of at most six first-order, ordinary, differential equations, and is capable of describing drop deformation up to the nonlinear range. This model is known to be accurate for small-to-medium droplet deformation, but loses some quantitative accuracy as droplet deformation becomes large. However, it provides a useful basis for analyzing and interpreting the experimental results also when significant strain deformations occur (Guido et al. 2004).

The drop is described as an ellipsoid by a second rank symmetric, positive definite, and time dependent tensor,  $\mathbf{S}$ . The shape dynamics is described by the evolution of tensor  $\mathbf{S}$  which follows the equation:

$$\frac{\partial \mathbf{S}}{\partial t} = -\frac{f_1}{\tau_D} \left( \mathbf{S} - \frac{3}{I_2} \mathbf{I} \right) + (\boldsymbol{\Omega} \cdot \mathbf{S} - \mathbf{S} \cdot \boldsymbol{\Omega}) + f_2 (\mathbf{S} \cdot \mathbf{D} - \mathbf{D} \cdot \mathbf{S}) \quad (3.12)$$

Equation 3.12 is dimensionless, the time being made nondimensional through the

emulsion time  $\tau_D = R\eta_m/\Gamma$ . In Equation 3.12,  $\mathbf{I}$  is the second rank unit tensor,  $\mathbf{D}$  and  $\mathbf{\Omega}$  are the deformation rate and the vorticity tensors respectively, and  $I_2$  is the second scalar invariant of tensor  $\mathbf{S}$ . The members of the right-hand side of the equation 3.12 represent: the first, the drop relaxation phenomena; the second, the drop vorticity-induced rotation; the third, the drop deformation-induced stretching.

The shear flows here considered give the following forms for the deformation and vorticity tensors:

$$\mathbf{D} = \frac{1}{2}\text{Ca} \begin{pmatrix} 0 & 1 & 0 \\ 1 & 0 & 0 \\ 0 & 0 & 0 \end{pmatrix}, \quad \mathbf{\Omega} = \frac{1}{2}\text{Ca} \begin{pmatrix} 0 & 1 & 0 \\ -1 & 0 & 0 \\ 0 & 0 & 0 \end{pmatrix} \quad (3.13)$$

The functions  $f_1$  and  $f_2$  appearing in equation 3.12 is:

$$f_1(\lambda) = \frac{40(\lambda+1)}{(2\lambda+3)(19\lambda+16)} \quad (3.14.a)$$

$$f_2(\lambda, \text{Ca}) = \frac{5}{2\lambda+3} + \frac{30\text{Ca}^2}{2+6\text{Ca}^2} \quad (3.14.b)$$

At rest the drop is spherical ( $\mathbf{S}=\mathbf{I}$ ).

Notice that within this description break-up is absent under shear flow for  $\lambda \geq 3$ . The model properly reduces to the theory of Taylor (1932) in the small deformation limit.

The total stress  $\boldsymbol{\sigma}$  of a dilute polymer blend constituted by Newtonian components can be predicted from Batchelor (1970):

$$\boldsymbol{\sigma} = \underbrace{-p\mathbf{I}}_{\text{isotropic term}} + \underbrace{\frac{\eta}{m}(\nabla\mathbf{v} + \nabla\mathbf{v}^T)}_{\text{external contribution}} - \underbrace{\frac{\eta_m}{V} \int_A (\mathbf{n}\mathbf{u} + \mathbf{u}\mathbf{n}) dA}_{\text{viscous term}} - \underbrace{\frac{\Gamma}{V} \int_A \left( \mathbf{n}\mathbf{n} - \frac{1}{3}\mathbf{I} \right) dA}_{\text{elastic term}} \quad (3.15)$$

*interfacial contribution*

where  $p$  is pressure,  $\nabla\mathbf{v}$  is the undisturbed velocity gradient tensor and  $\nabla\mathbf{v}^T$  its transpose,  $V$  is the total volume of the system,  $\mathbf{n}$  is the unit vector normal to the

interface between the two phases,  $\mathbf{u}$  is the velocity at the interface,  $dA$  is the area of an interfacial element, and the integrals are calculated over the whole interface of the system,  $A$ . Equation 3.15 can be used to predict the stresses if  $\mathbf{n}$  and  $\mathbf{u}$  are known. For a given imposed flow field those two vectors depend only on the drop radius  $R$ , and may vary in time as the drop shape may vary. Since drop interactions can be neglected in view of diluteness, each drop of the population can be treated as an isolated drop, here described by the MM-model.

The right-hand side of equation 3.15 contains an external and an interfacial contribution, only the latter of these two terms is useful to estimate drop size distribution of the blend. As already observed in the paragraph 3.1.2, the principal experimental problem arises from the difficulty to isolate the interfacial stress,  $\sigma_{\text{int}}$ , from the total measured stress,  $\sigma$ . LAOS tests meet right this requirement. Indeed, as showed in the previous experimental section (paragraph 3.4.2), the odd harmonics present in the blend power spectrum are just due to the interface stress contribution,  $\sigma_{\text{int}}$ . For Newtonian blend components, the external phase contribution is linear and cannot contribute to nonlinearities, thus its effects are only present in the fundamental harmonic. It is now apparent that the filtering of the matrix contribution is easily achieved by excluding the first peak of the emulsion power spectrum.

### 3.5.2 The method

The total measured interfacial stress,  $\sigma_{\text{int},m}$  (it is here considered tangential stress only, i.e. the 12 component of the stress tensor), of a dilute blend depends on an integral involving the drop population. The distribution function  $\psi(R)$ , which is the quantity to be estimated, can be discretized with a coarse-grained description with a finite number of elements  $f(R_i)$ . This approximation holds if the function  $\psi(R)$  is smooth enough compared to the sampling length. If this assumption is satisfied, the total measured interfacial stress results equal to:

$$\sigma_{\text{int},m} = \sum_i \sigma_{\text{int},t}(R_i) \cdot f(R_i) \cdot \Delta R_i \quad (3.16)$$

where  $\sigma_{\text{int},t}(R_i)$  is the theoretical interfacial stress contribution for a given drop size  $R_i$

and  $f(R_i)$  the unknown fraction of the drops with radius  $R_i$ . The equation 3.16 can be rewritten in the Fourier domain:

$$I_{k\omega,m} = \sum_i I_{k\omega,t}(R_i) \cdot f(R_i) \cdot \Delta R_i \quad (3.17)$$

where  $I_{k\omega,m}$  is the measured amplitude of the harmonic at a frequency  $k\omega$  of the acquired stress signal,  $I_{k\omega,t}(R_i)$  is the theoretical value of the harmonic at a frequency  $k\omega$  provided by the model for a drop radius of  $R_i$ . The equation 3.17 can be seen as a sum of linear terms, whose coefficients  $f(R_i)$  can be calculated straightforwardly with a simple linear regression. It must be noted that equation 3.17 can be written for different experimentally accessible values of  $k$ , except for the  $k = 1$ . Indeed, as already observed in the paragraph 3.5.1, the first peak of the power spectrum contains not only the stress interfacial contribution, but also the matrix stress contribution. In this work a value of  $k = 3$  is used. In some spot calculations also the fifth harmonic is considered, hence  $k = 5$ .

### 3.5.3 Blend morphology estimation

The model/experiment comparison will be explicitly showed for the blend E, similar results have been obtained for the other systems. The study is performed into three subsequent steps, aiming at a progressive more detailed description of the emulsion microstructure.

1) The first model/experiment comparison has been performed by assuming a monodisperse drop population. This choice makes easier and faster the simulation and also allows obtaining a preliminary check of the adopted methodology. The drop radius used in the numerical simulation is furnished by the linear measurement and it is equal to 6.7  $\mu\text{m}$  for the blend E. The results are reported in figure 3.14, where the absolute value of the third harmonic normalized with the strain amplitude,  $I_3/\gamma_0$ , as a function of the strain amplitude,  $\gamma_0$ , is plotted for the experimental (*filled squares*) and simulated (*solid line*) data. A good agreement is apparent: the theory captures qualitatively the occurrence of a maximum for the same deformation value observed in the experiment. It is remarkable that no adjustable parameters are introduced in the model. There is, however, a quantitative discrepancy between theory and experimental points. This can

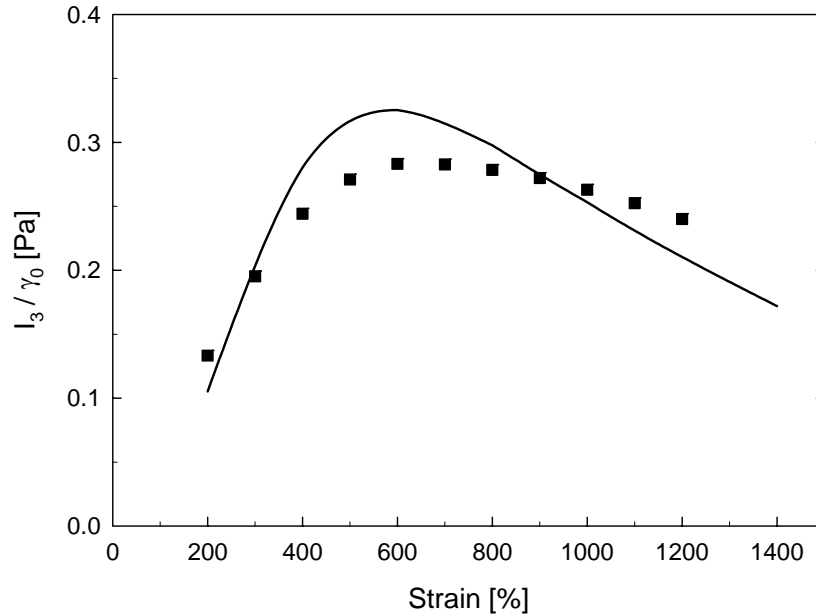


Figure 3.14. Absolute value of the third harmonic normalized with the strain amplitude as a function of the strain amplitude. The filled squares are the experimental points, the solid line represents the simulated data for a monodisperse polymer blend with a characteristic size of 6.7  $\mu\text{m}$ .

be due to a limited efficiency of the actual model, especially at high strain amplitudes (Guido et al. 2004), or to some errors in the estimation of physical parameters. It is demonstrated that the simulation is strongly influenced by the value of the viscosity ratio. However, a perfect overlapping between simulated and measured points was not expected because of the restricting hypothesis of monodispersity.

It must be noted that the third harmonic is normalized with the strain amplitude and not, as usual in the Fourier Transform Rheology, with the first harmonic. This has been done to facilitate the simulation procedure.  $I_3/\gamma_0$  has the dimension of a stress, so it is expressed in Pascal. To convert stress electric signal from Volt to Pascal the coefficients  $k_\sigma^L$  and  $k_\sigma^H$  introduced in the paragraph 3.3.3 are adopted.

2) The second model/experiment comparison removes the assumption of a monodisperse sample and assumes a log-normal distribution of droplet sizes:

$$\psi(R) = \frac{1}{\sqrt{2\pi} R \sigma} \exp\left(-\frac{1}{2} \frac{(\log R - \mu)^2}{\sigma^2}\right) \quad R \geq 0 \quad (3.18)$$

In the equation 3.18,  $\mu$  and  $\sigma$  represent two adjustable parameters.

It must be remarked that a log-normal distribution is reasonable according with some optical analysis on dilute polymer blends present in the literature (Caserta et al. 2005).

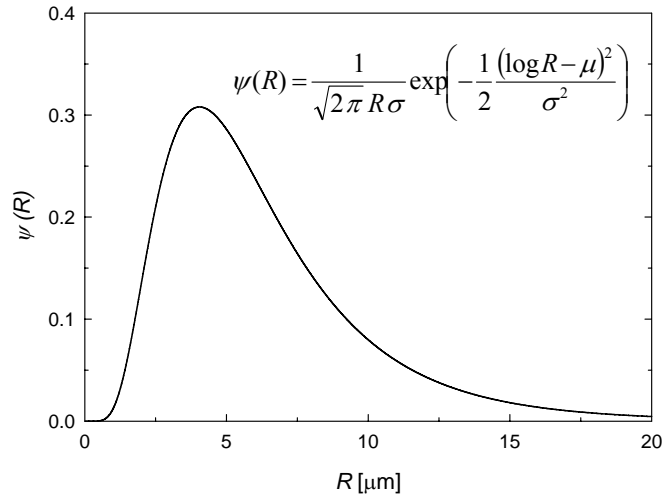


Figure 3.15. Log-normal distribution of droplet sizes ( $\mu = 1.70$  and  $\sigma = 0.55$ ). The average drop radius  $R_v$  is 7.

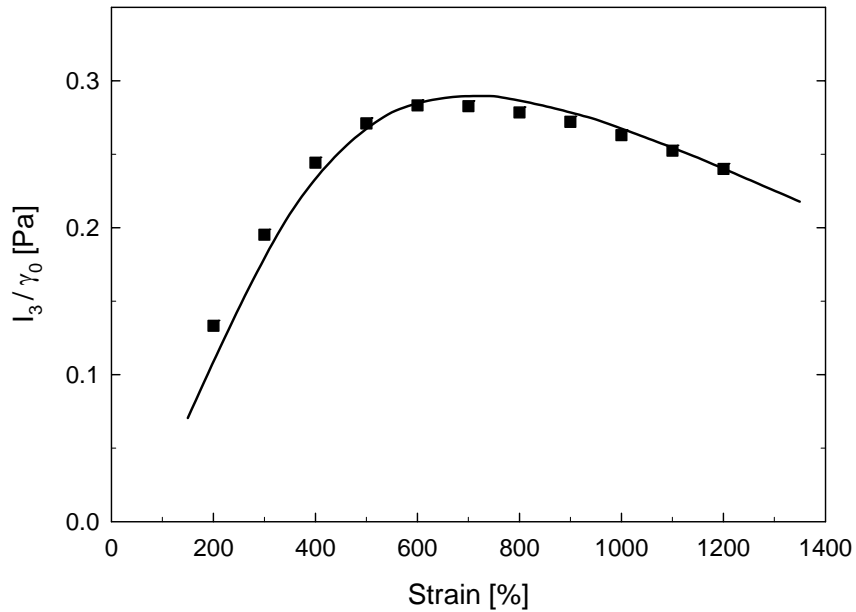


Figure 3.16. Absolute value of the third harmonic normalized with the strain amplitude as a function of the strain amplitude. The filled squares are the experimental points, the solid line represents the simulated data for the log-normal distribution of drop sizes reported in figure 3.15.

The values of  $\mu$  and  $\sigma$  are adjusted in order to minimize the distance between measured and theoretical points. The better results are obtained for  $\mu = 1.70$  and  $\sigma = 0.55$ . The corresponding log-normal distribution is reported in figure 3.15. In this case, the model/experimental agreement is quantitative, as observable in figure 3.16. The log-normal distribution with the estimated values of the adjustable parameters give a reasonable average volumetric drop radius  $R_v = 7$ , that is very close to the one predicted with Palierne model.

3) The third model/experiment comparison tries to estimate the drop size distribution, without any assumption on its form. Of course, this requires cumbersome experimental and simulating efforts.

Regarding the experimental side, more data have to be collected. For this reason, it is measured not only the third harmonic, but also the fifth one. In this way, the number of the experimental points is doubled, passing from eleven to twenty-two.

Regarding the simulation side, some fundamental choices have to be done. First of all, the number of discrete elements  $f(R_i)$  must be fixed. This number is conditioned by the number of experimental points. In the present work, a value of eight has been adopted. The width  $\Delta R_i$  of each block  $f(R_i)$  represents another variable. Here two different choices have been done:  $\Delta R_I = 2.5 \mu\text{m}$  and  $\Delta R_{II} = 1.5 \mu\text{m}$ . From now on the indexes “I” and “II” will be used to distinguish the two cases. The explored radius range  $\in [0 \div 8 \cdot \Delta R] \mu\text{m}$ ; so, in the case I, it is equal to  $[0 \div 20] \mu\text{m}$ , in the case II, it is equal to  $[0 \div 12] \mu\text{m}$ .

The distributions obtained with the discretization I is reported in the figure 3.17. It is formed by two blocks, which leads to an average drop radius of  $\sim 6 \mu\text{m}$ . It must be noted that the obtained distribution, although coarse-grained, is in good agreement with the previous log-normal distribution (figure 3.15). The model/experiment comparison is showed in figure 3.18, where the  $I_3/\gamma_0$  and  $I_5/\gamma_0$  are plotted versus  $\gamma_0$ . The accord between measured and simulated points is good for the third harmonic, while is quite bad for fifth one. This can be related to two main reasons: the limited efficiency of the actual model at high strain amplitudes and the experimental error in the measure of fifth

peak, which is smaller than the third one and consequently more affected by the background noise.

The distributions obtained with the discretization II is reported in the figure 3.19, it is quite different from the one represented in figure 3.17. It is bimodal with dominant

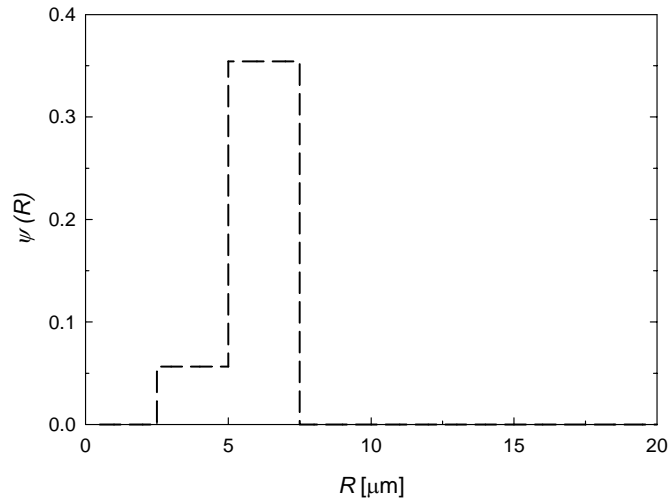


Figure 3.17. Discrete drop size distribution (case I)  
 $R \in [0 \div 20], \Delta R_I = 2.5 \mu m$

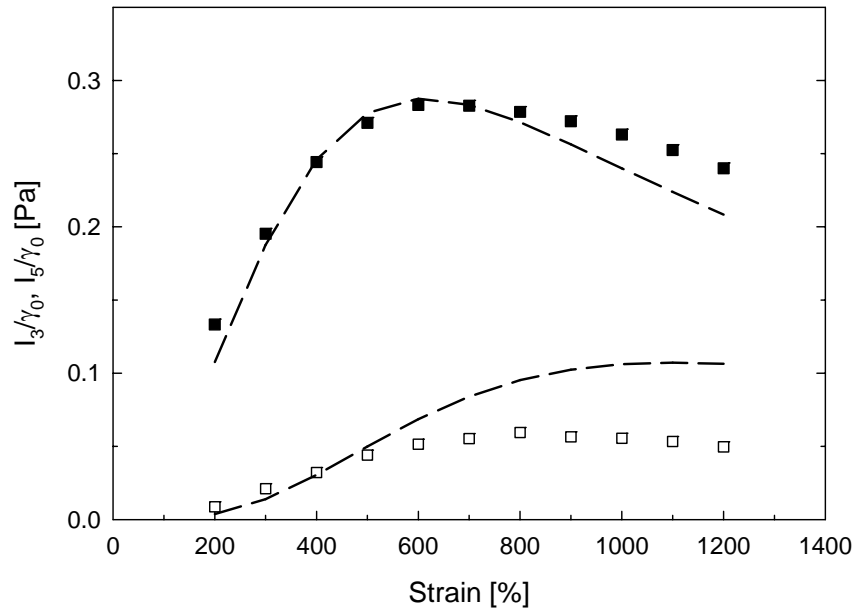


Figure 3.18. Absolute value of the third (■) and the fifth (□) harmonic normalized with the strain amplitude as a function of the strain amplitude. The long-dash lines represent the simulated data for the discrete distribution reported in figure 3.17

drop sizes equal to  $\sim 3.7 \mu\text{m}$  and  $\sim 6.7 \mu\text{m}$ . The average volumetric drop radius is around  $6 \mu\text{m}$ . The model/experiment comparison is showed in figure 3.20, the results are similar to the ones reported in figure 3.18. It must be noted that the occurrence of a bimodal distribution is not a new; for example, it is already observed by Grizzuti e

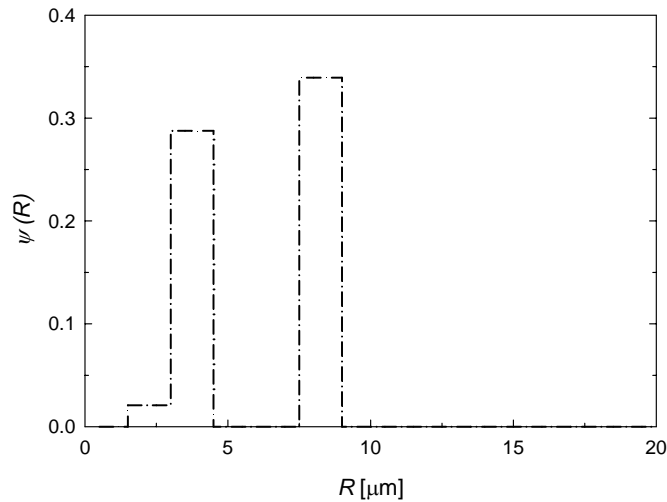


Figure 3.19 Discrete drop size distribution (case II)  
 $R \in [0 \div 12], \Delta R_{II} = 2.5 \mu\text{m}$

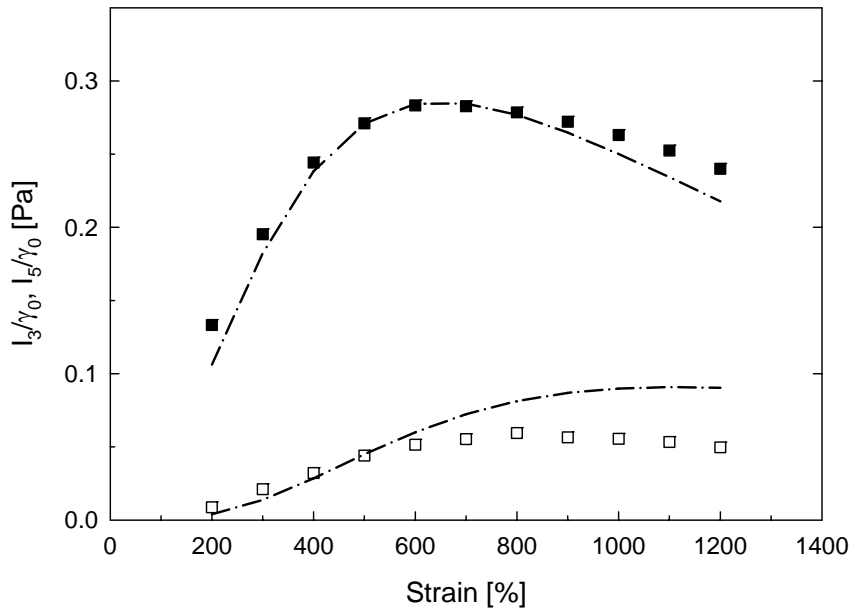


Figure 3.20. Absolute value of the third (■) and the fifth (□) harmonic normalized with the strain amplitude as a function of the strain amplitude. The dash-dot lines represent the simulated data for the discrete distribution reported in figure 3.19

Bifulco (1997) by means of optical techniques. Furthermore, during LAOS tests, breakup phenomena by “end pinching” may occur, as experimentally demonstrated by Wannaborworn et al. (2002). At large strain deformation, a drop is stretched in the flow direction; it can release from its ends a smaller droplet when the flow direction is reversed. This phenomenon supports the occurrence of two characteristic drop sizes. It is remarkable that bimodality cannot be individuated by means of linear measurements.

The simulation I and II lead to two different distributions, even if the average volumetric drop radius is almost the same. It is possible that the simulation I does not capture the bimodality because of the greater value of  $\Delta R_I$ . At the same time, the condition number of the case II is one order of magnitude larger than the case I. So, it is not possible to state which distribution is more correct, even if the distribution II seems more reasonable than distribution I. To achieve a definitive response, further improvements in measure and simulation procedure must be done. A fundamental step will require the acquisition of even more experimental points and also the separation of the real and the imaginary part of the stress Fourier spectrum.

However, the obtained results are encouraging. They indicate that the proposed experimental procedure works and, once appropriately refined, it can give the real drop size distribution of a dilute polymer blend.

### **3.6 On the occurrence of even harmonics**

As already observed, the tangential stress response of a non-Newtonian material subjected to a large amplitude oscillatory shear should contain only the odd harmonics of the excitation frequency,  $\omega$ . But, in the power spectrum of the investigated blend (figure 3.10.d) appears also a peak at  $2\omega$ .

Even overtones have been already observed in the literature; their occurrence is often ascribed to experimental insufficiencies (Onogi et al. 1970) and, in particular, to a wall slip phenomena (Reimers and Dealy 1996). Alternative explanations also exist, for example, Wilhelm et al. (1998) impute the occurrence of even peaks to “a time-dependent memory effect or non-linear elastic contribution in the system”. Sagis et al. (2001) have justified the appearance of even harmonics by incorporating an orientation

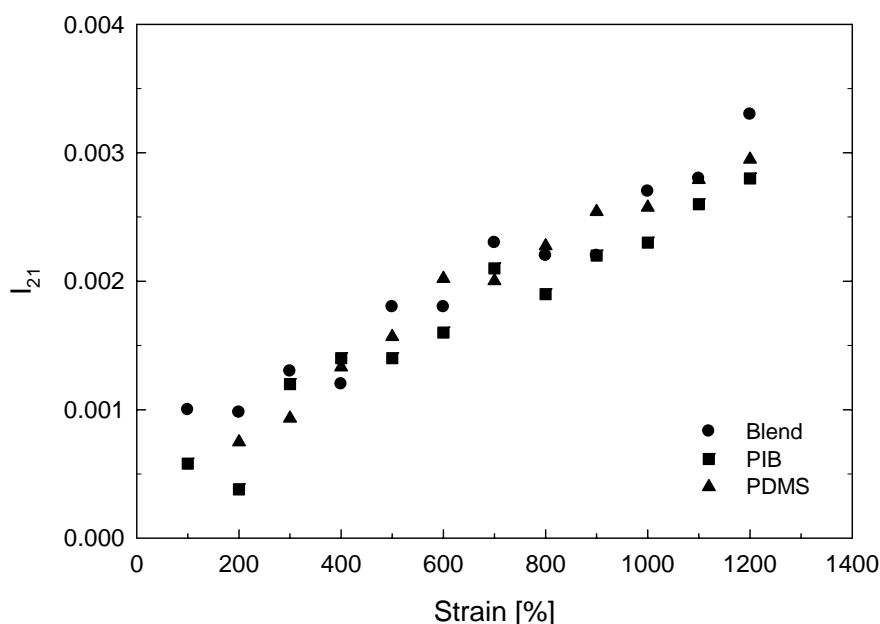


Figure 3.21. Absolute value of the second harmonic normalized with the first one as a function of the applied strain for the blend and for the pure polymers, at 30°C. The oscillation frequency is 0.1 Hz.

tensor that represents an anisotropic internal microstructure. Of course, the origin of even peaks depends on the investigated system and on the adopted experimental apparatus, so, it could not be unambiguously determined.

As regard the present study, the measured second peak seems to be totally unrelated to the tested material, but it comes from the instrument and, in particular, it is linked to the angular displacement of the oscillating plate of the rheometer. The proposed picture can be justified in view of the following experimental evidence.

Figure 3.10.d, 3.11.a and 3.11.b, reported in paragraph 3.4.2, represent, respectively, the stress response in the Fourier domain of the blend, the pure PIB and the pure PDMS. The imposed oscillatory deformation has amplitude of 800% and frequency of 0.1 Hz. A second harmonic,  $I_{21}$ , is clearly present in all three spectra and, in particular, its height is almost identical, thus immediately suggesting that the even peak is independent by the tested material.

The three previous graphs are referred to one strain amplitude, while, in the figure 3.21,  $I_{21}$  is plotted for different deformations ranging from 100 to 1200%. The second overtones are practically the same for the blend, the PIB and the PDMS at all the

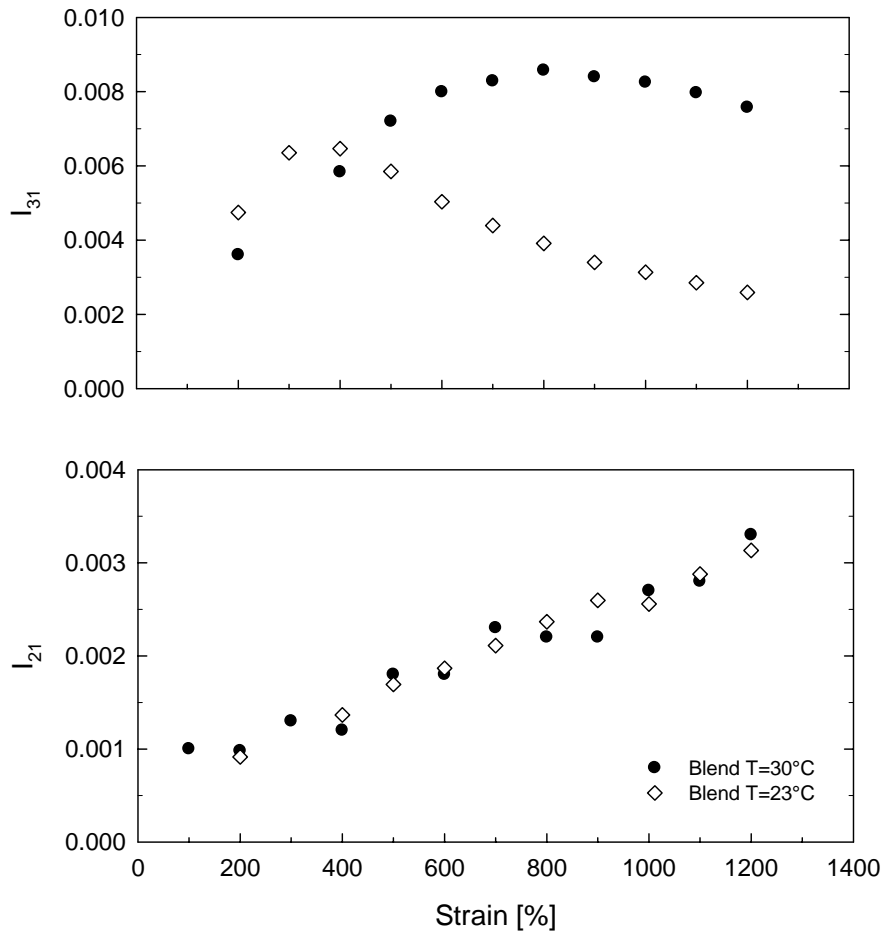


Figure 3.22 Absolute value of the second (lower graph) and the third (upper graph) harmonic normalized with the first one as a function of the applied strain for the same blend at two different temperatures. The oscillation frequency is 0.1 Hz.

explored deformations.

LAOS experiences have been carried out on the same blend at 23 and 30°C. Temperature greatly influences the value of the viscosity ratio,  $\lambda$ , which passes from 3.2 at 30°C to 1.5 at 23°C. A change of  $\lambda$  leads to a completely different dynamics of drop deformation under LAOS. In figure 3.22 the trend of the normalized second,  $I_{21}$ , and third,  $I_{31}$ , harmonic versus strain for both the systems is reported. The  $I_{31}$  is completely dissimilar thus confirming the different behavior of the blend at 23 and 30°C. The  $I_{21}$ , on the contrary, is substantially overlapped thus demonstrating again the absence of connection between the occurrence of the second harmonic in the Fourier spectra and the tested material.

What affect the amplitude of the second peak? Figure 3.21 and 3.22 seem to suggest that  $I_{21}$  is proportional to the applied strain. This is not completely correct, as testified by figure 3.23 that shows the behavior of the second harmonic versus strain. The experimental points are referred to the same blend, but they are obtained with three different geometries:

- 1) *cone-plate* with a diameter  $D = 50$  mm and an angle  $\alpha = 0.02$  rad (●)
- 2) *cone-plate* with a diameter  $D = 50$  mm and an angle  $\alpha = 0.04$  rad (○)
- 3) *plate-plate* with a diameter  $D = 50$  mm and a gap  $\delta = 0.75$  mm (●)

Experimental points reported in figure 3.23 present a different behavior; in particular, at a fixed deformation, the value of  $I_{21}$  is larger for the *cone-plate* 2), followed by *cone-plate* 1) and then by the *plate-plate* 3). At this point, it must be noted that these three tools realize a fixed strain by means of three different angular displacements,  $\Omega$ . Indeed, for a *cone-plate* geometry  $\Omega = \gamma \cdot \alpha$ , while for a *plate-plate* geometry  $\Omega = 2 \cdot \gamma \cdot \delta / D$ . This observation suggests to plot the data, already showed in figure 3.23, as a function of the

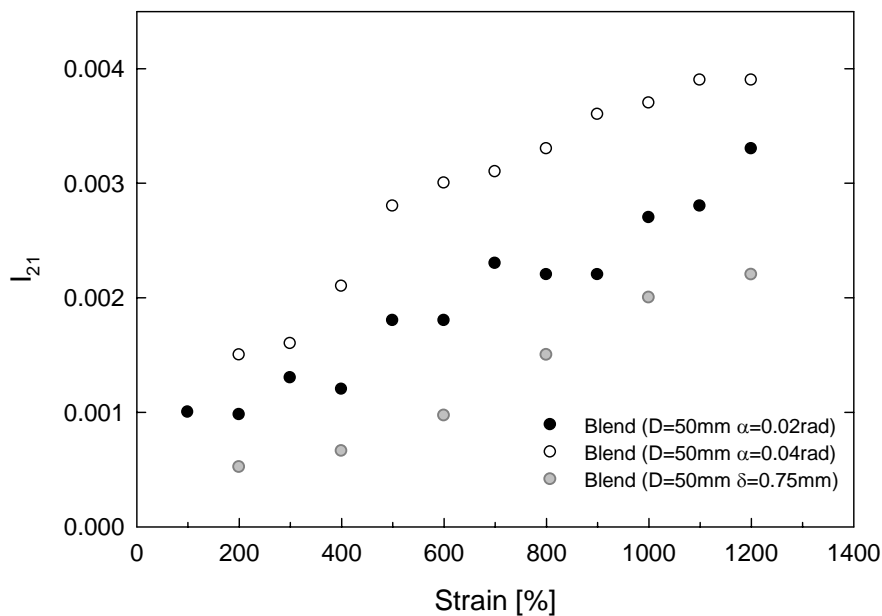


Figure 3.23 Absolute value of the normalized second harmonic as a function of the applied strain for the same polymer blend, at 30°C. The oscillation frequency is 0.1 Hz. The data are obtained by means of three different geometries.

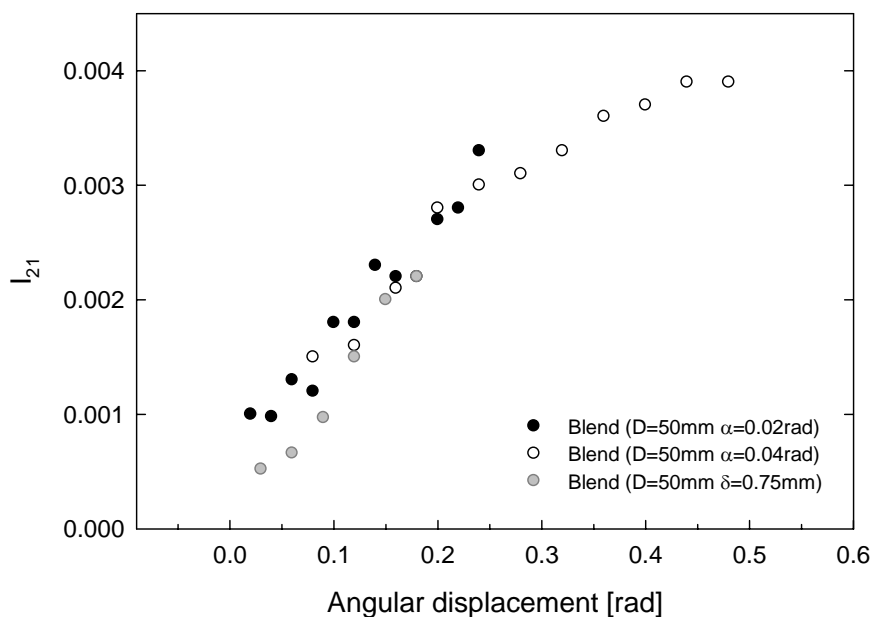


Figure 3.24 Absolute value of the normalized second harmonic as a function of the angular displacement of the oscillating plate of the rheometer for the same polymer blend.  $T = 30^{\circ}\text{C}$ . The oscillation frequency is 0.1 Hz. The data are obtained by means of three different geometries

angular displacement. The result is reported in figure 3.24. In such a plot, the experimental points present the same trend, thus demonstrating that the amplitude of the second harmonic is exclusively influenced by the angular position of the oscillating plate. In conclusion, the occurrence of  $I_{21}$  is probably due to a not perfect alignment of the upper and lower plate.

## REFERENCES

- Almusallam AS, Larson RG, Solomon MJ (2000) "A constitutive model for the prediction of ellipsoidal droplet shapes and stresses in immiscible blends." *J Rheol* **44**(5):1055-1083
- Batchelor GK (1970) "The stress system in a suspension of force-free particles." *J Fluid Mech* **41**:545-570
- Bentley BJ, Leal LG (1986) "An experimental investigation of drop deformation and breakup in steady, two-dimensional linear flows." *J Fluid Mech* **167**:241-283
- Bousmina M (1999) "Rheology of polymer blends: linear model for viscoelastic emulsions." *Rheol Acta* **38**:73-83
- Bousmina M, Bataille P, Sapiéha S, Schreiber HP (1995) "Comparing the effect of corona treatment and block copolymer addition on rheological properties of polystyrene/poly-ethylene blends." *J Rheol* **39**:499-517

- Bousmina M, Muller R (1993) "Linear viscoelasticity in the melt of impact PMMA. Influence of concentration and aggregation of dispersed rubber particles." *J Rheol* **37**:663-679
- Bracewell RN (1986) "The Fourier Transform and Its Applications." New York, McGraw-Hill
- Calvão PS, Yee M, Demarquette NR (2005) "Effect of composition on the linear viscoelastic behavior and morphology of PMMA/PS and PMMA/PP blends." *Polymer* **46**:2610-2620
- Caserta S, Sabetta L, Simeone M, Guido S (2005) "Shear-induced coalescence in aqueous biopolymer mixtures." *Chem Eng Sci* **60**:1019-1027
- Caserta S, Simeone M, Guido S (2004) "Evolution of drop size distribution of polymer blends under shear flow by optical sectioning." *Rheol Acta* **43**(5):491-501
- Choi S, Schowalter W (1975) "Rheological properties of non-dilute suspensions of deformable particles." *Phys Fluid* **18**:420-427
- Cristini V, Blawdziewicz J, Loewenberg M (1998) "Drop breakup in three-dimensional viscous flow." *Phys Fluids* **10**:1781-1783
- Doi M, Ohta T (1991) "Dynamics and rheology of complex interfaces. I." *J Chem Phys* **95**:1242-1248
- Friedrich C, Gleinser W, Korat E, Maier D, Weese J (1995) "Comparison of shere-size distributions obtained from rheology and transmission electron microscopy in PMMA/PS blends." *J Rheol* **39**(6):1411-1425
- Grace HP (1982) "Dispersion phenomena in high viscosity immiscible fluid systems and application of static mixers as dispersion devices in such systems." *Chem Eng Commun* **14**:225-277
- Graebling D, Benkira A, Gallot Y, Muller R (1994) "Dynamic viscoelastic behavior of polymer blends in the melt-experimental results for PDMS/POE-DO, PS/PMMA and PS/PEMA blends." *Eur Polym J* **30**:301-308
- Graebling D, Muller R (1990) "Rheological behavior of polydimethylsiloxane/poly-oxyethylene blends in the melt. Emulsion model of two viscoelastic liquids." *J Rheol* **34**:193-205
- Graebling D, Muller R, Paliarne JF (1993a) "Linear viscoelastic behavior of some incompatible blends in the melt. Interpretation of data with a model of emulsion of viscoelastic liquids." *Macromolecules* **26**:320-329
- Graebling D, Muller R, Paliarne JF (1993b) "Linear viscoelasticity of incompatible polymer blends in the melt in relation with interfacial properties." *J Phys IV* **3**:1525-1534
- Grizzuti N, Bifulco O (1997) "Effect of coalescence and break up on the steady-state morphology of an immiscible polymer blend in shear flow." *Rheol Acta* **36**:406-415
- Grosso M, Maffettone PL (2004) "Caratterizzazione di blend polimerici diluiti tramite Fourier Transform Rheology." *Atti VIII Convegno della SIR*:235-239
- Guido S, Grosso M, Maffettone PL (2004) "Newtonian drop in a newtonian matrix subjected to large amplitude oscillatory shear flows." *Rheol Acta* **43**:575-583
- Guido S, Minale M, Maffettone PL (2000) "Drop shape dynamics under shear-flow reversal." *J Rheol* **44**(6):1385-1399
- Jackson NE, Tucker CL (2003) "A model for large deformation of an ellipsoidal droplet with interfacial tension." *J Rheol* **47**:659-682
- Jansseune T, Mewis J, Moldenaers P, Minale M, Maffettone PL (2000) "Rheology and rheological morphology determination in immiscible two-phase polymer model blends." *J Non-Newtonian Fluid Mech* **93**:153-165
- Jansseune T, Vinckier I, Moldenaers P, Mewis J (2001) "Transient stresses in immiscible model polymer blends during start-up flows." *J Non-Newtonian Fluid Mech* **99**:167-181
- Kennedy MR, Pozrikidis C, Skalak R (1994) "Motion and deformation of liquid drops, and the rheology of dilute emulsions in simple shear flow." *Comput Fluids* **23**:251-278
- Kerner EH (1956) "The elastic and thermoelastic properties of composite media." *Proc Phys Soc A* **69**:808-813
- Krause S (1978) "Polymer-polymer compatibilty." In: Paul DR, Newman S (eds) "Polymer blends." New York, Academic Press
- Lacroix C, Aressy M, Carreau PJ (1997) "Linear viscoelastic behavior of molten polymer blends: a comparative study of the Paliarne and Lee and Park models." *Rheol Acta* **36**:416-428
- Lee HM, Park OO (1994) "Rheology and dynamics of immiscible polymer blends." *J Rheol* **38**:1405-1425

- Maffettone PL, Minale M (1998) "Equation of change for ellipsoidal drops in viscous flow." *J Non-Newtonian Fluid Mech* **78**:227-241
- Minale M, Moldenaers P, Mewis J (1999) "Transient flow experiments in a model immiscible polymer blend." *J Rheol* **43**(3):815-827
- Oldroyd JG (1953) "The elastic and viscous properties of emulsions and suspensions." *Proc Roy Soc Lond Ser A* **218**:122-132
- Onogi S, Masuda T, Matsumoto T (1970) "Nonlinear behavior of viscoelastic materials. I: Disperse systems of polystyrene solution and carbon black." *Trans Soc Rheol* **14**:275-294
- Palierne JF (1990) "Linear rheology of viscoelastic emulsions with interfacial tension." *Rheol Acta* **29**:204-214
- Rallison JM (1984) "The deformation of small viscous drops and bubbles in shear flows." *Annu Rev Fluid Mech* **16**:45-66
- Ramic AJ, Hudson SD, Jamieson AM, Manas-Zloczower I (2000) "Temporary droplet-size hysteresis in immiscible polymer blends." *Polymer* **41**:6263-6270
- Ramirez RW (1995) "The FFT Fundamentals and Concepts." Englewood Cliffs, Prentice-Hall
- Reimers MJ, Dealy JM (1996) "Sliding plate rheometer studies of concentrated polystyrene solutions: Large amplitude oscillatory shear of a very high molecular weight polymer in diethyl-phthalate." *J Rheol* **40**(1):167-186
- Sagis LM, Ramaekers M, van der Linden E (2001) "Constitutive equations for an elastic material with anisotropic rigid particles." *Phys Rev E* **63**
- Sigillo I, di Santo L, Guido S, Grizzuti N (1997) "Comparative measurements of interfacial tension in a model polymer blend." *Polym Eng Sci* **37**(9):1540-1549
- Skoog DA (1992) "Principles of instrumental analysis." Fort Worth, Saunders College Publishing
- Stone HW (1994) "Dynamics of drop deformation and breakup in viscous fluids. The viscosity of a fluid containing small drops of another fluid." *Annu Rev Fluid Mech* **26**(65-102)
- Taylor GI (1932) "The viscosity of a fluid containing small drops of another fluid." *Proc R Soc A* **138**:41-48
- Tucker CL, Moldenaers P (2002) "Microstructural evolution in polymer blends." *Annu Rev Fluid Mech* **34**:177-210
- Vinckier I, Moldenaers P, Mewis J (1996) "Relationship between rheology and morphology of model blends in steady shear flow." *J Rheol* **40**(4):613-631
- Vinckier I, Moldenaers P, Terracciano AM, Grizzuti N (1998) "Droplet size evolution during coalescence in semiconcentrated model blends." *AIChE J* **44**(4):951-958
- Wannaborworn S, Mackley MR, Renardy Y (2002) "Experimental observation and matching numerical simulation for the deformation and breakup of immiscible drops in oscillatory shear." *J Rheol* **46**(5):1279-1293
- Wilhelm M (2002) "Fourier-Transform Rheology." *Macromol Mater Eng* **287**(2):83-105
- Wilhelm M, Maring D, Spiess HW (1998) "Fourier-transform rheology." *Rheol Acta* **37**:399-405
- Wilhelm M, Reinheimer P, Ortseifer M (1999) "High sensitivity Fourier-transform rheology." *Rheol Acta* **38**:349-35
- Yu W, Bousmina M (2003) "Ellipsoidal model for droplet deformation in emulsions." *J Rheol* **47**:1011-1039
- Yu W, Bousmina M, Grmela M, Zhou CX (2002) "Modeling of oscillatory shear flow of emulsions under small and large deformation fields." *J Rheol* **46**:1401-1418
- Yu W, Bousmina M, Zhou C (2006) "Note on the morphology determination in emulsions via rheology." *J Non-Newtonian Fluid Mech* **133**:57-62

## CONCLUDING REMARKS

In this work dynamic mechanical spectroscopy (DMS) is used to characterize two different complex fluids. In particular, linear DMS is adopted to study the thermo-reversible gelation of aqueous solutions of hydroxypropylcellulose (HPC). Nonlinear DMS is utilized to probe the microstructure of dilute immiscible polymer blends. The aim of the present study has been not only to obtain a good characterization of the two complex fluids considered, but also to explore the potentiality of both linear and nonlinear dynamic mechanical spectroscopy.

The choice of two different complex fluids can be understood in view of the following considerations. During a typical DMS experiment, the material is subjected to a sinusoidal deformation and the corresponding stress is measured. By using some adequate theoretical models, the system response may be correlated to material microstructure. There are two principal families of DMS tests, depending on the amplitude  $\gamma_0$  of the imposed deformation: SAOS (Small Amplitude Oscillatory Shear) and LAOS (Large Amplitude Oscillatory Shear). In the former case,  $\gamma_0$  is small enough to produce a linear response of the system; in the latter case,  $\gamma_0$  is large and a nonlinear response occurs. SAOS tests represent a robust, largely adopted rheological procedure. The mechanical behavior of materials in this regime is well investigated and documented. On the contrary, LAOS tests are a much younger experimental technique. Nonlinear measurements are intrinsically more complex than linear ones, from both the experimental and the theoretical point of view. The recent growth of this technique is mainly due to the significant improvements of instrumental and software devices. At this point, it is apparent that SAOS and LAOS experimental procedures possess a different “maturity”. For this reason, in this work, the mature SAOS tests have been adopted to characterize a system showing a complex morphology evolution: aqueous solutions of HPC. On the contrary, the still young LAOS techniques have been applied to the study of a system already well known in the linear regime: immiscible polymer blend.

Of course, the choice of the two complex fluids is not casual, but is related to their

technological importance:

- Aqueous solutions of hydroxypropylcellulose (HPC) have the peculiar characteristic to form gel upon heating at about human body temperature. This feature, along with the well-known HPC biocompatibility, makes the material attractive as an injectable drug delivery matrix. Indeed, the system, liquid at room temperature, can easily be injected into the human body; once at 37°C it gels. Through the gel, the drug can be released with controlled rate.
- Polymer blends constitute a material class of increasing importance. Indeed, blending immiscible polymers is a good alternative to synthesizing new monomers to obtain high-performance products. The typical microstructure of a dilute emulsion consists of spherical droplets immersed in a continuous matrix. The size and distribution of the globular domains strongly affect the final properties of the system.

The fundamentals of both linear and nonlinear dynamic mechanical spectroscopy have been discussed in chapter 1.

In chapter 2, SAOS tests have been adopted to study the thermoreversible gelation of aqueous solutions of hydroxypropylcellulose. The direct *sol-gel* and the reverse *gel-sol* transition have been studied by performing heating/cooling cycles with different thermal ramp rates. The effect of HPC concentration, HPC molecular weight and ionic strength of solutions on the entire process has also been analyzed. Linear dynamic mechanical spectroscopy shows as a very sensitive tool to study the complex morphological evolution of the system.

By increasing temperature of the HPC aqueous solutions, the quality of polymer/solvent interactions changes, thus leading to a couple of phenomena: precipitation and gelation. At room temperature, physical bonds among hydrophobic segments of HPC are screened by hydration water. At higher temperature, the quality of water/polymer interactions deteriorates and propyl segments remain progressively “uncovered” and free to interact with each other. At around 46°C, intra-molecular associations occur, leading to a partial precipitation of HPC. Some chains or fractions of

chain shirk from the solution, and they do not contribute to the viscoelasticity of the system anymore. Starting from  $\sim 50^{\circ}\text{C}$ , inter-molecular interactions start to happen among HPC still dissolved in water (“active” chains), thus leading to a gelation of the system ( $\sim 56^{\circ}\text{C}$ ). Precipitation and gelation, therefore, compete for the same HPC chains. The amount of precipitates and, consequently, of the active chains can be controlled by the heating rate, which represents a crucial parameter of the whole process. Indeed, when the thermal ramp is fast, a little precipitation takes place, leading to the formation of the so-called “strong” gel. Conversely, when the system is slowly heated, many chains do precipitate and a “weak” gel is obtained.

Thermogelation is totally reversible, although the dynamics of formation and destruction of the microstructure is completely different. Experimental evidence suggests that, upon cooling, gel destruction and re-dissolution of precipitates happen together. Indeed, when the temperature of the system is reduced, the viscoelastic moduli, and in particular  $G'$ , do not follow the corresponding heating paths but show higher values. While gel destruction determines a reduction of the system viscoelasticity, the simultaneous re-dissolution of precipitates favors its increment. This is the cause of the *high temperature hysteresis loop* formation. By reducing cooling rate, this high temperature hysteresis loop broadens, just because a larger re-dissolution of HPC chains takes place. A *low temperature hysteresis loop* is also observed with, most probably, a kinetic origin. The loop size decreases by reducing the cooling ramp rate.

In conclusion, we believe that precipitation is the main reason of the observed complex morphology evolution. When precipitation is absent (as for HPC concentration of 20%wt), both high and low temperature hysteresis loops disappear.

The effect of HPC molecular weight,  $M_w$ , is also considered. The above proposed morphological evolution, both for the direct *sol-gel* and for the reverse *gel-sol* transition, is referred to the lowest of the adopted HPC molecular weights. It is found that  $M_w$  has only a slight influence on the direct *sol-gel* transition. Its principal effect is an anticipation of the gelation process, which in fact occurs at progressively lower temperatures with increasing  $M_w$ . Consequently, the precipitation/gelation gap is reduced. On the contrary,  $M_w$  strongly influences the reverse *gel-sol* transition. In

particular, for the higher molecular weights, gel breakup is not counterbalanced by a re-dissolution of HPC molecules, but is coupled with precipitation of other chains.

Finally, the characteristic temperatures of the process,  $T_p$  (precipitation temperature) and  $T_{co}$  (cross-over temperature), can be modulated by changing the salinity of the aqueous solution. In particular, the addition of *KCl* determines the reduction of both temperatures. This reduction is linearly proportional to the amount of dissolved salt. By controlling the ionic strength of the solution,  $T_{co}$  can be fixed at 37°C. This is fundamental for the use of HPC aqueous solutions as injectable drug delivery systems.

In chapter 3, the application of nonlinear dynamic mechanical spectroscopy to estimate the drop size distribution of dilute immiscible polymer blends is described.

The innovative aspect of this research is as follow. Fourier Transform Rheology (FTR) is here coupled with a theoretical model to obtain a quantitative description of the microstructure of a complex fluid. In particular, the proposed methodology allows one to determine the size distribution of drops in a polymer blend, via measurements of nonlinear viscoelasticity. It must be noted that linear viscoelastic measurements are generally able only to give the average drop size of such a system.

Great efforts of this work have been focused on the experimental part. The rheometer has been properly modified to perform LAOS measurements and a data acquisition and handling system has been created and optimized.

The blend is composed by poly-dimethylsiloxane (PDMS) in poly-isobutene (PIB). The volumetric fraction of PDMS is equal to 10%. The blend is preliminarily characterized in linear regime, by means of SAOS tests, in order to calculate the average drop size of the system. When the amplitude of the oscillatory deformation becomes larger than 100% a nonlinear behaviour starts to occur. The blend stress response is best analyzed in the Fourier domain where the nonlinearity is clearly evidenced by the appearance of odd-multiples of the fundamental harmonic. In particular, the third and the fifth peaks are clearly distinct from background noise. It is remarkable that the stress response of the pure components, under the same experimental conditions, presents negligible odd harmonics, thus indicating that the blend nonlinearity does not depend on

the neat PDMS and PIB behaviour, but is due to the interfacial stress coming from the deforming interface of the drops.

The nonlinear results are compared with theoretical predictions obtained by coupling the Maffettone and Minale model (MM-model) with Batchelor theory. The MM-model describes the shape evolution of a single drop under a generic flow field (e.g. LAOS flow). Although the model loses some quantitative accuracy at very large drop deformation, it is here adopted for its simplicity. Batchelor theory calculates the interfacial stress arising from the deformed interface of a drop. The diluteness of the system allows considering the total interfacial stress of the blend as a linear superposition of the contributions pertaining to each drop.

The experimental results are successfully compared with the theoretical predictions, leading to an estimation of drop size distribution of the PDMS/PIB blend. The average drop size of the obtained distribution is in agreement with the average drop size calculated through linear viscoelasticity. It must be noted that the calculated distribution is still coarse-grained. Nevertheless, it clearly demonstrates that the proposed methodology works and gives reasonable results. Therefore, LAOS procedure deserves further investigations and extensions in order to refine the accuracy of the blend drop size distribution.

